

## ABSTRACT

ISLAM, MD DIDARUL. Template-free Scalable Fabrication of Linearly Periodic Microstructures. (Under the direction of Dr. Jong Eun Ryu).

Periodic micro/nano-scale structured surfaces from nature have inspired numerous scientific studies to adapt design and construction from such ordered surfaces for various applications, including superhydrophobic (SHPo) drag-reduction. However, one primary concern of practical applications of such periodic microstructures remains the scalability of conventional microfabrication technologies. This study demonstrated a simple template-free scalable manufacturing technique to fabricate linearly periodic microstructures by controlling the ribbing defects in the forward roll coating. Viscoelastic composite coating materials were designed using carbon nanotubes (CNTs) and polydimethylsiloxane (PDMS) to obtain the desired ribbing geometry. The ribbing behaviors during the roll coating were controlled with process parameters that resulted in variable periodicity of the microstructures with a spacing of 114 – 700  $\mu\text{m}$ . The ribbing patterns showed a transition from the linear alignment to a random structure as the instability driving force (i.e., the capillary number) increased. Those nanocomposite surfaces with the ribbing microstructures showed a high Wenzel roughness factor ( $r$ ) that ranges from 1.6 to 3.6, which resulted in water contact angles of  $128^\circ$  to  $158^\circ$ , respectively. The bottom of a 3D printed model boat was coated with the nanocomposite film featured with the linearly-aligned microstructures to demonstrate the hydrodynamic friction reduction. The 3D printed boat showed 7 – 8% faster speed than the boat with a flat PDMS film when towed in a static water pool. In addition, the boat with the microstructured coating showed an 11.9% increased loading capacity by weight. On the other hand, the CNT-PDMS composite materials showed the reinforcement in mechanical properties as the cohesive failure occurs at 7 N force, whereas the bare-PDMS fails at

3.6 N. In addition, CNT-PDMS films showed electric conductivity, where the sheet resistance reduces from 747.84 to 22.66  $\Omega/\square$  with 0.3 – 1.5 vol% of CNTs addition. The increased electrical conductivity enables the potentiality of plastron regeneration capabilities in the SHPo drag-reduction.

© Copyright 2022 by Md Didarul Islam

All Rights Reserved

Template-free Scalable Fabrication of Linearly Periodic Microstructures

by  
Md Didarul Islam

A dissertation submitted to the Graduate Faculty of  
North Carolina State University  
in partial fulfillment of the  
requirements for the degree of  
Doctor of Philosophy

Mechanical Engineering

Raleigh, North Carolina  
2022

APPROVED BY:

---

Dr. Jong Eun Ryu  
Committee Chair

---

Dr. Mohammed Zikry

---

Dr. Yong Zhu

---

Dr. Saad Khan

## **DEDICATION**

*To my beloved parents, family, and my wife for their love and support*

## **BIOGRAPHY**

Md Didarul Islam (Didar) pursued his Ph.D. in the mechanical engineering department at North Carolina State University under the supervision of Dr. Jong Ryu. He worked as a research assistant at the Composite Design and Manufacturing Lab. Didar is passionate about solving materials science and mechanical engineering problems. Specifically, he has expertise in synthesizing polymeric composite materials for infrared optics and utilizing creative nanofabrication techniques to manufacture optical devices. Some of these efforts have great potential to reduce the high fabrication cost of conventional inorganic materials. Didar is also interested in developing low-cost scalable manufacturing techniques to fabricate periodic microstructures for large-area substrates. Applications include superhydrophobic, self-cleaning, and drag-reduction surfaces with multifunctional capabilities.

Before coming to North Carolina state university for a Ph.D., Didar completed his master's degree in computational science from the University of Texas at El Paso, where he worked in collaboration with the Mechanical engineering department to learn about applying the design of experiments and data analytics in additive manufacturing of piezoelectric pressure sensors.

Before that, Didar completed his bachelor's degree in Mechanical engineering from the Bangladesh University of Engineering and Technology and worked for an oil and gas company named Tullow oil inc. He worked for two years in the production team. Working in the industry made him realize the importance of making data-driven decisions. He decided to come back to school first to learn about applying data analytics and the design of experimental approaches in experimental research. Secondly, pursuing a Ph.D. in mechanical engineering allowed him to acquire more fundamental knowledge and technical skills. To summarize, his education, research,

and work experience helped him learn; how to transform a real-world challenge into a scientific problem and solve them in collaboration with innovative engineering methods.

The following publications were authored or co-authored by Didar in peer-reviewed journals or conference proceedings during his doctoral study at North Carolina State University.

### **Journal Articles**

1. M.D. Islam, J.E. Ryu et al., Enhanced mid-wavelength infrared refractive index of organically modified chalcogenide (ORMOCHALC) polymer nanocomposites with thermomechanical stability, *Opt. Mater.* 108 (2020) 110197.
2. M.D. Islam, J.E. Ryu et al., Design of High Efficient Mid-Wavelength Infrared Polarizer on ORMOCHALC Polymer, *Macromol. Mater. Eng.* 305 (2020) 2000033.
3. M.D. Islam, J.E. Ryu et al., Physics-based computational method predicting the dielectric properties of polymer nanocomposites, *Applied Composite Materials* (2022)
4. M.D. Islam, J.E. Ryu et al., Template-free scalable fabrication of linearly periodic microstructure by controlling ribbing defects phenomenon during forward roll coating. (*Manuscript under review in Advanced Materials*)
5. S. Liu, M.D. Islam, J.E. Ryu et al., Novel computational design of high refractive index nanocomposites and effective refractive index tuning based on nanoparticle morphology effect, *Compos. Part B Eng.* (2021) 109128.
6. A.J. Berndt, J. Hwang, M.D. Islam, J.E. Ryu et al., Poly(sulfur-random-(1,3-diisopropenylbenzene)) based mid-wavelength infrared polarizer: Optical property experimental and theoretical analysis, *Polymer.* 176 (2019) 118–126.

## Conference Proceedings

1. M.D. Islam\*, J.E. Ryu et al., Template-free scalable fabrication of linearly periodic microstructure by controlling ribbing defects phenomenon during forward roll coating, *Proc. NAMRC, SME*, Purdue, July 2022.
2. M.D. Islam\*, J.E. Ryu et al., Tunable mid-wavelength infrared (MWIR) polarizer by ORMOCALC composite with improved thermomechanical stability, *Proc. SPIE, SPIE-Intl Soc Optical Eng*, San Diego, 2021: p. 73.
3. M.D. Islam\*, J.E. Ryu et al., Highly efficient mid-wavelength infrared (MWIR) polarizer by ORMOCALC composite with improved thermomechanical stability and spectral selectivity, *Proc. ASME, IMECE 2021*, online, Nov. 2021.
4. S. Liu, M.D. Islam, J.E. Ryu et al., Novel computational design of high refractive index nanocomposites and effective refractive index tuning based on nanoparticle morphology effect, *Proc. SPIE, SPIE-Intl Soc Optical Eng*, San Diego, 2021: p. 73.
5. S. Liu, M.D. Islam, J.E. Ryu et al., Novel Nanocomposite Refractive Index Tuning Mechanism Based on Controlling Embedded Particle Morphology, *Proc. ASME, IMECE 2021*, online, Nov. 2021.
6. S. Chockalingam, M.D. Islam\*, J.E. Ryu et al., Fabrication of Bioinspired Micro/Nano Textured Rough Surfaces Through the Scalable Roll Coating Process, *Proc. ASME, IMECE 2021*, online, Nov. 2021.

## ACKNOWLEDGMENTS

First and foremost, I am thankful to have Dr. Jong Eun Ryu as my mentor and research supervisor. Thanks for choosing me to be your student and providing me with the excellent opportunity to work with you. He introduced me to optics, nanotechnology, multifunctional composite materials, and new and emerging creative manufacturing technologies. Looking back on my Ph.D. journey makes me more humble and thankful to have him as my mentor. I have received ample opportunities to learn about advanced technologies, making me more confident moving forward with my graduation. Without his persistent guidance and support, this research work and my prior accomplishments would not be possible. I have received his utmost support and best advice from the first day in Raleigh, both in school and outside.

I would also like to thank my committee members, Dr. Mohammed Zikry, Dr. Yong Zhu, and Dr. Saad Khan, for their insightful thoughts and suggestions for my research. The guidance and effort from all the committee members made this research work a success.

I want to thank all the excellent people I have collaborated with. I was fortunate enough to work with fellow NC State students, including Sipan Liu, Masrur Morshed Nahid, Reece Henry, Laine Taussig, Himendra Perera, Matthew Phillips, Muh-Jan Chen, Yuxuan Liu, and Benjamin Black. Working with such bright minds helped me learn new knowledge beneficial for the research. I would also like to thank Chuck Mooney of AIF and Greg Allion, who I found extremely helpful in conducting my research. I want to thank Dr. Darryl Boyd of the US Naval Research Laboratory for providing collaboration opportunities in promising optical materials research.

I am thankful to the Mechanical and Aerospace Engineering department at North Carolina State University for giving me the opportunity to pursue my Ph.D. in this reputed

program. The department also gave me teaching opportunities and supported me financially to continue my study and research work at NC State. I also highly appreciate National Science Foundation (grant no. 2031558) supporting this research and giving me financial support.

Last but not least, I would like to thank my family and wife for their unconditional love and support; without them, I would not be the person I am today.

## TABLE OF CONTENTS

LIST OF TABLES .....	x
LIST OF FIGURES .....	xi
<b>Chapter 1: Introduction</b> .....	1
1.1 Motivation.....	1
1.2 Research Objectives.....	5
1.3 Research Planning.....	6
1.4 Dissertation Outline .....	7
<b>Chapter 2: Literature Review</b> .....	9
2.1 Drag Reduction by Periodic Microstructures .....	9
2.1.1 Wettability and Superhydrophobicity .....	9
2.1.2 Conventional Drag Reduction Mechanism.....	13
2.1.3 Superhydrophobic Drag Reduction.....	16
2.1.4 Current Methods to Manufacture Superhydrophobic Surfaces .....	20
2.2 Ribbing Instabilities .....	23
2.2.1 Interfacial Forces in Ribbing .....	23
2.2.2 Ribbing of Newtonian vs. Non-Newtonian Materials .....	26
<b>Chapter 3: Coating Paste Formulation and Characterization</b> .....	29
3.1 Background .....	29
3.2 Experimental Methods .....	29
3.3 Results and Discussion .....	32
3.4 Conclusions.....	37
<b>Chapter 4: Computational Fluid Dynamic study of Ribbing formation</b> .....	40
4.1 Background.....	40
4.2 Experimental Methods .....	40
4.3 Results and Discussion .....	41
4.4 Conclusions.....	48
<b>Chapter 5: Manufacturing of Periodic Microstructure by Roll-Coating</b> .....	49
5.1 Background.....	49
5.2 Experimental Methods .....	49
5.3 Results and Discussion .....	52
5.4 Conclusions.....	66
<b>Chapter 6: Multifunctional Applications of Superhydrophobic Surfaces</b> .....	67
6.1 Background.....	67
6.2 Experimental Methods .....	67
6.3 Results and Discussion .....	70
6.4 Conclusions.....	76
<b>Chapter 7: Conclusions and Future Works</b> .....	78
7.1 Conclusions.....	78

7.2 Future Works .....	79
<b>References</b> .....	<b>80</b>

## LIST OF TABLES

Table 1.1	Polar and dispersive surface energy components of the test liquids .....	31
Table 1.2	Surface energy measurement based on the Owens-Wendt model .....	34

## LIST OF FIGURES

Figure 1.1	Schematic of the ribbing formation phenomenon on a two-roll coater.....	3
Figure 1.2	Schematic of the planning of the research.....	7
Figure 1.3	Outline of the dissertation .....	8
Figure 2.1	(a) Images of Superhydrophobic lotus leaf along with magnification SEM images (inset image is a water droplet) [52]. (b) SEM image of the surface of a red rose petal (inset image shows the rose and water droplet on the surface when flat, and when upside down) [52]. (c) Photograph of cicada with SEM micrograph image [52]. (d) Photo of tokay gecko and its foot with adhesive lamellae's microstructures and spatula [52]. (e) Photograph of antifogging mosquito eyes and SEM image [52]. (f) Namib beetle and their superhydrophobic-superhydrophilic skin [55] .....	11
Figure 2.2	The applications of superhydrophobic surfaces [56] .....	13
Figure 2.3	The wetting models of (a) Young's, (b) Wenzel, and (c) Cassie-Baxter [61]. (d) The Kao diagram [62] .....	15
Figure 2.4	(a) Mitsubishi air lubrication system [63]. (b) The sailing experiment of a boat coated with superhydrophobic coating and a reference boat without any coating [64]. (c) The velocity of the bare/coated model boats with respect to the power supply [64].....	17
Figure 2.5	Parameters that affect liquid flow over a SHPo surface are defined as follows: (a) Velocity distribution on a SHPo surface, displaying a slip velocity ( $u_s$ ) and an effective slip length. (b) Water on a vertically structured roughness, exhibiting the air-water interface on or in the roughness parts. (c) Water on a random roughness, defining the average roughness height ( $k_a$ ) and average roughness pitch ( $P_a$ ), which is the same as the average roughness width ( $w_a$ ), along with the average wetted roughness height ( $h_a$ ) and average interface width ( $s_a$ ) with the subscript 0, 1, 2, and wet [72].....	19
Figure 2.6	Experimental studies on the SHPo drag reduction in turbulent flows presented with geometry and effective drag-reduction (DR%) [72] .....	20
Figure 2.7	(a) Photolithography process overview [53]. (b) Nanoimprint lithography (NIL) process overview [74]. (c) Schematic illustration of the durable SHPo coating fabricated process [75].....	22
Figure 2.8	The unstable growth of voids or cracks can be studied by (a) pulling fluid from between glass plates, (b) pulling or wedging the plates apart, (c) moving a roller over a glass plate, and (d) peeling adhesive tapes from glass plates [29].....	24

Figure 2.9	(a) Schematic diagram showing the relationship between the pressure gradient at the advancing front and surface energy. (b) Schematic of the velocity and pressure gradient component radiating outward in the $z$ -direction, tip splitting, and tip coalescence [76] .....	26
Figure 2.10	(a) Eccentric cylinder coating apparatus. (b) Comparison of the critical capillary number ( $Ca^*$ ) in the forward roll coating geometry versus the dimensionless gap ratio ( $d/R$ ) from the experimental measurements for a range of fluids with varying elasticity. (c) Eccentric cylinder forward roll coating instabilities for Newtonian fluids. (d) Roll coating instabilities in non-Newtonian fluids [77] .....	28
Figure 3.1	(a) Coating paste formulation. (b) Processed CNT-PDMS with varying vol%. (c) CNT distribution in PDMS .....	30
Figure 3.2	(a) The test materials are analyzed for contact angle for various reference liquids, and the result in data are fitted in the Owens-Wendt model. (b) The surface energy components of the materials are based on the fitting.....	35
Figure 3.3	(a) Storage Modulus ( $G'$ ) and oscillation stress vs. oscillation strain (%) to identify the linear viscoelastic region (LVE). (b) Storage Modulus ( $G'$ ), and loss modulus ( $G''$ ) vs. angular frequency (rad/s). (c) Complex Viscosity ( $\eta^*$ ) vs. angular frequency .....	38
Figure 3.4	(a) Elastic stress vs oscillation strain (%). (b) Yield stresses ( $\sigma_y$ ) of the composites vs. nanoparticles vol% .....	39
Figure 4.1	Schematic of the CFD simulation configuration of the two-roll coater in (a) 3-dimension. (b) 2-dimension. (c) The fluid-flow mesh boundary conditions.....	41
Figure 4.2	(a) Ribbing instabilities observed in 3D. (b) CFD Model validation with experimental results.....	44
Figure 4.3	Schematic of the fluid cross-section of the CFD model.....	44
Figure 4.4	(a) Absolute pressure and fluid velocity at the direction of fluid flow ( $x$ - $x$ direction) for $R/d = 31.75, 36.29, 42.33, 50.8,$ and $63.5$ at a roller speed of 10 rpm. (b) The fluid velocity profile in the $x$ - $x$ direction. (c) Shear rate ( $\dot{\gamma}$ ) generated due to the velocity gradient at the $x$ - $x$ direction. (d-f) Pressure gradient $dp/dx$ in the flow direction, $\dot{\gamma}$ , and $\tau_w$ in various roller speeds (30, 50, 80, and 100 rpm at $R/d$ of 31.75, 36.29, 42.33, 50.8, and 63.5) .....	45
Figure 4.5	(a-h) Ribbing instability of PDMS under various process conditions. (i) PDMS flattens after a few seconds .....	46

Figure 4.6	(a) Experimental data of PDMS ribbing wavelengths vs. various process conditions. (b-d) The experimental wavelengths of PDMS are plotted against $dp/dx$ , $\dot{\gamma}$ , and $\tau_w$ calculated from the CFD analysis .....	47
Figure 5.1	(a) Two roll coating machines. (b) Forward roll coating of composite paste. (c) Fabricated sample after heat-cure. (d-e) SEM image showing the micro-trench formation and the peak-formations due to filamentation on a linearly periodic sample. (f-g) SEM images show high aspect-ratio leaf-vein shape samples, as the $R/d$ crosses a critical value .....	50
Figure 5.2	(a) 3D images of the samples by a confocal laser microscope. (b) Top view of the scanned surface with horizontal and vertical lines (lines not drawn to scale) to estimate the periodicity of the samples. (c) Topography of a sample horizontal line showing the waviness of the surface .....	51
Figure 5.3	(a) Filamentation phenomenon on 0.27 vol% CNT-PDMS composite roll-coating. (b) Filament initiation. (c) Filament elongation. (d) Filament breakage ....	53
Figure 5.4	High-speed images were captured for roll coating of 0.54 vol% CNT-PDMS for various roll-coating speeds of 20 rpm, 60 rpm, and 100 rpm for $R/d$ of (a) 50.80, (b) 63.5, and (c) 84.67. The ribbing was relatively stable at a lower speed, whereas the higher speed incurred more filamentation and tip-splitting .....	54
Figure 5.5	Patterns classification occurring by ribbing and filamentations. The patterns begin from linear to tree branches, and finally, leaf-vein-shaped random structure .....	55
Figure 5.6	(a) Photographs of 6.9 vol% of $\text{SiO}_2$ – S186 samples for various $R/d$ at a roller speed of 10 rpm. (b) Photographs of 0.98 vol% of CNT – S186 samples for various $R/d$ .....	57
Figure 5.7	Laser confocal images of (a) 6.9 vol% of $\text{SiO}_2$ – S186 and (b) 0.98 vol% of CNT – S186 samples for various $R/d$ . (c) Measured ribbing wavelengths of the sample vs. $R/d$ .....	57
Figure 5.8	SEM images of 1.65 vol% CNT-PDMS samples at 50 rpm speed, and (a) $R/d = 63.5$ , (b) $R/d = 84.67$ , and (c) $R/d = 101.6$ .....	58
Figure 5.9	(a) Photographs of fabricated samples using $R/d = 56.44, 63.50, 72.57, 84.67,$ and $101.60$ . (b-f) SEM images of samples fabricated with the same $R/d$ ratios; (g) High-magnification SEM image of an individual peak of the samples showing CNT distribution in PDMS .....	60
Figure 5.10	Photographs and SEM images of leaf-vein shaped samples fabricated at 40 and 80 rpm at $R/d$ of 101.6 and 127 .....	61

Figure 5.11 Ribbing wavelength ( $\lambda_{Ribbing}$ ) and filamentation wavelengths ( $\lambda_{Filamentation}$ ) of the fabricated samples vs. $R/d$ .....	62
Figure 5.12 (a) Water contact angle measurements boxplot at five different locations of each sample. (b) Wenzel roughness factor vs. $R/d$ .....	63
Figure 5.13 CFD simulation results for roll-coating of 1.93 vol% CNT-PDMS under various process conditions (a) $\lambda_{Ribbing}$ , $dp/dx$ , and shear rate vs. $R/d$ . (b) $\lambda_{Ribbing}$ and wall shear stress vs. shear rate.....	65
Figure 6.1 (a) The free-body diagram of the drag-reduction experimental setup. (b) Miniature model boats with standard loads. (c) Experimental setup.....	68
Figure 6.2 Mechanical scratch testing of the samples showing cohesive and adhesive failure (image reconstructed based on [103,104]).....	69
Figure 6.3 (a) Sample preparation of CNT-PDMS composite sample for the electrical measurement. (b) Electrical conductivity measurement setup using a custom-made 4-point probe following the Van-der-Pauw method.....	70
Figure 6.4 Velocity profile of model boat with and without the linear micro-structured sample.....	72
Figure 6.5 (a) Entrapped air underneath the SHPo surface skin attached to the model boat. (b) Loading test for the model boat with SHPo surface .....	73
Figure 6.6 Sheet resistance $R_s$ of the CNT-PDMS composite samples fabricated in the current study. (b) Mechanisms of regenerative plastrons by work of Lee et al. [111] .....	75
Figure 6.7 Scratch test of (a) 2.08 vol% CNT-PDMS and (b) PDMS-Sylgard 184 sample.....	76

## CHAPTER 1 : Introduction

### 1.1 Motivation

Regarding micro/nano-scale structures, nature has been far ahead of human-developed technology. With applications that include superhydrophobicity [1,2], self-cleaning [3], anti-icing [3], anti-biofouling [4], biological sensors [4], and radiative cooling [4], mimicking nature's micro/nano-scale structures are becoming integral to current research endeavors. These micro/nano-scale structures have provided biological systems with unique functionalities for millions of years [5–7]. For example, Namib Desert Beetles use the superhydrophobic-superhydrophilic micropatterned skin to harvest water from fog [8–10]. Plants such as lotus utilize leaf microstructures to influence wetting behavior and enable self-cleaning [8,11]. Sharks' unique skin morphology augments the near-wall vorticity during turbulent flow. This augmentation reduces the skin-friction and enables sharks to be one of the most efficient swimming species in the ocean [12–14]. These drag-reducing microstructures are of particular interest to the scientific community. Thus, researchers have focused on periodic microstructures aligned in the flow direction, similar to sharkskin. In prior modeling and experimentation, researchers have decreased drag by using different variations of linear periodic microstructures. For example, Xu et al. developed a series of linear micro-trenches demonstrating a maximum drag reduction of approximately 30% in high Reynolds number applications [15]. Additionally, Park et al. studied the impact of grating parameters on drag reduction and demonstrated a maximum drag reduction of 75% [16].

Lithography is one of the standard manufacturing processes for superhydrophobic periodic microstructures [15–17]. However, one primary limitation of this method is that the size of the superhydrophobic (SHPo) surface is limited by the substrate size, which in the case of a

silicon substrate, ranges from 10 to 30 cm. This is far smaller than actual boats that are larger in magnitude ranging from several meters to hundreds of meters. The photolithography process is impractical to manufacture large-area substrates due to high cost and low throughput.

Nanoimprint lithography utilizing a polydimethylsiloxane (PDMS) stamp has been utilized to replicate the hydrophobic micropattern of a lotus leaf [18]. Although a high water contact angle was achieved, the method cannot still be utilized on a large scale. Other related technologies such as micro-coining, bio-pattern imprinting, laser cutting, and 3-dimensional (3D) printing also have critical limitations as these methods are time-consuming, expensive, and complex, compromising the scalability [19–23]. Therefore, creating a scalable manufacturing process to produce SHPo micro-grating structures is necessary for practical drag reduction applications.

The challenge of scalable manufacturing of micro-trench structures has motivated the authors to consider a more insightful look into a common roll-coating defect known as ribbing (Figure 1.1), where spatially periodic patterns appear transverse to the roll-coating direction [24–27]. During the roll-coating process, a positive pressure gradient is developed in the downstream meniscus of the coating fluid [28]. The flow becomes unstable when the pressure gradient exceeds a critical value, and a finger-like growth is observed [29,30]. The ribbing instability is undesirable in general roll coating applications, such as painting [31,32], polymer thin films [33,34], and flexography printing [35,36]. However, carefully controlling these ribbing patterns could assist in replicating periodic microstructures obtained by the traditional methods.

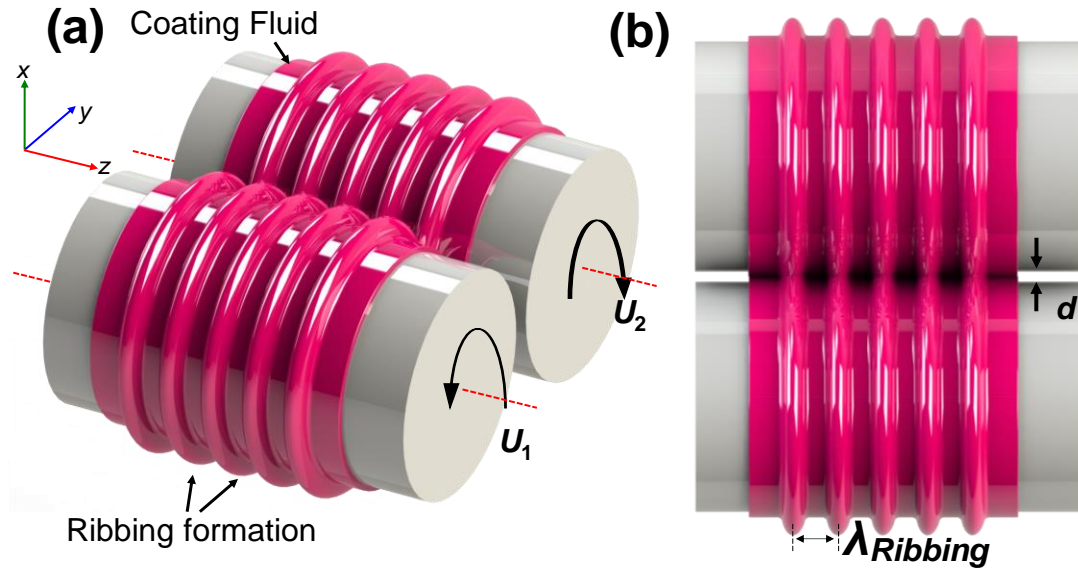


**Figure 1.1** Schematic of the ribbing formation phenomenon on a two-roll coater.

The ribbing behavior of Newtonian and non-Newtonian fluids has been studied through experimental and computational models aiming to minimize roll-coating defects [24–27,37]. It was found that the ribbing periodicity or wavelength ( $\lambda_{Ribbing}$ ) and amplitude have a strong relationship with material properties as well as process parameters, including the surface energy  $\gamma$ , viscosity  $\eta$ , roller radius  $R$ , roller gap  $d$ , and roller speed  $U$  [29,38–40]. For a Newtonian fluid, the onset condition of the ribbing instability was found describable by two dimensionless parameters: the capillary number  $Ca = \eta U / \gamma$  and the geometric factor  $R/d$ . The critical capillary number  $Ca^*$  showed a linear proportionality with the geometric factor  $R/d$  for Newtonian fluids [25,27,30,41–43].

On the other hand, the critical capillary number for non-Newtonian fluids is much lower than for Newtonian fluids [42]. However, unlike Newtonian fluids, the theoretical prediction of the  $Ca^*$  in viscoelastic fluids is not available. There remains a lack of understanding of how the ribbing occurs in coating applications. López et al. controlled the elasticity with the

concentration of polymer molecules in a Newtonian fluid (Glycerol/Water) and showed similar trends in the  $Ca^*$  and the normal stress parallel to the flow as the polymer concentration increases [42]. The results imply that the elastic nature of the viscoelastic fluid increases the stress in the flow direction by restricting the flow and causes ribbing instability at a slower roller speed, i.e., a lower capillary number. According to computational simulations, Zevallos et al. showed that at any given  $Ca$ ; there is a critical Weissenberg number  $Wi$  above which the flow becomes unstable [28]. Most research on non-Newtonian elastic fluid has focused on identifying the critical capillary numbers or threshold conditions to initiate the instabilities. However, the fluid propagation and ribbing formation beyond the onset conditions are yet to be explored [44–46].

An in-depth investigation of the physical properties of the roll-coating pastes and how it influences the ribbing instabilities in a roll-coating process can achieve scalable manufacturing of periodic micro-patterns surface. Unlike the roll coating applications, this study focuses on investigating beyond the onset conditions and carefully controlling the process parameters to manufacture periodic microstructures by controlling the instabilities. One phenomenon observed for most coating materials is that ribbing patterns tend to flatten when the roller stops, as the surface tension dominates over viscosity. However, to manufacture periodic microstructures, retaining the deformed shape when the rollers stop is necessary. The surface flattening can be avoided by tailoring the coating liquid's viscoelastic properties. One method to engineer the viscoelasticity of the polymers is nanoparticle addition [47–49]. The desired materials will behave only like a fluid above the yield stress but act solid when the stress is unloaded. Previous studies suggest that the inclusions' volume fraction and geometry influence the composite's

rheological properties. Notably, composites with cylindrical or high aspect ratio nanoparticles are more likely to possess yield stress than spherical particles [50,51].

In this study, an in-depth investigation of the roll-coating parameters to manufacture linear periodic microstructures is conducted. First, the ribbing formation of PDMS (Sylgard 184, Dow Corning) in a forward roll coating for various process parameters was investigated. The finger-like ribbing was observed during the roll coating. However, when the rollers stopped, the liquid surface flattened due to the surface tension. Thus, a viscoelastic composite paste was formulated by adding cylindrical nanoparticles (carbon nanotubes, CNTs) to PDMS. This helped to achieve a yield behavior and avoid surface tension-driven flattening. Finally, utilizing the composite paste, linearly periodic microstructures were manufactured by the roll-coating process. The physical properties of the coating paste and computational fluid dynamics (CFD) analysis of the roll coating parameters helped to successfully manipulate the ribbing instabilities to manufacture periodic microstructures. The manufactured samples were then applied to a miniature boat to measure the drag reduction and load testing. In addition, the mechanical and electrical properties of the CNT-PDMS composite were also evaluated for multifunctionality and robustness.

## **1.2 Research Objectives**

This research aims to establish a scalable roll-coating process for SHPo surfaces that provide hydrodynamic drag reduction (DR). The recent first success of obtaining DR in field conditions indicates that the microstructure on the SHPo surface should be a periodic pattern of micro-trenches [15]. However, manufacturing scalability and cost are the main barriers to realizing a regular microstructure over a large area necessary for real-world applications. To break the barrier, we propose manufacturing micro-gratings by utilizing an inherent instability in

viscoelastic polymer films, known as ribbing instability, during roll coating. To this end, there are three research objectives we want to achieve.

1. Develop a CFD model to predict the ribbing pattern and critical parameters defining the coating paste properties.
2. To test the hypothesis that the ribbing pattern, a linear 3D microstructure occurred in the roll-coating process for polymers. Validate the CFD model using the experimental results.
3. To establish the fundamental knowledge that relates the roll-coating process parameters to the ribbing patterns or micro-grating geometries.
4. Fabricate micro-grating geometries utilizing the roll-coating process and evaluate surface robustness, superhydrophobicity, and drag reduction capability through experiments.

### **1.3 Research Planning**

The first step of the research will focus on manufacturing composite coating pastes by adding nanoparticles to the polymer. The prepared materials' physical properties, such as storage modulus, loss modulus, and surface energy, will be next investigated experimentally concerning particle concentration and geometry. The coating pastes will be utilized in the roll-coating process to investigate the ribbing phenomenon by varying the process parameters such as roller speed and distance. Finally, multiple imaging techniques will analyze the ribbing patterns, including Scanning electron microscope (SEM) and laser confocal microscope. The experiment will be conducted in a feedback loop assisted by a CFD model to fine-tune the materials

composition and process parameters to achieve desired morphology of the roll-coated surface (Figure 1.2).

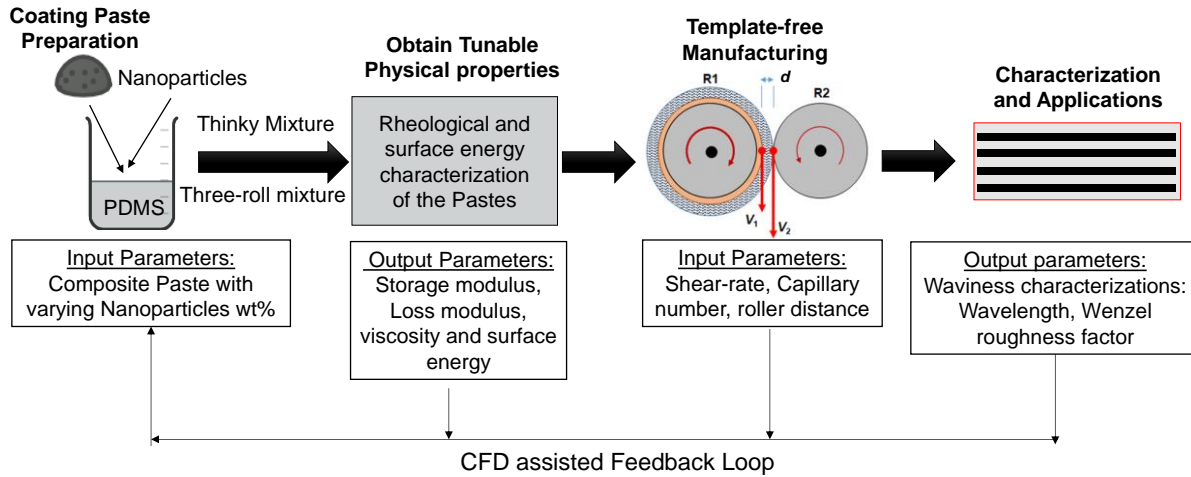


**Figure 1.2** Schematic of the planning of the research.

## 1.4 Dissertation Outline

The dissertation first consists of a literature review related to surface wettability, conventional manufacturing techniques of superhydrophobic structure, and applications in frictional drag reduction. Next, the ribbing instabilities were discussed for Newtonian and non-Newtonian materials. The coating materials' physical properties, such as the surface energy and rheological analysis, are discussed in the next chapter. Next, the collected materials data was utilized to build a computational fluid dynamic model of forward roll coating. The simulation was conducted for PDMS first, next was validated by experimental results, and critical process parameters related to the properties of the material were evaluated. The periodic micro-grating structures fabrication was discussed next, including the fabrication of linear, semi-linear, and leaf-vein-shaped samples. The hydrophobicity and surface morphology of the samples were

evaluated. Finally, the fabricated samples were put into practical drag-reduction experimentations. The samples were also tested for multifunctionality. In the final section, the summary of the study and future tasks are discussed. Figure 1.3 shows the critical research tasks in sequential order.

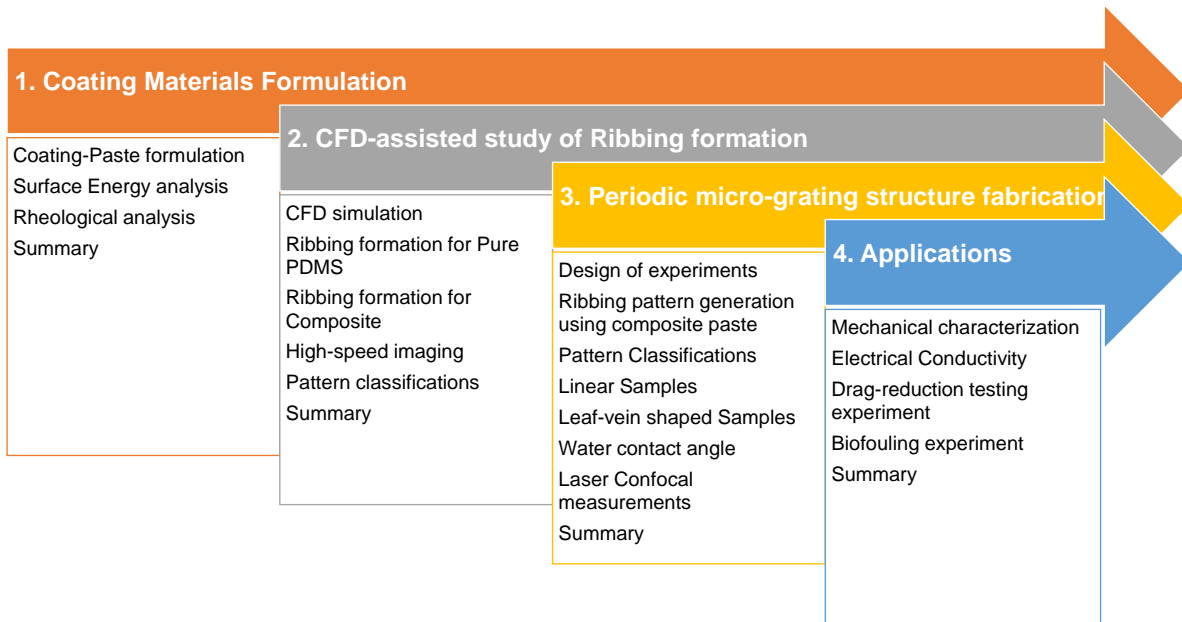


**Figure 1.3** Outline of the Dissertation

## CHAPTER 2 : Literature Review

### 2.1 Drag Reduction by Periodic Microstructures

#### 2.1.1 Periodic Micro-/Nano-structures in Nature

Biological systems have optimized their complex hierarchy of structured structures over billions of years of evolution and natural selection to achieve maximum performance in responding to and adjusting to changing environmental conditions. With applications that include superhydrophobicity [1,2], self-cleaning [3], anti-icing [3], anti-biofouling [4], biological sensors [4], and radiative cooling [4], mimicking nature's micro/nano-scale structures are becoming integral to current research endeavors. Plant leaves have a unique wettability or water repellency on their surfaces. Water droplets cannot stick firmly to the surface of plants with repellent leaves (or petals), forcing them to bounce off or roll away, eliminating dirt particles from the leaves or petals on a regular basis. The "lotus effect" or "self-cleaning" is the name for this feature. This non-wetting ability is caused by micro- and nanoscale hierarchical roughness in the form of cilium-like nanostructures placed on top of randomly dispersed micro-papillae, as illustrated in Figure 2.1a [52].

The petal effect refers to how some plants (such as roses) can keep a water droplet from rolling off their petals and keep it spherical even when the petal is turned upside down (Figure 2.1b). Micropapillae with manifolds on the top form red rose petals. The petals of the Chinese Kafir Lily are made up of tessellated hexagons with an average side length of 75  $\mu\text{m}$  and strip width of 780 nm in each hexagon, whereas the petals of the sunflower are made up of parallel lines with an average diameter of 15  $\mu\text{m}$  and a helix width of 2.5  $\mu\text{m}$  on each line. Water droplets are projected to penetrate the petal's larger-scale grooves, producing the Cassie-impregnating wetness regime and causing water droplet sticking [53].

Figure 2.1d shows the gecko foot, which comprises hundreds of nanoscale spatula (200–500 nm in diameter) that are broken into innumerable well-aligned tiny keratinous hairs termed setae (30 – 130  $\mu\text{m}$  in length and 5  $\mu\text{m}$  in diameter). The spatulas bend when they touch any surface, allowing molecular contact across broad regions and transforming weak van der Waals interactions into massive attractive forces that allow the gecko to climb vertical walls or over ceilings [53]. Cicada has a photonic structure giving them anti-reflection capabilities (Figure 2.1c). Its wings have ordered hexagonal close-packed arrays of pillars with a spacing of about 190 nm. The height of the pillars is about 400 nm with a bottom diameter of 80 – 150 nm. The effective refractive index can be estimated at any depth based on the air and bulk materials refractive index, which gives a gradient of refractive index, giving an anti-reflection surface [54].

Gao et al. used soft lithography and low-surface-energy fluoroalkyl silane modification to create artificial mosquito eye mimics with superhydrophobic and antifogging capabilities [54]. A stamp was created by replicating a sparsely packed circular hexagonal microstructure on PDMS, then modifying it with self-assembled fluoroalkyl silane and hot pressing it onto a monolayer of silica nanospheres, resulting in homogenous compound eye-like nipple structures (Figure 2.1e). Fog is an alternative water source in the Namib Desert [55]. Darkling beetles (Tenebrionidae) use this to harvest fog water, and they use several techniques to do it (Figure 2.1f) [55]. Some dig sand trenches, while others utilize their bodies as fog collectors, adopting the classic fog-basking posture. On the ridges of the sand dunes, two *Onymacris* beetle species have been recorded fog-basking. These beetles have smooth elytra surfaces, but another species with bumpy elytra is said to have specialized adaptations that aid in fog-basking water collection. A study of the elytra of beetles in the genus *Stenocara* [54] revealed how fog water creates huge droplets on a beaded surface. Water delivered by the fog rests on the hydrophilic peaks of the

beetle's smooth bumps on the elytra and forms fast-growing droplets that roll down towards the head once large enough to move against the wind [54].

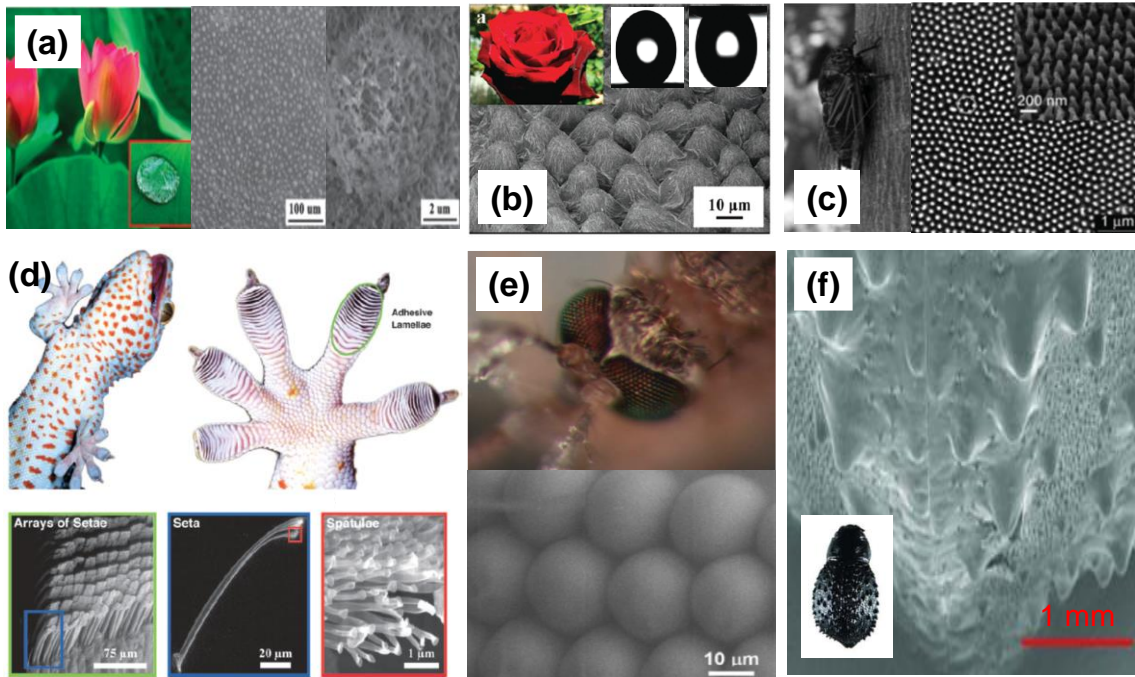


**Figure 2.1** (a) Images of Superhydrophobic lotus leaf along with magnification SEM images (inset image is a water droplet) [52]. (b) SEM image of the surface of a red rose petal (inset image shows the rose and water droplet on the surface when flat, and when upside down) [52]. (c) Photograph of cicada with SEM micrograph image [52]. (d) Photo of tokay gecko and its foot with adhesive lamellae's microstructures and spatula [52]. (e) Photograph of antifogging mosquito eyes and SEM image [52]. (f) Namib beetle and their superhydrophobic-superhydrophilic skin [55]

With advancements in the fabrication of superhydrophobic surfaces on diverse metal substrates, these periodic micro/nano-structures have inspired scientists to produce

functionalized metal surfaces with exceptionally low surface energy and are slowly finding their way into industries and everyday life (Figure 2.2) [56]. The high surface-to-volume ratio of a microfluidic device, for example, has a major impact on flow behavior, resulting in significant pressure loss. In order to efficiently decrease pressure loss, superhydrophobic coatings are applied to microfluidic devices or microchannels [57]. It is widely known that ice and snow formation reduces the efficiency of solar cells and wind turbines operating in harsh circumstances [58], and the problem of removing ice from surfaces has received much attention. There are two types of procedures for removing ice from surfaces: active and passive. Active methods include heat treatments, mechanical scraping, and the use of de-icing chemical compounds. After ice development, the active approach removes the ice from the surfaces, which requires a lot of work. On the other hand, the passive technique inhibits ice production or ice adhesion to surfaces even when icing occurs. Because of the decreased ice adhesion strength, the passive approach may successfully remove ice from surfaces with minimal energy consumption, resulting in energy savings. The passive technique based on a superhydrophobic surface can limit ice adhesion to the surface and avoid ice formation. When an airplane travels through freezing temperature zones, icing occurs, and ice adheres to the plane's surface, posing a danger of catastrophic failure [59]. The features of the superhydrophobic surface can be used to reduce drag in laminar or turbulent flows. For example, pressure loss via tubes or channels with superhydrophobic surfaces may be successfully decreased, and the convective heat transfer coefficient can be enhanced to some extent, ascribed to fluid velocity acceleration [60]. Other industries might benefit from the superhydrophobic surface. For example, ice slurry may be used as a secondary-loop refrigerant, which can be used as a heat transfer fluid and energy storage medium in an air conditioning system to save energy. The ice slurry can be made with a

generation system that has a superhydrophobic surface, which means the ice slurry particles are less likely to stick to the surface or obstruct the tubes. As a result, the superhydrophobic surface might be helpful in the production of ice slurry [60].

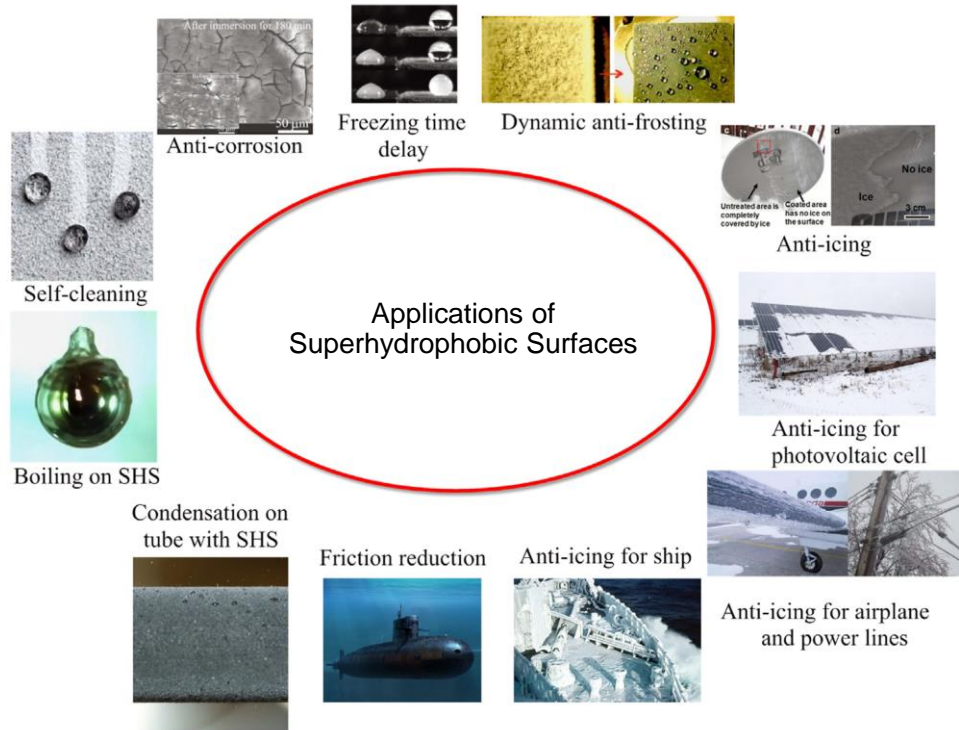


**Figure 2.2** The applications of superhydrophobic surfaces [56].

### 2.1.2 Wettability and Superhydrophobicity

To understand the wetting behavior of a surface and the effect of periodic micro/nanostructures, we pay attention to several well-known wetting models. When a liquid droplet comes into touch with a solid surface, most of the time, this surface interaction results in the droplet spreading on the solid surface and forming a spherical cap somewhat bent by gravity. The liquid-surface contact determines the extent to which the droplet spreads on the surface. These interactions and their outcomes are described by wetting theory (Figure 2.3). Molecules in a liquid droplet are held together by intermolecular forces, which are balanced in all possible

spatial directions for molecules in the droplet's core. In the outer ridges of the droplet, however, a greater number of molecules are positioned towards the center of the droplet than towards the edge, resulting in a net force drawing the outer molecules towards the droplet's center. As a result, energy input is required to transport a molecule from the droplet's center to the less bound outside region, overcoming the corresponding potential energy gap. Furthermore, because the droplet is in touch with a surrounding vapor, solid, or other liquid, molecules inside the droplet are subjected to external forces, which alter the work required for displacement. The work required for displacement per unit surface is specified as the interfacial surface tension ( $\gamma$ ), which defines a liquid's tendency to reduce its surface area.

Young used a three-phase model and assumed a droplet small enough for gravity to be negligible to derive a relationship between the contact angle ( $\theta_y$ ) of a droplet on a smooth surface and the surface tensions of the liquid-vapor ( $\gamma_{lg}$ ), liquid-solid ( $\gamma_{sl}$ ), and solid vapor ( $\gamma_{sg}$ ) interfaces [61].

$$\cos \theta_y = \frac{\gamma_{sg} - \gamma_{sl}}{\gamma_{lg}} \quad (2.1)$$

However, when there is a roughness on the solid surface, Young's equation no longer holds. The surface roughness alters the wetting behavior of liquid on the surface. Wenzel was able to correlate the apparent CA ( $\theta_w^*$ ) (Figure 2.3b) of the droplet on the structured surface to Young's contact angle ( $\theta_y$ ) the droplet would have on an unstructured solid of the same material by introducing a roughness parameter ( $r$ ), which is defined as the ratio of actual surface area to the projected area of the surface [61].

$$\cos \theta_w^* = r * \cos \theta_y \quad (2.2)$$

$$r = \frac{\text{Curved surface area}}{\text{Projected surface area}}$$

The Wenzel model considers the liquid completely wets the surface. However, if the surface is not completely, that is partially resting air pockets trapped in the structure beneath the liquid and sitting on the apex of the surface topography without piercing it (Figure 2.3c). The air pockets limit the liquid-solid contact area and dramatically raise the surface's contact angle. Cassie and Baxter [61] devised the following model to determine the apparent contact angle ( $\theta_c^*$ ) in 1944 (Figure 2.3c) [61].

$$\cos \theta_c^* = f_s * \cos \theta_y + f_s - 1 \tag{2.3}$$

$f_s$  = fraction of solid surface

$1 - f_s$  = fraction of Air

It may be established that surface roughness and morphology significantly impact surface wettability. The Kao diagram (Figure 2.3d) depicts the link between the Young contact angle (representing surface tension) and the apparent contact angle in terms of membrane surface wettability state (Wenzel/Cassie-Baxter) [62]. Surface roughness amplifies the hydrophobicity of hydrophobic surfaces or the hydrophilicity of hydrophilic surfaces, as seen in the Kao diagram.

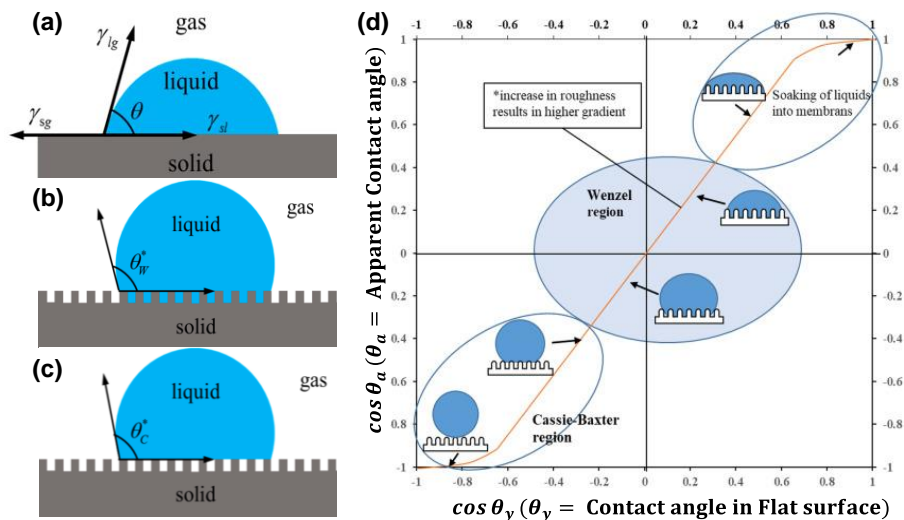


**Figure 2.3** The wetting models of (a) Young’s, (b) Wenzel, and (c) Cassie-Baxter [61]. (d) The Kao diagram [62].

### 2.1.3 Frictional Drag Reduction by Superhydrophobic Surface

There have been several methods introduced to reduce the frictional drag in ship propulsion, including air lubrication, which is a method of reducing drag (frictional resistance) between the ship's hull and seawater by creating a bubbly flow or gas blanket, which has energy-saving effects in terms in ship's fuel consumption depending on various loading, operation conditions, vessel design, and adaptation of the type of air lubrication method for the vessel. Figure 2.4a shows a Mitsubishi air lubrication system [63]. However, to implement such methods still, an energy source is required, often offsetting the reduction in frictional drag.

An alternative solution to this method is utilizing a superhydrophobic surface to entrap an air layer similar to the Cassie-Baxter state mentioned in the previous section to initiate the slip length necessary for effective frictional drag reduction. A visual representation of the frictional drag reduction is presented in Figure 2.4b-c [64]. The authors incorporated Poly(methyl methacrylate (PMMA) powder, nanoscale silica, and tetrahydrofuran (THF, solvent) to prepare a solution that was then sprayed on the model using a spray cannon (jet nozzle diameter = 0.6 mm) at 350 kPa at a distance of 25 cm, which resulted in a boat with the superhydrophobic surface. A reference boat was utilized of the same dimension without any coating. The vessels' engine power supply ranged from 0.3 to 0.75 W, and before coating, the vessels were verified for speed and supplied with the same batteries. The vessels were released and sailed for 20 meters in a water tank, with the average velocity used to determine the drag-reducing impact. As shown in Figure 2.4c, the superhydrophobic model outperformed the bare vessel. The authors observed a silver mirror-like shiny surface underneath the boat, indicating an air layer primarily responsible for the reduced drag. When the superhydrophobic surface was submerged in water, air pockets

formed, isolating water from the substrate. Water would not infiltrate into the asperities due to surface tension.

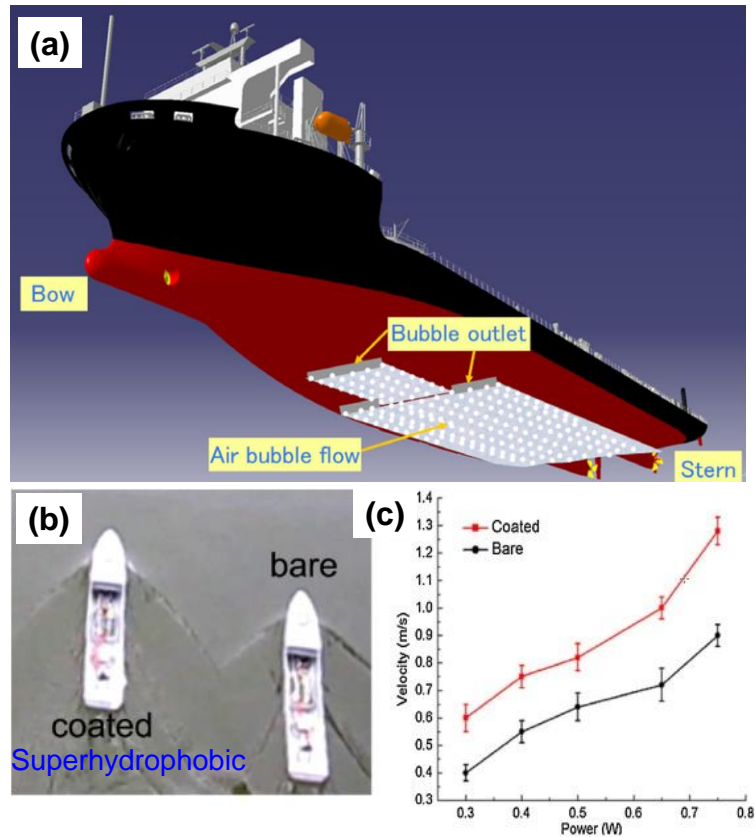


**Figure 2.4** (a) Mitsubishi air lubrication system [63]. (b) The sailing experiment of a boat coated with superhydrophobic coating and a reference boat without any coating [64]. (c) The velocity of the bare/coated model boats with respect to the power supply [64].

Many geometries and flow conditions have been investigated over the years, both numerically and experimentally. Although theoretical studies consistently suggested effective drag-reduction for both laminar and turbulent flows, experimental studies were often contradictory due to consistent measurement techniques and deteriorated plastrons [15]. Wide varieties of geometries were considered to manufacture the SHPo surfaces, including regular

structures such as micro-grates [65–67] and random structures[68–71] (Figure 2.5). Park et al. conducted a thorough comparative review of most available experimental studies data [72]. It was observed that SHPo surfaces with longitudinal micro-trenches structures resulted in drag-reduction most consistently (Figure 2.6). In contrast, random roughness surfaces produced inconsistent results, and in some cases, the drag increased. The arbitrary roughness surfaces have a roughness scale below 10  $\mu\text{m}$  which would lead small slip length ( $<1 \mu\text{m}$ ) inadequate for effective drag reduction. Although in some cases a high value of drag-reduction was reported with random roughness samples, but this could be due to the overgrown plastron size which exceeds the theoretical values calculated based on samples roughness scale.

This is also important to mention that large water contact angles on SHPo surfaces alone are inadequate for effective drag reduction; instead, producing large slip-length and maintaining plastron persistently is the key to successful drag reduction, as discussed in references [17,73]. The micro-trenches structured SHPo surfaces resulting in considerable slip length consistently. For example, Park et al. studied the impact of grating parameters from a pitch of 50 – 100  $\mu\text{m}$  and gas-fraction of 30 – 95% and demonstrated a maximum drag reduction of 75% [16]. Additionally, Xu et al. showed a maximum drag reduction of approximately 30 – 40% in high Reynolds number applications by utilizing micro-trench structures with 50 – 200  $\mu\text{m}$  pitch and 90% gas-fraction [15].

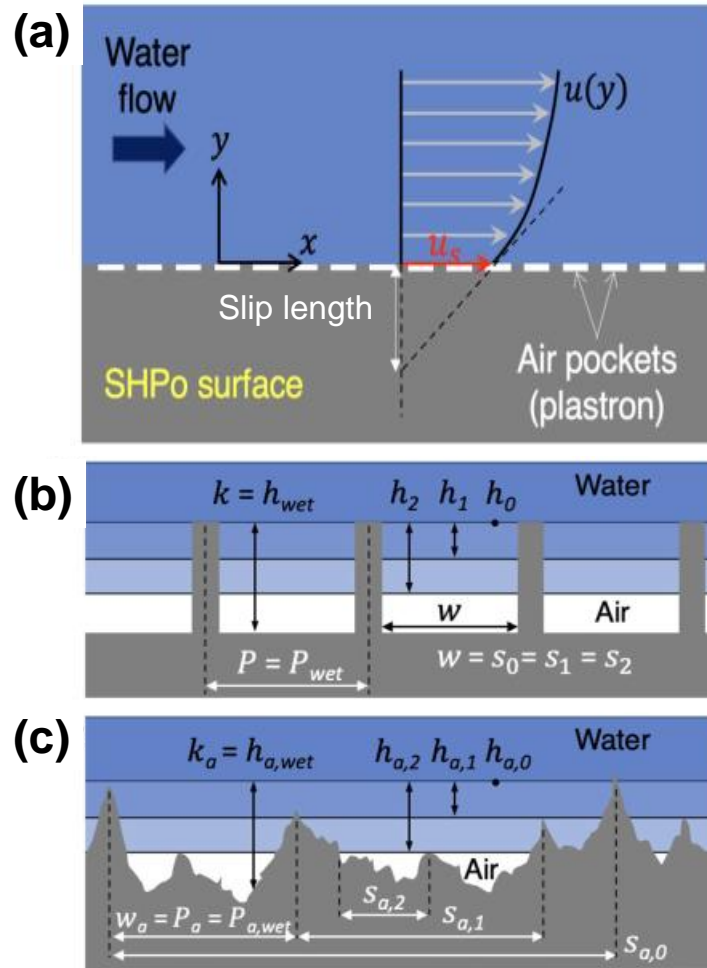


**Figure 2.5** Parameters that affect liquid flow over a SHPo surface are defined as follows: (a) Velocity distribution on a SHPo surface, displaying a slip velocity ( $u_s$ ) and an effective slip length. (b) Water on a vertically structured roughness, exhibiting the air-water interface on or in the roughness parts. (c) Water on a random roughness, defining the average roughness height ( $k_a$ ) and average roughness pitch ( $P_a$ ), which is the same as the average roughness width ( $w_a$ ), along with the average wetted roughness height ( $h_a$ ) and average interface width ( $s_a$ ) with the subscript 0, 1, 2, and wet [74].

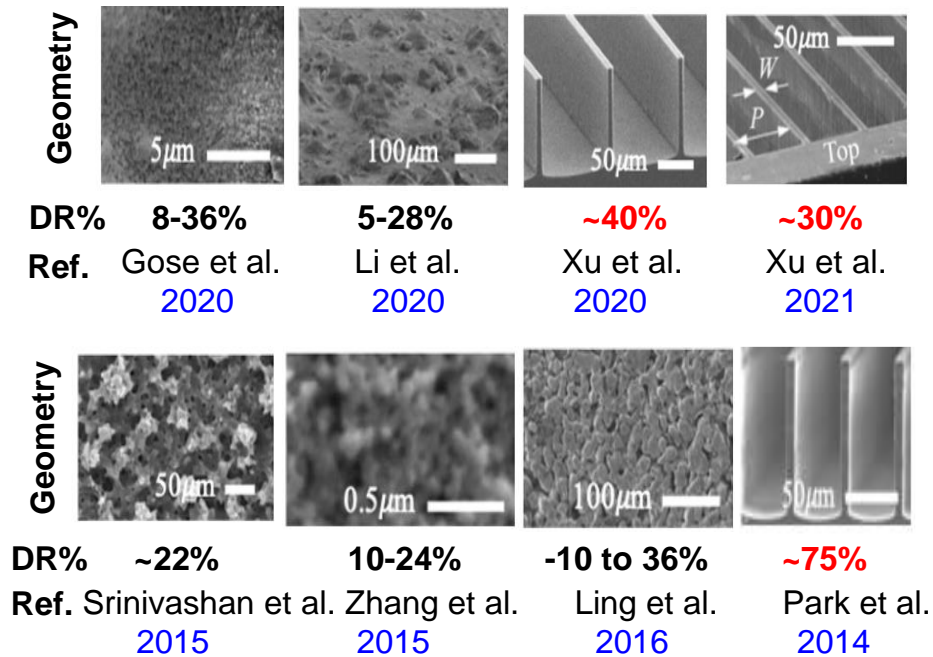


**Figure 2.6** Experimental studies on the SHPo drag reduction in turbulent flows presented with geometry and effective drag-reduction (DR%) [74].

#### 2.1.4 Current Manufacturing Methods

Lithography is one of the standard manufacturing processes for superhydrophobic periodic microstructures[15–17]. Photolithography is a method of putting a design onto a substrate using light. All photolithography processes follow this principle. The photoresist is first applied to the substrate. While putting on the pattern mask, the substrate is subjected to electromagnetic radiation, which alters the molecular structure and causes a change in the solubility of the substance [53]. Etching is done after the exposure. The substrate is then dipped into a developer solution. Aqueous developer solutions dissolve regions of the photoresist exposed to light. However, one primary limitation of this method is that the size of the SHPo surface is limited by the substrate size, which in the case of a silicon substrate, ranges from 10 to 30 cm. This is far smaller than actual boats that are larger in magnitude ranging from several meters to hundreds of

meters. The photolithography process is impractical to manufacture large-area substrates due to high cost and low throughput.

Nanoimprint lithography (NIL) utilizing a Polydimethylsiloxane (PDMS) stamp has been utilized to replicate the hydrophobic micropattern of a lotus leaf [18]. NIL is a simple method for pattern transfer. To transfer the design, a mold (stamp) is first built with surface relief characteristics and then pushed against a polymer substrate. Figure 2.7b shows a schematic of the process. A sacrificial resist film is often used as a mask to etch the underlying substrate or film. Because of its potential for nanoscale manufacturing, NIL has sparked much interest, including superhydrophobic surfaces. Although a high water contact angle can be achieved, the method cannot still be utilized on a large scale.

Other related technologies, such as superhydrophobic-spray coating (Figure 2.7c), micro-coining, bio-pattern imprinting, laser cutting, and 3D printing, also have critical limitations as these methods are time-consuming, expensive, and complex, compromising the scalability [19–23]. Therefore, creating a scalable manufacturing process to produce SHPo micro-grating structures is necessary for practical drag reduction applications.

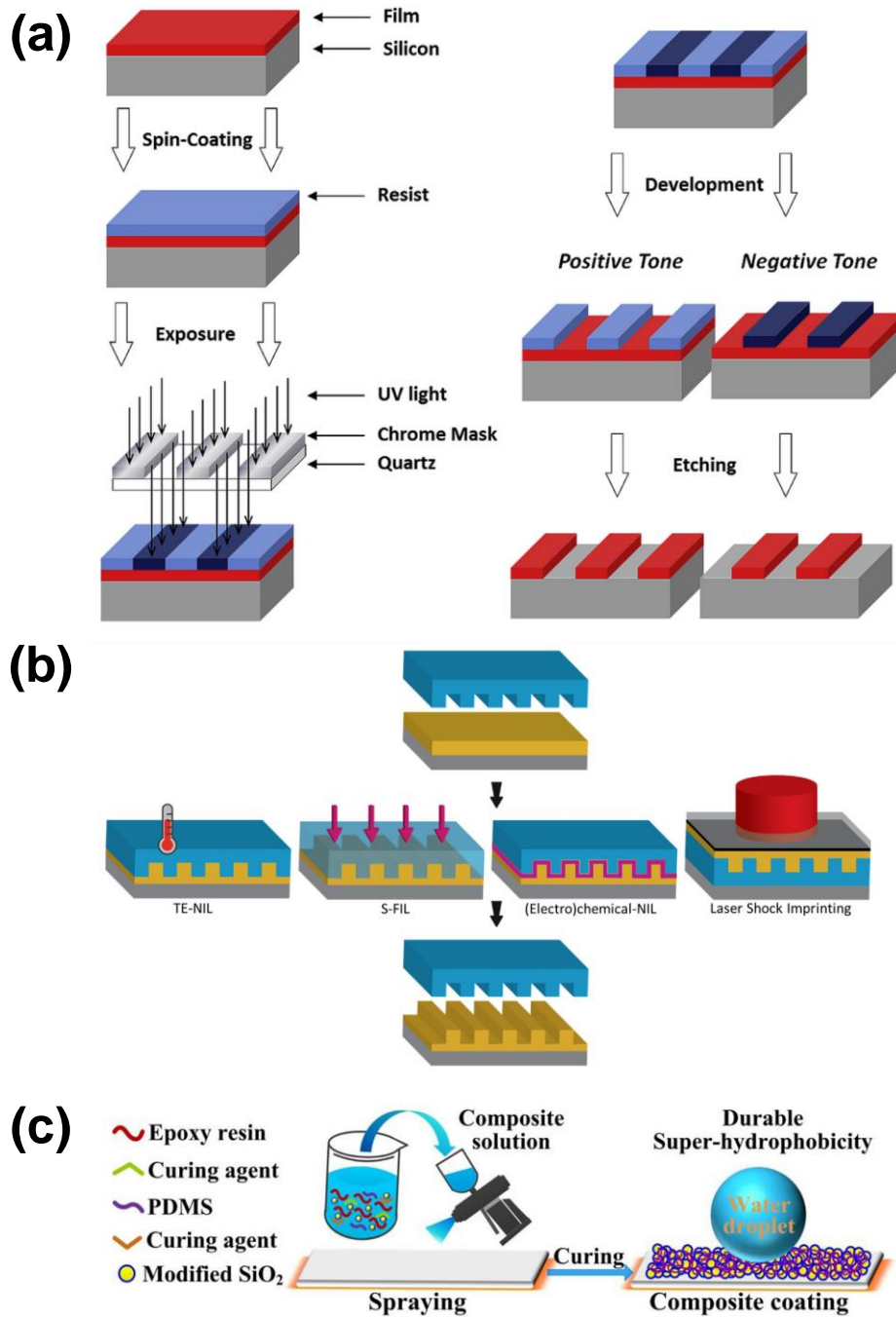


**Figure 2.7** (a) Photolithography process overview [53]. (b) Nanoimprint lithography (NIL) process overview [75]. (c) Schematic illustration of the durable SHPo coating fabricated process

[76].

## 2.2 Ribbing Instabilities

### 2.2.1 Interfacial Forces in Ribbing

The ribbing instabilities were introduced in the introduction of this report. Ribbing is defined as generating spatially periodic patterns in a roll-coating process [24–27]. The patterns are usually observed transverse to the coating direction. During the roll-coating process, a positive pressure gradient is developed in the downstream meniscus of the coating fluid [28]. The flow becomes unstable when the pressure gradient exceeds a critical value, and a finger-like growth is observed [29,30]. Fields et al. discussed several other mechanisms of potential instabilities, as shown in Figure 2.8 [29]. When a tiny layer of liquid is sucked between two glass plates (Figure 2.8a), or the plates are dragged apart (Figure 2.8b), the separation is caused by a crack extending inwards from the plates' sides. The fracture front is smooth and straight if the separation rate is slow and the fluid viscosity is low. However, when the rate (or viscosity) rises, the crack front breaks down into a finger-like structure, with the fingers racing ahead of the main separation front. The smooth, straight lines become more prominent at these greater speeds. The same phenomenon occurs when a viscous-adhesive connection fails in tension, like when an adhesive strip like the Scotch tape is pulled off a smooth surface (Figure 2.8d). The fracture or separation-front is smooth and stable at low peeling speeds: any changes in form are dampened by the adhesive's surface tension; nevertheless, at greater peeling velocities, the front becomes finger-like.

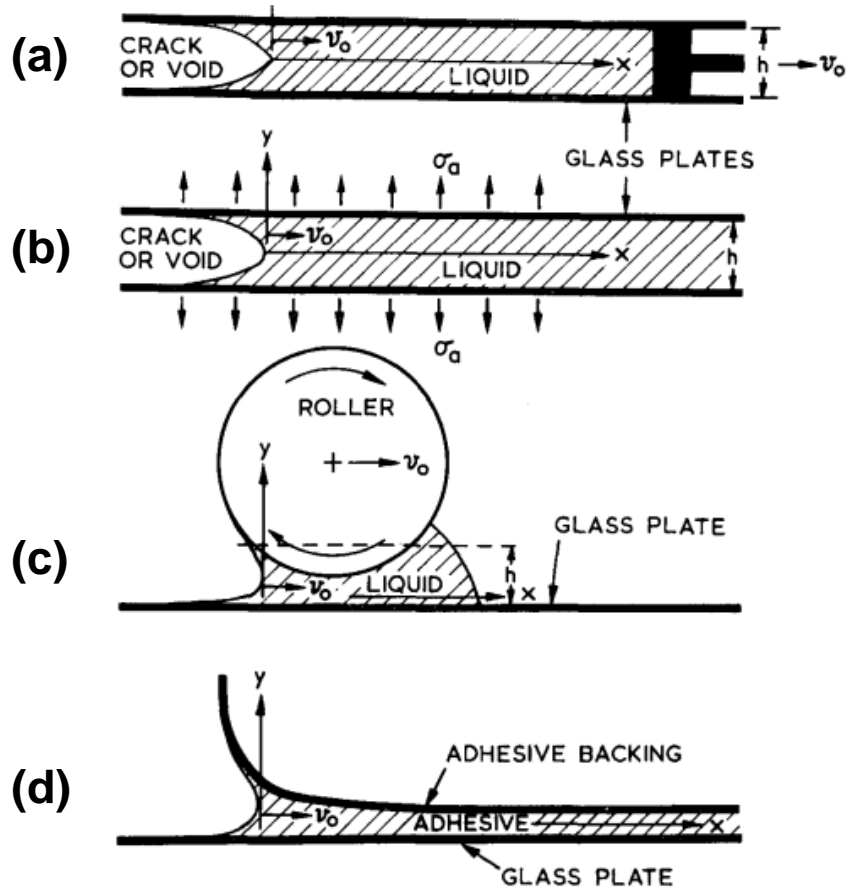


**Figure 2.8** The unstable growth of voids or cracks can be studied by (a) pulling fluid from between glass plates, (b) pulling or wedging the plates apart, (c) moving a roller over a glass plate, and (d) peeling adhesive tapes from glass plates [29].

The driving forces involved in the ribbing phenomenon are explained in Figure 2.9 [29,77].

The flow velocity can be estimated as,

$$v_0 = -\left(\frac{d^2}{12\eta}\right)\left(\frac{dp}{dx}\right)_0 \quad (2.4)$$

where  $d$  is the film thickness or distance between the plates, the fluid's viscosity is  $\eta$ , and  $dp/dx$  is the pressure gradient in the flow direction. Now the pressure potential is estimated as  $a\left(\frac{dp}{dx}\right)$ ,

where  $a$  is the amplitude of the perturbation (Figure 2.9a). Now, if the radius of the curvature is

$R$  and the surface tension of the liquid  $\gamma$ , the restraining force or the stabilizing force will be  $\frac{\gamma}{R}$ .

The following conditions have to be fulfilled to initiate the instabilities,

$$-a \left( \frac{dp}{dx} \right) > \frac{\gamma}{R} \quad (2.5)$$

Next, the maximum restraining force is calculated. Assuming the crack front is assumed to into sinusoidal shape, the fluid front is defined as follows,

$$x = a * \sin \left( \frac{2\pi z}{\lambda} \right) \quad (2.6)$$

The maximum radius of curvature would be as follows.

$$\frac{1}{R} = \frac{d^2 x}{dz^2} = \frac{4\pi^2 a}{\lambda^2} \quad (2.7)$$

If a finger has to grow, the following condition has to be fulfilled,

$$\left( \frac{dp}{dx} \right)_0 > \frac{-4\pi^2 \gamma}{\lambda^2} \quad (2.8)$$

Now replacing the values with equation 2.4 gives the following wavelength conditions for instabilities,

$$\lambda > \pi \left( \frac{d^2 \gamma}{3\eta v_o} \right)^{\frac{1}{2}} \quad (2.9)$$

The form of the perturbation is extremely near to a sine wave when the amplitude is modest; hence the analysis described above is assumed to be correct based on Fields et al. However, when the perturbation evolves into fingers, however, the flow fields or diffusion fields are drastically altered: instead of being virtually parallel to the  $x$ -axis, the velocity or flux vectors now radiate out from the tips of the fingers (Figure 2.9b). Without more evidence, the spacing of these well-developed fingers is not equal to the wavelength of the fastest-growing disturbance, initiating both tip-splitting and tip-coalition. Grillet et al. observed that liquids' elasticity increases the tip-splitting phenomena in ribbing instabilities [78].

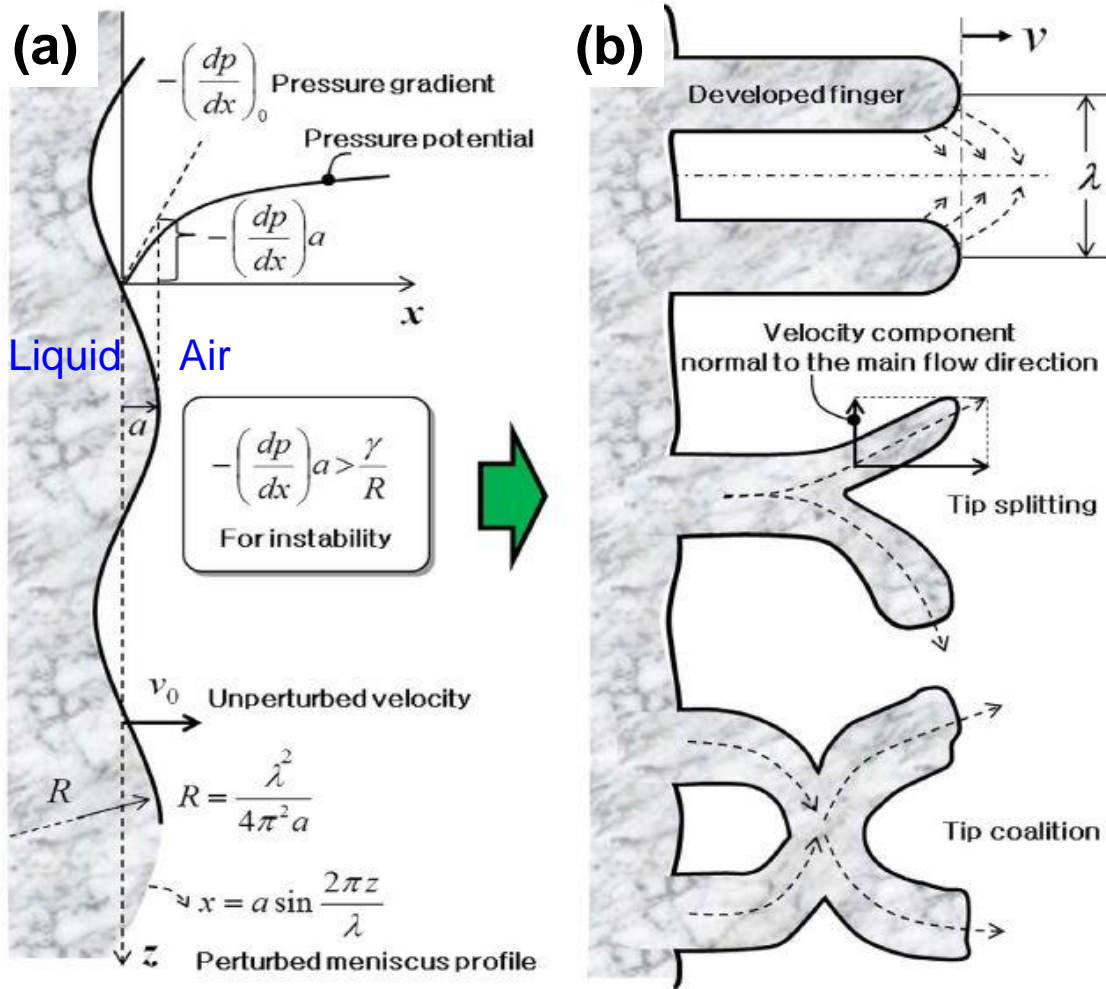


**Figure 2.9** (a) Schematic diagram showing the relationship between the pressure gradient at the advancing front and surface energy. (b) Schematic of the velocity and pressure gradient component radiating outward in the  $z$ -direction, tip splitting, and tip coalescence [77].

### 2.2.2 Ribbing of Newtonian vs. Non-Newtonian Materials

Experimental and computational models have been used to investigate Newtonian and non-Newtonian fluids' ribbing behavior to reduce roll-coating flaws [24–27,37]. Ribbing periodicity or wavelength ( $\lambda_{Ribbing}$ ) and amplitude have been discovered to have a strong link with material qualities and process factors such as surface energy  $\gamma$ , viscosity  $\eta$ , roller radius  $R$ ,

roller gap  $d$ , and roller speed  $U$  [29,38–40]. The beginning condition of the ribbing instability in a Newtonian fluid was discovered to be described by two dimensionless parameters: the capillary number  $Ca = \eta * U/\gamma$  and the geometric factor  $R/d$ . For Newtonian fluids, the critical capillary number  $Ca^*$  exhibited a linear relationship with the geometric factor  $R/d$  [25,27,30,41–43].

Non-Newtonian fluids, on the other hand, have a significantly lower critical capillary number than Newtonian fluids [42]. The theoretical prediction of the  $Ca^*$  in the viscoelastic fluid, unlike the Newtonian fluid, is not possible. There is still a mystery about how ribbing happens in coating treatments. The concentration of polymer molecules regulated the elasticity of a Newtonian fluid (Glycerol/Water), and similar trends in the  $Ca^*$ , and normal stress parallel to the flow were seen as the polymer concentration increased [42]. The findings suggest that the viscoelastic fluid's behavior produces ribbing instability at reduced roller speeds, implying that the viscoelastic fluid's behavior raises stress in the flow direction by limiting flow. According to Zevallos et al., there is a threshold Weissenberg number  $Wi$  over which the flow becomes unstable at any given  $Ca$  [28]. Most non-Newtonian fluids research has been determining the critical capillary number values or threshold conditions that cause instability. However, beyond the beginning circumstances, fluid propagation and ribbing creation have yet to be investigated [44–46].

Grillet et al. explored the effect of elasticity on the stability of air-fluid interfaces during fluid displacement flow for both a viscous Newtonian fluid and an ideal elastic fluid [78]. The stability of coating flows was investigated on an eccentric cylinder shape (Figure 2.10a). Three types of phenomena are described when it comes to Boger fluids. The authors discovered some novel characteristics in classic fingering instabilities in elastic displacement flows. One of them is a very significant elastic instability of forward roll coating, which may be directly linked to the

elasticity of the coating fluid and seems to exist even in the absence of diverging channel walls. As demonstrated in Figure 2.10b, the critical capillary numbers ( $Ca^*$ ) are lower for elastic fluids. In addition, the Newtonian fluid mostly shows a linearly spaced ribbing (Figure 2.10c), whereas when the materials have elasticity shows dramatic tree-branch-shaped ribbing (Figure 2.10d).

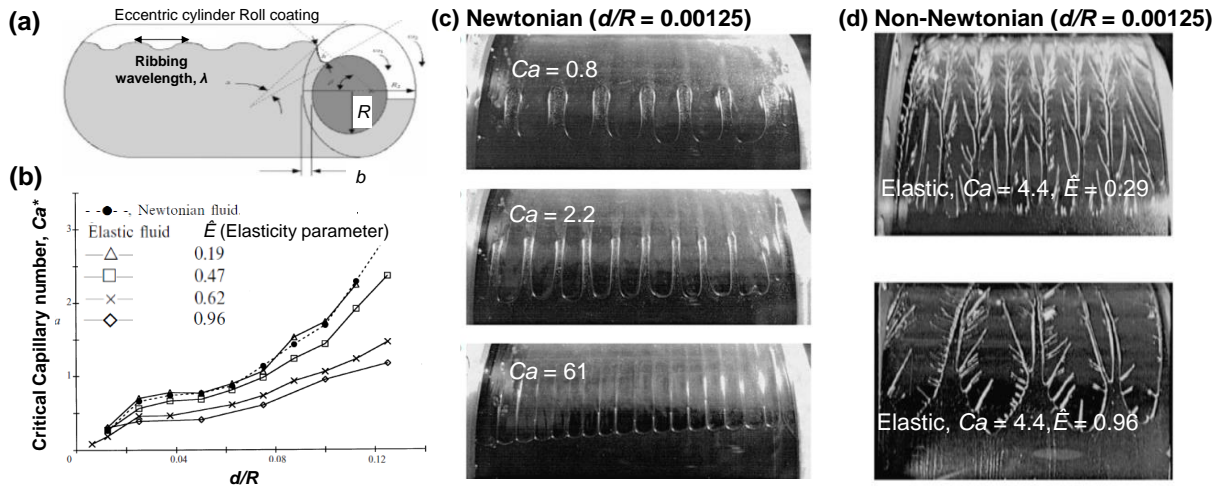


**Figure 2.10** (a) Eccentric cylinder coating apparatus. (b) Comparison of the critical capillary number ( $Ca^*$ ) in the forward roll coating geometry versus the dimensionless gap ratio ( $d/R$ ) from the experimental measurements for a range of fluids with varying elasticity. (c) Eccentric cylinder forward roll coating instabilities for Newtonian fluids (d) Roll coating instabilities in non-Newtonian fluids [78].

## CHAPTER 3 : Coating Paste Formulation

### 3.1 Background

The coating paste was formulated using different nanoparticle inclusion with aspect ratios and volume fractions to tune the viscoelastic properties of the materials. The surface energy of the materials was also determined, which is necessary to understand the surface tension-driven flattening when the rollers come to a stop.

### 3.2 Experimental Methods

#### 3.2.1 Coating Paste Formulation

A nanocomposite paste was synthesized using a polydimethylsiloxane elastomer kit. PDMS Sylgard 184 (S184) and PDMS Sylgard 186 (S186) from Dow chemicals were utilized as the base materials. The multi-walled carbon nanotube (CNT, 6-9 nm diameter and 100-200  $\mu\text{m}$  length) and spherical silicon oxide nanoparticles ( $\text{SiO}_2$ , ~50 nm diameter) were introduced as the inclusion of various vol%. The PDMS and nanoparticles were initially mixed utilizing a universal planetary mixer for 10 minutes (Figure 3.1). Next, the hardener was introduced to the PDMS with a 10:1 ratio. This mixture was then mixed further in a high-shear three-roll milling machine. The roller distances were gradually reduced, and the materials were passed through multiple times to ensure adequate dispersion and homogenization of the nanoparticles. The vol% of the inclusions varied to achieve composite pastes with tailored rheological properties.

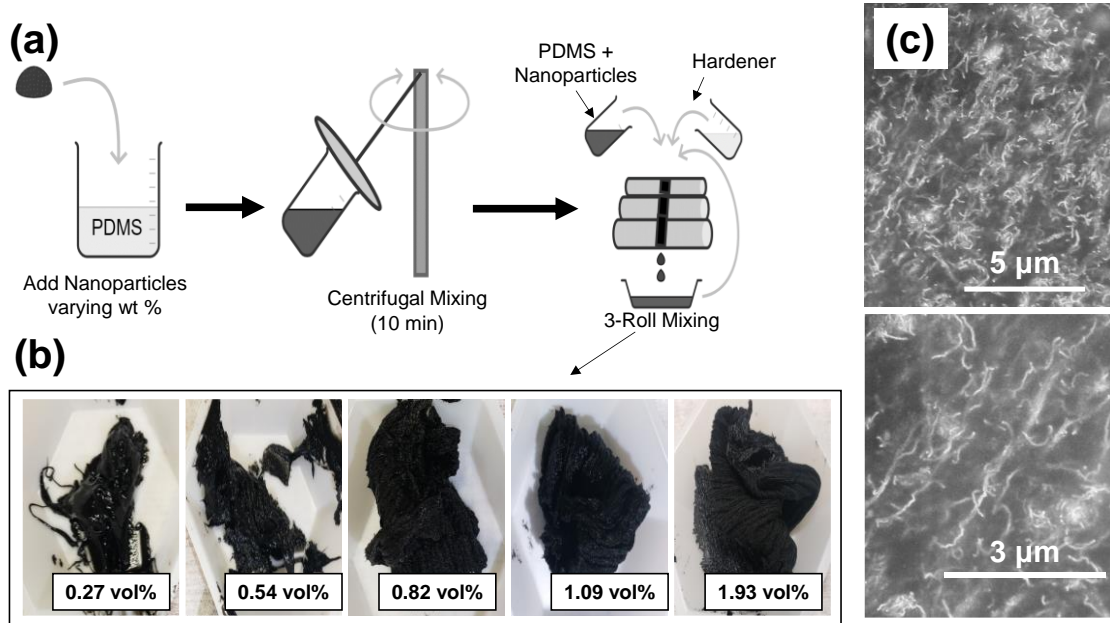


**Figure 3.1** (a) Coating paste formulation (b) Processed CNT-PDMS with varying vol% (c) CNT distribution in PDMS.

### 3.2.2 Surface Energy Measurement

Several surface energy theories have been developed based on the contact angle and  $\theta$  measurements. Fowke's model [79] and the Owens-Wendt model [80,81] were utilized in this study. Fowke's model combines the Young and Young-Dupree equations and separates liquid and solid surface energy as polar and non-polar components as equation (3.1).

$$\frac{\gamma_l(\cos\theta+1)}{2} = (\gamma_l^d)^{1/2}(\gamma_s^d)^{1/2} + (\gamma_l^p)^{1/2}(\gamma_s^p)^{1/2} \quad (3.1)$$

Here  $\gamma_l^d$  and  $\gamma_l^p$  are liquid non-polar(dispersive) and polar components, respectively.

Whereas  $\gamma_s^d$  and  $\gamma_s^p$  are the solid non-polar and polar components. The Owens-Wendt model, also known as the extended Fowke's model, incorporates the Good's equation, thus resulting in equation (3.2).

$$\frac{\gamma_l(\cos\theta+1)}{2(\gamma_l^d)^{1/2}} = (\gamma_s^d)^{1/2} + \frac{(\gamma_l^p)^{1/2}(\gamma_s^p)^{1/2}}{(\gamma_l^d)^{1/2}} \quad (3.2)$$

Three reference liquids with known surface energy values, as mentioned in Table 1.1 (e.g., water, diiodomethane (99%), and ethylene glycol (99%)), were utilized to measure the contact angle on a flat-surfaced test sample. The results were fitted into equations (3.1) and (3.2) to evaluate the surface energy of the test material by Fowke's model and Owens-Wendt's model. The test samples were prepared by a compression molding method, as shown in Figure 6.3 The CNT-PDMS-hardener compositions were mixed well in the Thinky-mixer and the three-roll-mill. The resulted composition was placed between two polyimide sheets and compression-molded under 1-ton pressure with a 0.5 mm spacer. The polyimide sheet with the CNT-PDMS composite was next heat-cured at 120°C for 20 minutes. The polyimide sheet was quickly removed as the polymer crosslinked, resulting in a flat circular-shaped composite sample with uniform thickness. The surface roughness of these test samples was measured using a laser confocal microscope that accounts for surface roughness in the surface energy measurement calculation.

**Table 1.1** Polar and dispersive surface energy components of the test liquids [82]

Test liquid	$\gamma_l$ (mJ/m <sup>2</sup> )	$\gamma_l^p$ (mJ/m <sup>2</sup> )	$\gamma_l^d$ (mJ/m <sup>2</sup> )
water (W)	72.8	51.0	21.8
diiodomethane (DIM)	50.8	0.0	50.8
ethylene glycol (EG)	48.0	19.0	29.0

### 3.2.3 Rheology

Dynamic oscillatory rheological experiments were conducted on a Discovery Hybrid-3 rheometer (TA Instruments) and performed in triplicate. Creep experiments were also conducted

to confirm yield stress values. All experiments were performed using an 8 mm cross-hatched parallel plate geometry kept at 25°C using a Peltier plate. Since the samples were high modulus pastes, the samples were loaded in excess via spatula or by a gloved hand. The rheometer head was brought down to an 1100  $\mu\text{m}$  trim gap, then brought to 1000  $\mu\text{m}$  after trimming. Since the sample would eject in a shear deformation, no pre-shearing was performed, and the test was performed right away, as viscometric parameters did not change with time after loading.

The samples' linear viscoelastic region (LVE) and yield stress were determined using a strain sweep at 1 rad/s. Frequency sweeps were performed from 0.1 – 100 rad/s at an oscillatory strain of 0.1% in the LVE region. The yield stress was determined by evaluating the maximum of elastic stress, which is a product of elastic modulus and strain, with respect to strain. The stress associated with strain is yield stress, according to Walls et al. [83]. A creep test was performed on a 10% w/w sample to confirm the yield stress measurements.

### **3.3 Results and Discussion**

#### **3.3.1 Surface Energy of the Materials**

As discussed prior, the dynamics between surface energy and viscosity of the fluid, often described as a capillary number in roll coating, have a crucial role in ribbing instability. The surface energy ( $\gamma$ ) of PDMS has been well-studied [84,85]. The dispersive component of surface energy was measured at 17.5 – 21.7  $\text{mJ m}^{-2}$  by several methods such as pendant drop, polymer melt, and liquid contact angle measurements approach [84,85]. The polar component was negligible compared to the dispersive component, as the value ranged from 0.8 – 2.3  $\text{mJ m}^{-2}$ . The surface energy of multi-wall CNTs was also measured by the Washburn, Wilhelmy, and SEM contact angle measurements [86–89]. The dispersive component of the surface energy of CNTs of 90 – 99% purity was 23 – 37  $\text{mJ m}^{-2}$ , whereas the polar part was 0 – 16.1  $\text{mJ m}^{-2}$  [86–89].

Despite the availability of references with PDMS and CNTs surface energy data, the CNT-PDMS composite has not been studied previously. In this study, three reference liquids, water, diiodomethane (DIM), and ethylene glycol (EG), are used to measure contact angles in several flat samples of the composite materials. The data were fitted in Owens-Wendt model equation 3.1 and equation 3.2, and the apparent surface energy was evaluated (Table 1.2 and Figure 3.2). The addition of CNTs showed minimal impact on the surface energy of the PDMS. The polar component ( $\gamma_t^p$ ) for each test material was low, 0.07 – 0.17 mJ m<sup>-2</sup>, and the dispersive component ( $\gamma_t^d$ ) was dominant in all cases. The total surface energy ( $\gamma_t$ ) for PDMS (S184), 1.79 vol% CNT, and 6.13 vol% CNT, was found 23.23, 21.85, and 23.2 mJ m<sup>-2</sup>, respectively, based on the Owens-Wendt model. The surface energy of the PDMS was found to be in good agreement with the prior studies validating the experimental method [84,85]. The results provide further understanding for the next phase of this study. As the surface energy of the composite appears to be dominated by the PDMS, the only scope to tune to dynamics between viscous force and surface energy would rely on tuning the viscoelastic properties as observed in the prior section. The surface energy of S186 with nanoparticles showed slightly lower total surface energy (17.9-18.2 mJ/m<sup>2</sup>) as observed in Figure 3.2b.

**Table 1.2** Surface energy measurement based on the Owens-Wendt model

Material	Test liquid	Contact angle, $\theta$	$\frac{\gamma_l^p}{\gamma_l^d}$	$\frac{\gamma_l(\cos\theta + 1)}{2(\gamma_l^d)^{1/2}}$	$\gamma_t^d$ (mJ/m <sup>2</sup> )	$\gamma_t^p$ (mJ/m <sup>2</sup> )	$\gamma_t = \gamma_t^p + \gamma_t^d$ (mJ/m <sup>2</sup> )
PDMS (S184)	DIM	67.48	0.00	4.93			
	EG	93.28	0.81	4.20	23.06	0.17	23.23
	Water	116.52	1.53	4.32			
1.65 vol% CNT – S184	DIM	69.04	0.00	4.84			
	EG	94.75	0.81	4.09	21.78	0.07	21.85
	Water	115.40	1.53	4.45			
5.68 vol% CNT – S186	DIM	66.65	0.00	4.98			
	EG	93.33	0.81	4.2	23.12	0.1	23.22
	Water	114.87	1.53	4.52			
PDMS (S186)	DIM	78.2	0.00	4.29			
	EG	84.1	0.81	4.91	18.49	0.35	18.83
	Water	109.4	1.53	5.21			
0.88 vol% CNT – S186	DIM	79.35	0.00	4.22			
	EG	85.08	0.81	4.84	17.1	1.19	18.29
	Water	104.00	1.53	5.91			
6.92 vol% SiO <sub>2</sub> – S186	DIM	73.4	0.00	4.58			
	EG	97.68	0.81	3.86	17.47	0.44	17.91
	Water	106.03	1.53	5.64			

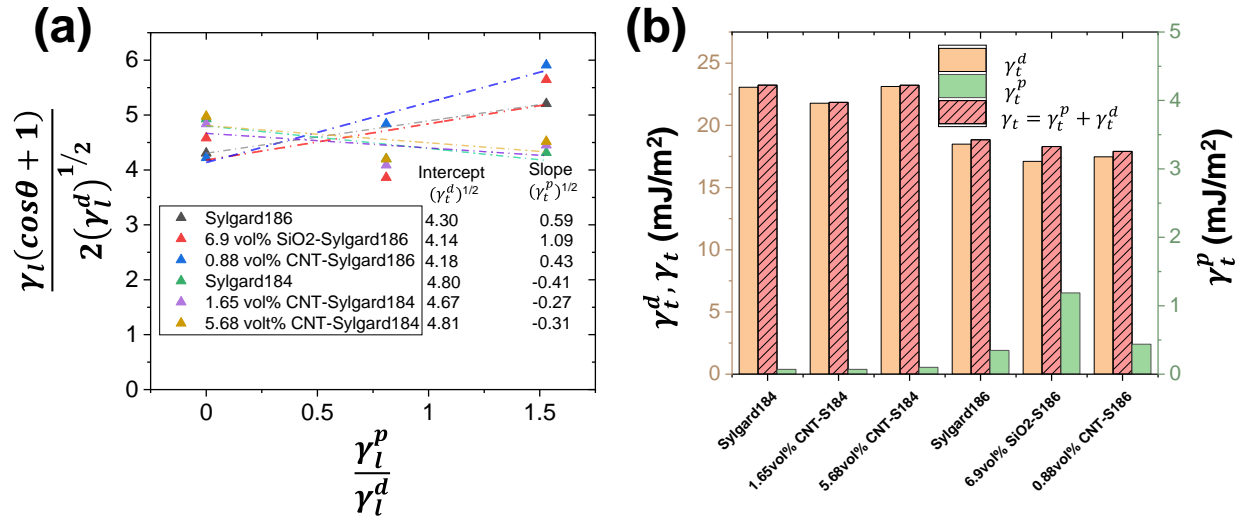


**Figure 3.2** (a) The test materials are analyzed for contact angle for various reference liquids, and the result in data are fitted in the Owens-Wendt model. (b) The surface energy components of the materials are based on the fitting.

### 3.3.2 Rheological Properties

The viscoelastic properties of the coating pastes are investigated first, which were later utilized in CFD analysis and helped determine the desirable properties of the coating paste. Figure 3.3a shows the storage modulus and oscillation stress concerning the strain %. The horizontal part of the storage modulus is associated with the LVE. Materials with lower elastic modulus and longer LVE are more fluid in nature, whereas the shorter LVE and higher elastic modulus mean more solid-like behavior. For example, S186 showed LVE of 2% oscillation strain, whereas S186-0.33 vol% CNT and S186-0.88 vol% CNT showed LVE of 0.8% and 0.3% oscillation strain. The LVE region's storage modulus for the materials were  $9.44 \times 10^{-4}$ ,  $4.9 \times 10^{-3}$ , and  $1.3 \times 10^{-1}$  Pa consecutively, meaning S186 is the most fluidic and S186-0.88vol%CNT the most solid-like materials. The materials' oscillation stress increased linearly until the LVE region for all the materials.

Figure 3.3b is next obtained by running a frequency sweep in the LVE region (0.03% strain) to obtain storage modulus and loss modulus concerning the angular frequency. Here we observe that the S184 shows a storage modulus of  $1.83 \times 10^{-9} - 7.99 \times 10^{-4}$  Pa, whereas the loss modulus is  $5.31 \times 10^{-7} - 2.61 \times 10^{-3}$  Pa. As the loss modulus was observed to be higher than the storage modulus, the S184 behaves like a liquid. In contrast, all CNT inclusion materials showed higher storage modulus than loss modulus. The domination of storage modulus means the CNT-PDMS composites are more elastic in nature and behave as a solid compared to S184. The elastic ( $G'$ ) and viscous modulus ( $G''$ ) also reveal a frequency-dependent behavior with  $G''$  dominating  $G'$  indicative of viscoelastic material. When carbon nanotubes (CNTs) are incorporated into the PDMS, the elastic and viscous moduli increase by several orders of magnitude (Figure 3.3b). The elastic modulus becomes larger than the viscous modulus, and both are independent of frequency, characteristic of three-dimensional sample spanning networks [91,92]. Such microstructure formation via physical interlocking between the CNTs and PDMS has been suggested before, suppressing the molecular motions of the polymer chains [93,94].

Figure 3.3c shows the complex viscosity vs. angular frequency data where the CNT loaded samples exhibit a power-law behavior concerning frequency. The absence of a Newtonian regime is consistent with microstructure formation [95]. All samples show a significantly enhanced value compared to PDMS-alone; more importantly, we observe a slope approximating -1, suggestive of the presence of yield stress. Huang et al. measured similar trends in this type of system, with high modulus and yield stress values attributed to nanotube clusters which jam and cause internal percolation within the polymer matrix [96].

Next, the yield stress is confirmed and measured by plotting the elastic stress vs. the strain % data (Figure 3.4a), whereas the peak of the elastic stress provides the yield stress value. We

have used the elastic stress approach to measure the yield stress in this plot [92,97]. The yield stress prevents the paste from flowing until specific stress is met, beneficial as surface features can be preserved post-processing. The yield stress of the materials is plotted in Figure 3.4b. Note that S184 did not show yield stress, whereas with CNT inclusion of 0.54, 0.82, 1.09, 1.37, 1.93, and 5.68 vol% incurred yield stress of 2012, 2414, 3318, 5341, 9431, 68679 Pa. The S186 showed yield stress of 8325 Pa, whereas CNT inclusion of 0.33, 0.88 vol% introduces 22804, 588637 Pa yield stress, and S186-6.92 vol% SiO<sub>2</sub> shows yield stress of 80782 Pa. Overall, the S186 materials showed higher yield stress than S184 materials, and the cylindrical CNTs showed higher yield stress compared to spherical SiO<sub>2</sub> inclusion for a similar vol%. In addition to the moduli increase, the physical interlocking of the nanoparticles in the PDMS matrix results in yield stress, which increases with loading. This was also confirmed in the subsequent experiment that PDMS could not retain the ribbing shape due to lack of yield behavior, whereas CNT-PDMS samples prevent surface-tension-driven flattening.

### **3.4 Conclusion**

The surface energy was observed to have a minimal impact on the inclusion vol% of the particles. The S186 has consistently lower surface energy (17.9-18.2 mJ/m<sup>2</sup>) in comparison to S184 composites surface energy (21.85-23.23 mJ/m<sup>2</sup>). However, the viscosity of the materials significantly changes as we include nanoparticles. The nanoparticle's addition physically interlocks the polymer, resulting in the materials' yielding behavior. The yield stress was observed to be depending on the geometry and volume fraction of the inclusion. The yield stress is necessary for potential shape retention when the rollers come to a stop to retain the ribbing patterns.

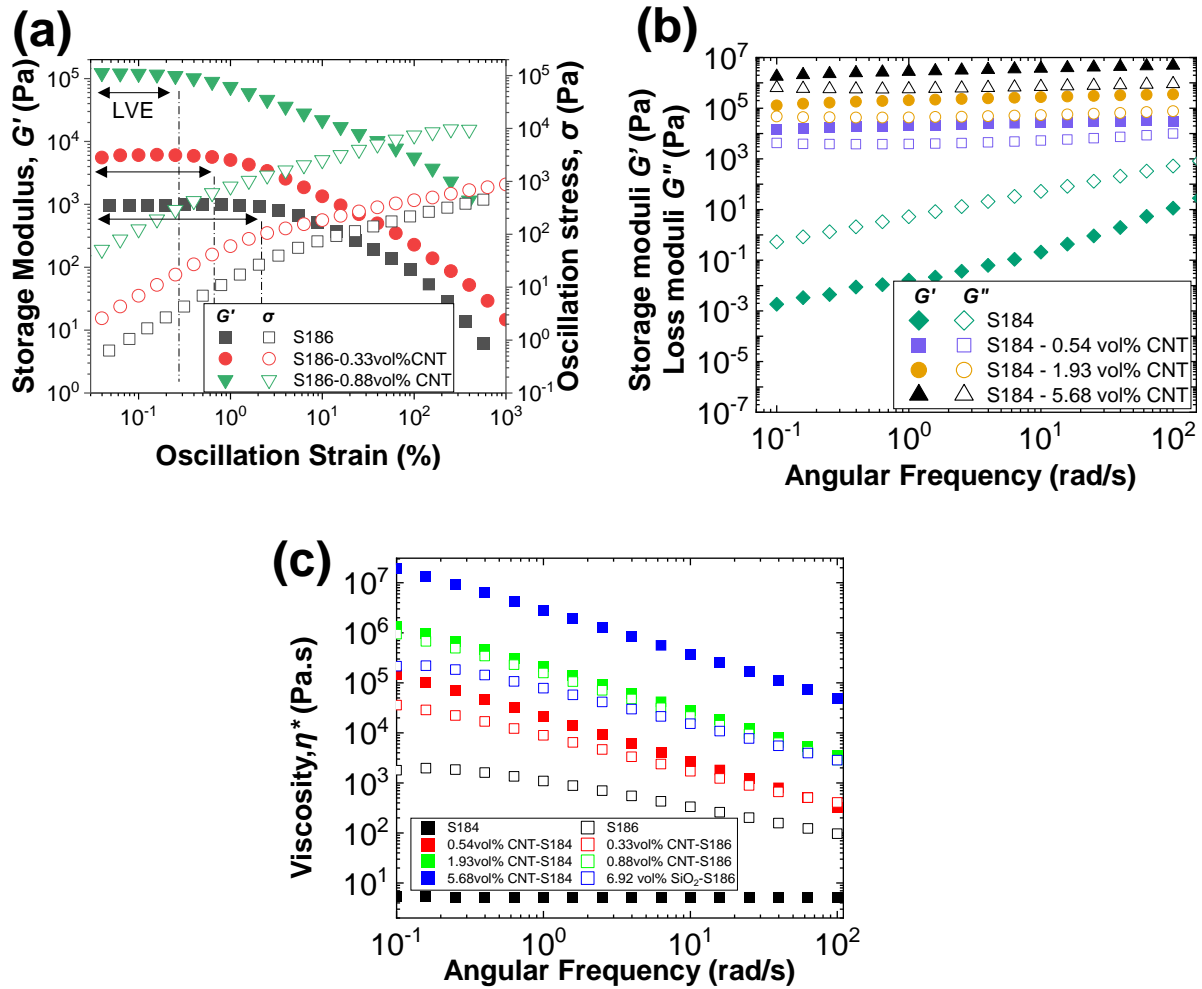


**Figure 3.3** (a) Storage Modulus ( $G'$ ) and oscillation stress vs. oscillation strain (%) to identify the linear viscoelastic region (LVE). (b) Storage Modulus ( $G'$ ), and loss modulus ( $G''$ ) vs. angular frequency (rad/s). (c) Complex Viscosity ( $\eta^*$ ) vs. angular frequency.

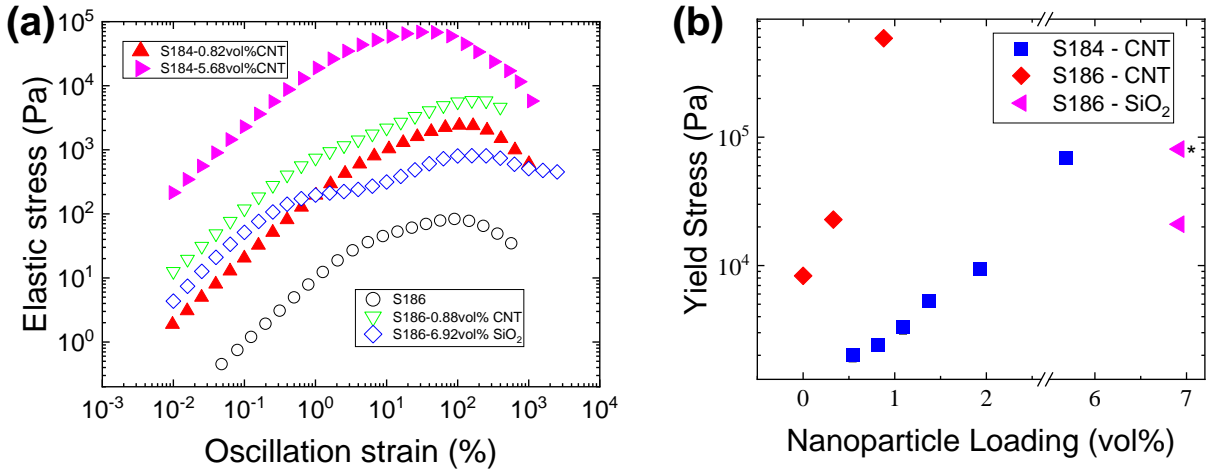


**Figure 3.4** (a) Elastic stress vs oscillation strain (%). (b) Yield stresses ( $\sigma_y$ ) of the composites vs. nanoparticles vol%.

## CHAPTER 4 : Computational Fluid Dynamic Study of Ribbing formation

### 4.1 Background

Most materials utilized for the roll-coating applications are non-Newtonian, as the material's properties depend on the shear rate. However, the roll-coating machines lack the ability to measure the shear rate and other critical properties as the roll-coating happens. Thus, we introduce a CFD model that will assist in predicting the critical process parameters necessary to investigate the material's behavior as the roll-coating occurs.

### 4.2 Experimental Methods

#### 4.2.1 CFD Simulation

Simulations of the roll coating process are performed using the commercial computational fluid dynamics software *FLOW-3D* based on the volume of fluid (VOF) method. The schematic of the simulation configuration with boundary conditions is shown in Figure 4.1. The fluid flow inlet is considered a pressure boundary condition with fluid-fraction of 1, whereas an outflow boundary condition is used at the outlet. All other boundaries are assumed symmetric. The gravity and non-inertial references, surface tension, viscosity, and turbulence physics modules are utilized in the simulation. The PDMS (Sylgard-184) and 1.93 vol% CNT-PDMS are modeled based on the surface energy and viscosity measured experimentally in this research. The unsplit-Lagrangian model was used for the volume of fluid advection scheme, which exhibits good accuracy in tracking sharp interfaces in complex three-dimensional motions. The fluid flow was solved using Navier Stokes momentum and continuity equations. A minimum time step of  $10^{-16}$  sec and a maximum time step of  $10^{-7}$  sec is considered with a 5% volume-fraction cleanup to minimize computation time. *FLOW-3D* POST was utilized to the analyzing the simulation results.

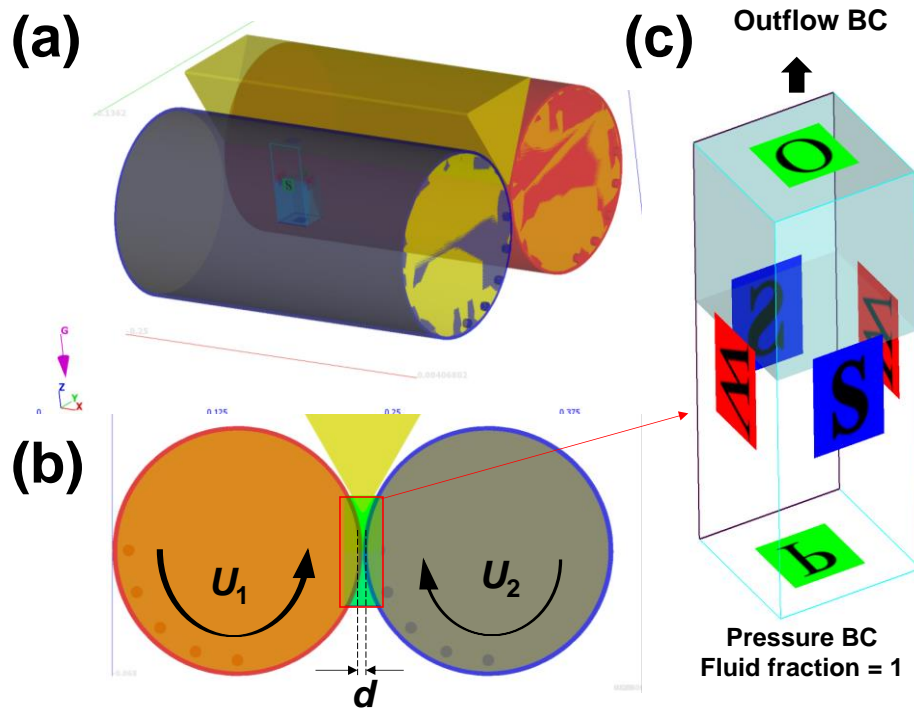


**Figure 4.1** Schematic of the CFD simulation configuration of the two-roll coater in (a) 3D (b) 2D (c) The fluid-flow mesh boundary conditions. Here O, P, and W stand for outflow, pressure, and wall boundary.

### 4.3 Results and Discussion

A fundamental limitation in prior studies related to roll-coating of non-Newtonian materials was defining the process parameters during the roll coating, such as the capillary number  $Ca^*$ , shear rate ( $\dot{\gamma}$ ) and wall shear stress ( $\tau_w$ ) [98,99]. The shear rate-dependent viscoelastic behavior of the coating materials is usually obtained by a rheometer. However, the roll-coating instruments are not intrinsically viscometric, as they do not have the necessary sensors. Thus, the exact viscosity of the coating paste during the roll-coating process is unknown as the associated shear rate is also unknown. Estimating the capillary number relies on either assuming a constant viscosity or estimating the shear rate based on the velocity of the rollers

[77], which results in inaccurate  $Ca$ . Accurate measurement of the shear rate can be obtained by finite element analysis to determine the fluid velocity profile gradient during the roll-coating process [98,99]. In this section, a CFD simulation was conducted to develop an effective method to determine the unknown process parameters, including the pressure gradient in the fluid flow direction ( $dp/dx$ ), fluid flow velocities ( $V_x$ ), shear rate ( $\dot{\gamma}$ ), and wall shear stress ( $\tau_w$ ) related to the roll coating process parameters such as rollers speed ( $U$ ) and rollers distance ( $d$ ). Both rollers were kept at the same speed for each simulation ( $U_1 = U_2$ ). These parameters were later studied along with the experimental results for further understanding.

The ribbing formation was observed in the CFD simulation of roll-coating under various process conditions, as observed in Figure 4.2a. First, a 3D simulation was conducted at a fixed roller speed of  $U = 40 \text{ rad s}^{-1}$  for different roller distances ( $d$ ). A dimensionless parameter ( $R/d$ ) was defined, where  $R$  is the roller radius. The ribbing wavelength ( $\lambda_{Ribbing}$ ) is defined by the distance between each riblet's peak.  $\lambda_{Ribbing}$  is initially observed to be equally spaced for each condition and reduces from 7.9 to 3.3 mm as  $R/d$  increases from 63.5 to 84.67. However, as the  $R/d$  further increases to 101.6, the periodicity becomes irregular as  $\lambda_{Ribbing}$  observed between 1.6 – 2.5 mm. Finally, with an  $R/d$  of 127, the ribbing patterns show further distortion and  $\lambda_{Ribbing}$  increases to 5 mm. An additional phenomenon known as the filamentation phenomenon is also observed in the 3D simulation [100]. Here on each of the riblets, a septum forms, which gets perforated as the rollers move and the fluid is further stretched. The holes get more prominent as the rollers keep rotating, and eventually, the septum breaks leaving micro-peaks on the ribbed patterns [100].

The surface tension-driven 3D model in *FLOW-3D* is highly computationally demanding. As a remedy, further investigation on the pressure gradient, shear rate, and shear stress during the

roll-coating is conducted in two-dimension. The cross-sectional view of the fluid at the roller's interface is shown in Figure 4.3. The pressure gradient ( $dp/dx$ ) and fluid velocity ( $V_x$ ) are observed along the  $x$ -axis ( $a$ - $b$  direction). As the rollers start to rotate, a pressure differential is generated, as observed in Figure 4.4a, with high pressure on the upstream, which drives the fluid flow. The pressure differential increases with an increase in  $R/d$ . The higher-pressure differential also causes a higher  $V_x$  in the  $a$ - $b$  direction. The  $V_x$  is also plotted against  $y/d$  in the  $c$ - $d$  direction (Figure 4.4b), where  $y$  is the coordinates in the  $y$ -direction and  $d$  is the roller distance. The maximum velocity of the PDMS is observed at the center of the fluid flow,  $x/d = 0.5$  (Figure 4.4b). The shear rate was next calculated as the velocity gradient ( $dV_x/dx$ ) and presented in Figure 4.4c. The maximum shear occurs at the roller's wall and the higher  $R/d$  results in the higher shear rate. Next, a parametric study is conducted for roller speed ( $U$ ) of 30, 50, 80, and 100 rpm with  $R/d$  of 31.75, 36.28, 42.33, 50.8, and 63.5. The resulting  $dp/dx$ ,  $\dot{\gamma}$ , and  $\tau_w$  are plotted in Figures 4.4d, 4.4e, and 4.4f. Each of these parameters increases with an increase in roller speed and  $R/d$ . The effect of  $R/d$  was more dramatic at higher roller speed. For example, the  $dp/dx$  increases only from 0.79 to 4.14 MPa m<sup>-1</sup> at 30 rpm but increases from 2.84 to 13.86 MPa m<sup>-1</sup> at 100 rpm. Similarly, at  $R/d$  of 31.75, the  $dp/dx$  increases from 0.79 to 2.84 MPa m<sup>-1</sup> as the roller speed increases from 30 to 100 rpm, respectively, whereas the same increase in speed causes  $dp/dx$  to escalate from 4.13 to 13.86, respectively. In summary, the CFD analysis established a method to determine some key parameters that were not able to examine in prior studies due to the limitation of the experimental tools. The  $dp/dx$ ,  $\dot{\gamma}$ , and  $\tau_w$  observed in the CFD simulation results is utilized to analyze the experimental results in the following sections.

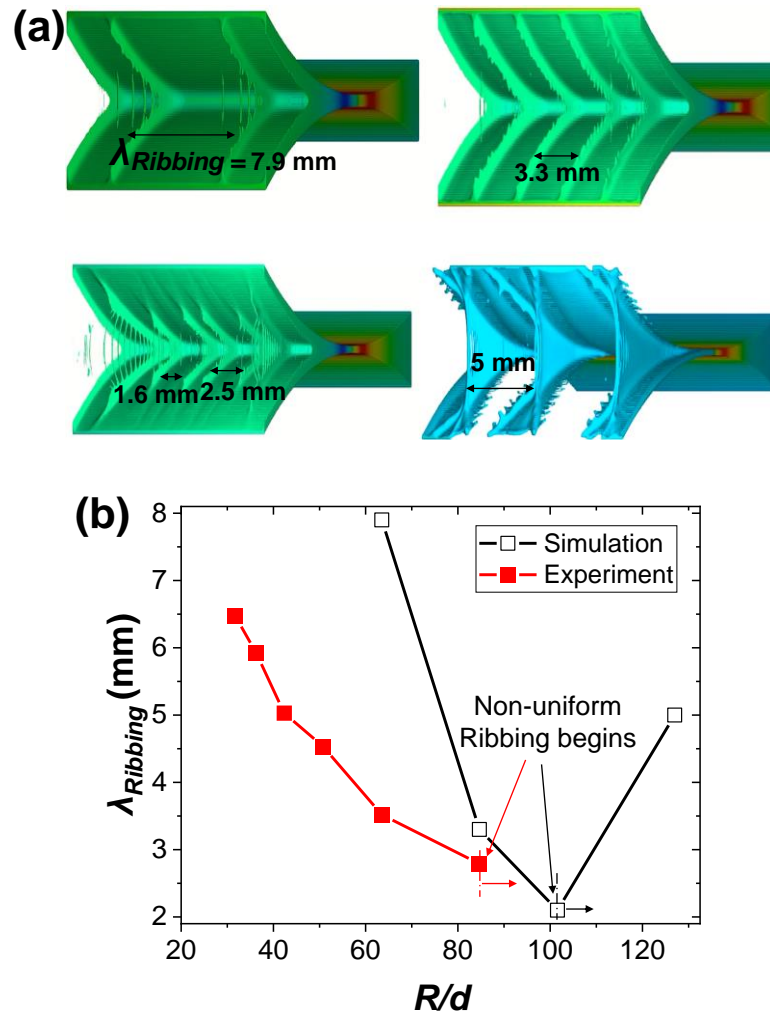


Figure 4.2 (a) Ribbing instabilities in *Flow-3D* (b) CFD results compared with experiments.

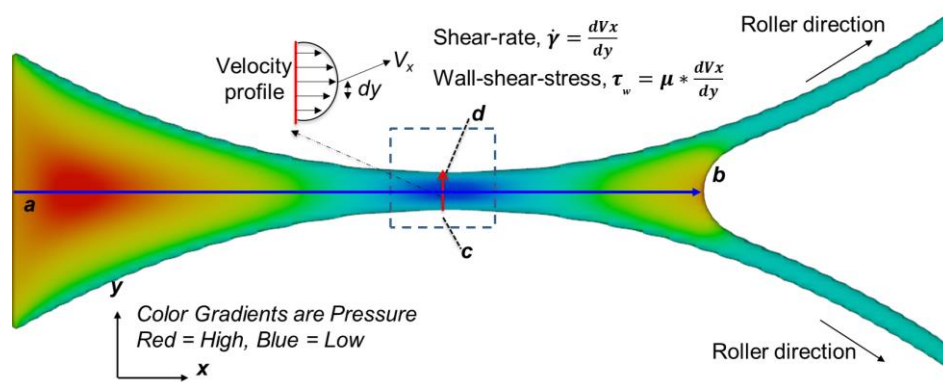
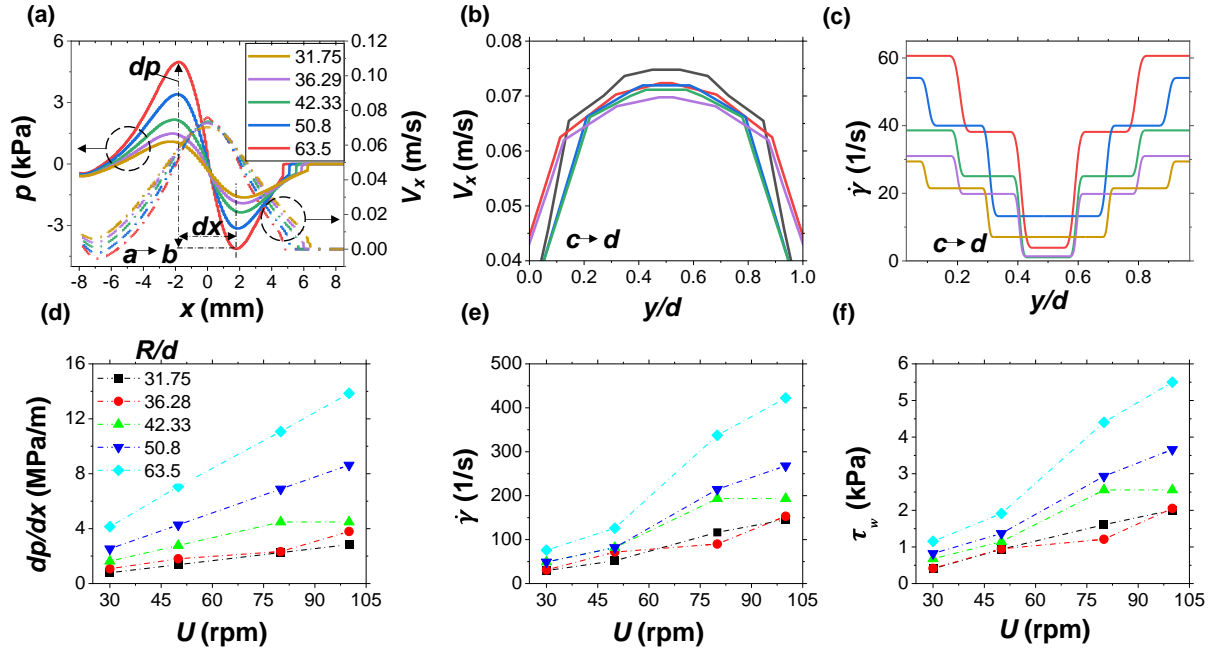


Figure 4.3 Schematic of the fluid cross-section of the CFD model.



**Figure 4.4** (a) Absolute pressure and fluid velocity at the direction of fluid flow ( $x$ - $x$  direction) for  $R/d = 31.75, 36.29, 42.33, 50.8,$  and  $63.5$  at a roller speed of 10 rpm. (b) The fluid velocity profile in the  $x$ - $x$  direction. (c) Shear rate ( $\dot{\gamma}$ ) generated due to the velocity gradient at the  $x$ - $x$  direction. (d-f) Pressure gradient ( $dp/dx$ ) in the flow direction,  $\dot{\gamma}$ , and  $\tau_w$  in various roller speeds (30, 50, 80, and 100 rpm at  $R/d$  of 31.75, 36.29, 42.33, 50.8, and 63.5)

A parametric study was conducted for PDMS as the coating liquid to understand the ribbing behavior related to the process parameters. A distinct ribbing phenomenon is observed upon rotation of the rollers, identical to what was observed in the CFD simulation in Figure 4.2a. Some of the ribbing images are shown in Figure 4.5a-h. The ribbing wavelength ( $\lambda_{Ribbing}$ ) is investigated concerning the rollers speed ( $U$ ) and the dimensionless geometric parameter  $R/d$ . For any given  $R/d$ , an increase in roller speed results in a decrease of  $\lambda_{Ribbing}$  (Figure 4.6a). A more dramatic reduction in wavelength is observed with the rise of  $R/d$  for any specific speed. For example, at  $R/d$  31.75, the wavelength decreases from 7.03 to 6.47 mm with a 30 – 100 rpm

roller speed. At 30 rpm speed, the wavelength reduces from 7.03 mm to 3.52 mm as the  $R/d$  increases from 31.75 to 63.5, respectively. At a higher  $R/d$  ( $> 63.5$ ), the linear ribbing periodicity started to be non-uniform (Figure 4.5h), similar to what was observed in the CFD simulation (Figure 4.2a).

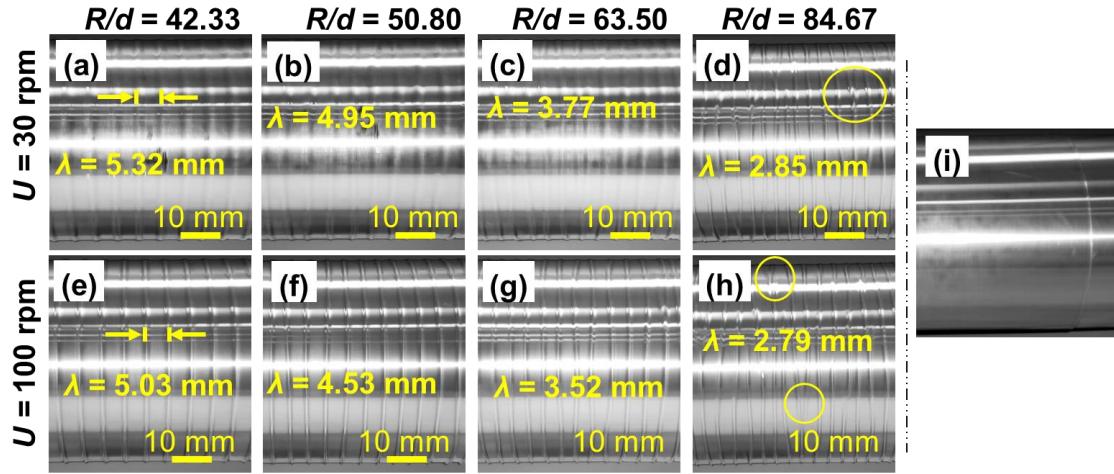


**Figure 4.5** (a-h) Ribbing instability of PDMS under various process conditions. (i) PDMS flattens after a few seconds.

The ribbing pattern of the PDMS is only observed when the rollers are rotating. As soon as the rollers stop, the ribbing patterns flatten in a few seconds due to the surface tension (Figure 4.5i). As observed in Figure 3.3c, the PDMS behaves like a fluid with nearly constant viscosity (about 5.2 Pa.s) from a shear rate of 0.1 to 100  $s^{-1}$ . This fluid-like behavior allows the surface tension force to flatten the ribbing patterns quickly.

Next, the calculated  $dp/dx$ ,  $\dot{\gamma}$ , and  $\tau_w$  from the CFD simulations is plotted against the experimental wavelengths (Figures 4.6b, 4.6c, and 4.6d). As also supported by the earlier studies [28], the  $dp/dx$  was closely related to the ribbing wavelengths. A higher  $dp/dx$  associated with more instabilities resulted in shorter wavelengths. In addition, higher  $\dot{\gamma}$  and  $\tau_w$  also resulted in

shorter ribbing wavelengths. A statistical analysis of the  $\lambda_{Ribbing}$  individually with respect to  $\log_{10}(dp/dx)$ ,  $\log_{10}(\dot{\gamma})$ , and  $\log_{10}(\tau_w)$  shows a co-relation factor of  $-0.836$ ,  $-0.81$ , and  $-0.823$ , respectively, proving a strong relationship between these parameters. In addition, a linear fitting between these parameters also shows  $R$ -square values of  $0.68$ ,  $0.64$ , and  $0.66$  consecutively for the equations shown in Figures 4.6b, 4.6c, and 4.6d. A lack of fitting analysis for the linear fitting results in a  $p$ -value of  $0.056$ ,  $0.243$ , and  $0.25$ . This demonstrates that the fittings are significant with 95% confidence ( $p$ -value $>0.05$ ).

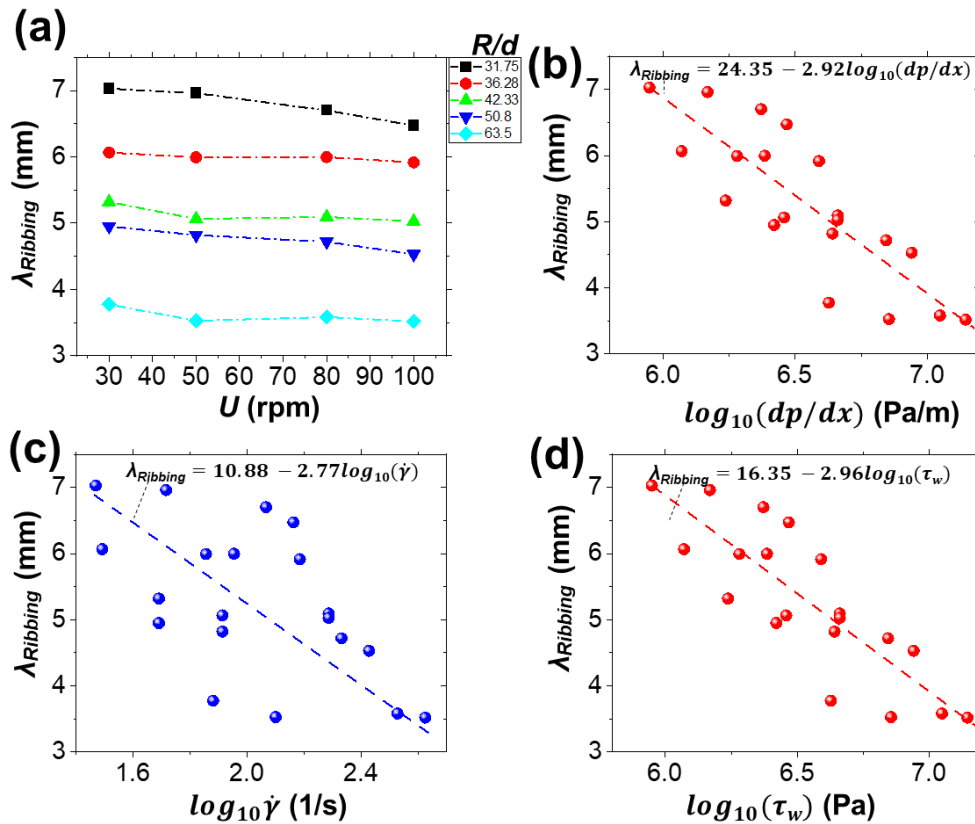


**Figure 4.6** (a) Experimental data of PDMS ribbing wavelengths vs. various process conditions.

(b-d) The experimental wavelengths of PDMS are plotted against  $dp/dx$ ,  $\dot{\gamma}$ , and  $\tau_w$  calculated from the CFD analysis.

#### 4.4 Conclusions

In summary, there were two crucial findings from the roll-coating of the PDMS. The wavelength decreases with an increase in roller speed or  $R/d$ , whereas the reduction is more evident with the rise of  $R/d$ . The  $dp/dx$  primarily drives the wavelength formation. The PDMS cannot retain the ribbing patterns when the rollers stop as the materials behave as a fluid. This draws interest in synthesizing coating materials that will behave as a solid when at rest, preventing surface tension-driven flattening; but acting as fluid during the roll-coating allowing the ribbing formation to occur. *Flow-3D* simulations showed the controllable ribbing phenomenon. The experimental results validated the simulation. PDMS (Sylgard 184) shows ribbing formation but cannot retain the shape due to surface tension-driven flattening. The wavelength reduces with increased roller speed and reduced roller distance. The wavelength is more heavily affected by roller distance compared to speed. Critical parameters defining the instabilities and fluid properties such as  $dp/dx$ ,  $\dot{\gamma}$ , and  $\tau_w$  was successfully evaluated based on *Flow-3D*. The experimental ribbing wavelength strongly co-relates with these parameters. We have successfully demonstrated an effective method to predict these critical parameters by the simulation, which the conventional rollers cannot measure as they are not viscometric.

## CHAPTER 5 : Periodic Micro-grating structure Fabrication

### 5.1 Background

Based on the learning from the CFD model and roll-coating of PDMS, a parametric analysis was conducted for CNT-PDMS composite paste. A wide variety of coating paste with different inclusion of vol% was utilized for roll-coating to first study the pattern generation. Finally, after narrowing down the process parameters, final samples were fabricated that contained the periodic microstructures.

### 5.2 Experimental Methods

#### 5.2.1 Forward Roll Coating

A two-roll coating machine was utilized to fabricate the samples and analyze the ribbing behavior (Figure 5.1). Each with a radius ( $R$ ) of 25.4 mm, the rollers run with independent motors that can control the angular speed from 0 to 120 rpm. To transfer the composite film after roll-coating, a removable polyimide sleeve was inserted on roller #1. The coating materials were inserted between two rollers and were introduced to different process conditions by controlling the roller velocities  $U_1$ ,  $U_2$ , and the roller distance of  $d$ . Finally, the micro-structure composite film was oven-cured at 125°C for 25 minutes. An example of a roll-coated sample with linearly periodic microstructure is observed in Figure 5.1d-e, and leaf-vein patterns observed in Figure 5.1g-h showing both ribbing and filamentation phenomena.

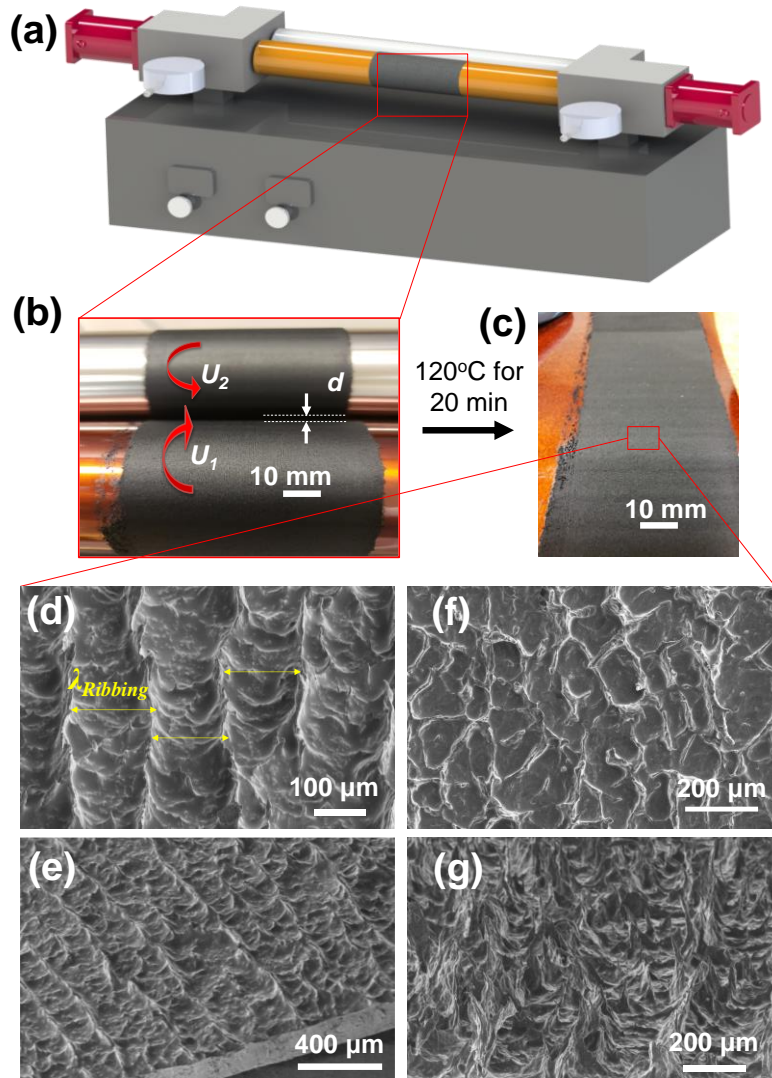


**Figure 5.1** (a) Two roll coating machines. (b) Forward roll coating of composite paste; (c) Fabricated sample after heat-cure. (d-e) SEM image showing the micro-trench formation and the peak-formations due to filamentation on a linearly periodic sample. (f-g) SEM images show high aspect-ratio patterns similar to veins of a leaf, as the  $R/d$  crosses a critical value.

### 5.2.2 Surface Morphology Characterization

The surface roughness and waviness of the samples were characterized by a non-contacting laser scanning confocal microscope (Keyence VK-X1100, 0.5 nm height resolution,

and 1 nm width resolution). Several roughness descriptors, such as the Wenzel roughness factor ( $r$ ), the density of peaks ( $Spd$ ), and arithmetic mean wavelength ( $\lambda$ ), were evaluated from the laser confocal data. The surface morphology was also investigated with a high-resolution scanning electron microscope (FEI Verios 460 L). Figure 5.2a shows the linearly spaced patterns with both ribbing and filamentation. Multiple horizontal and vertical lines were drawn with the multifile analyzer to evaluate the laser confocal data. Each of the lines shows wavy patterns, as observed in Figure 5.2c. However, the lines were next smoothed to quantify the periodicity. The reported values are the average periodicity.

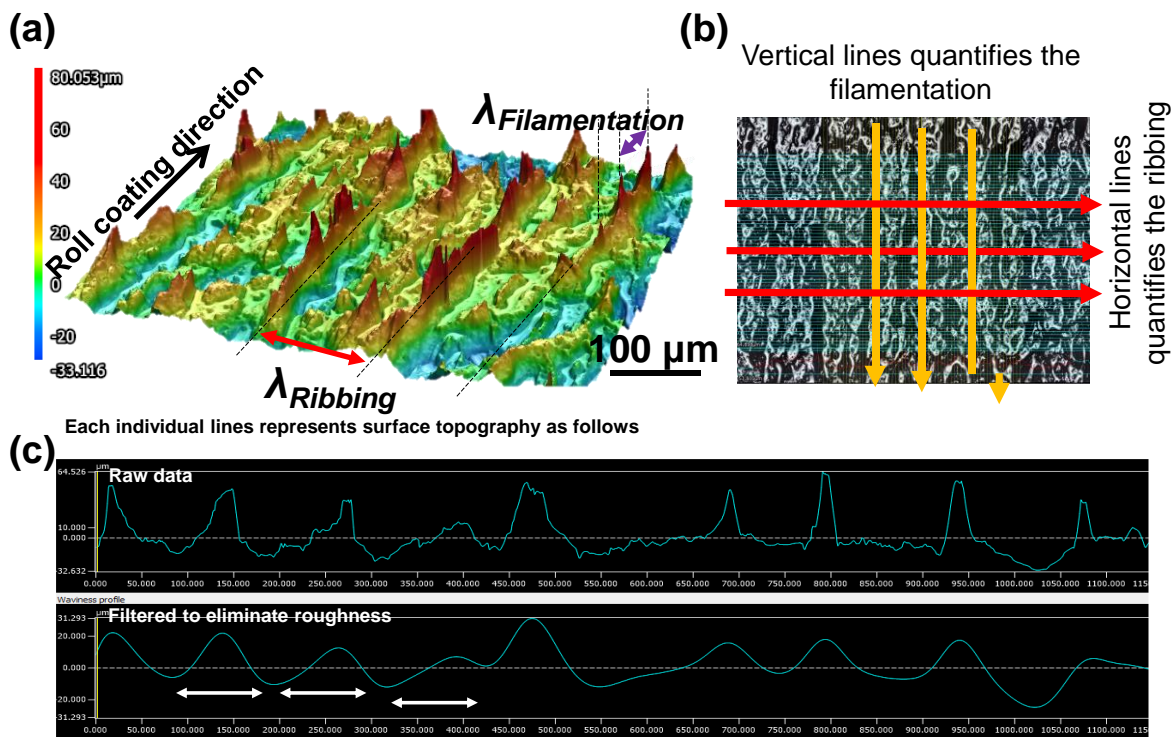


**Figure 5.2** (a) 3D images of the samples by a confocal laser microscope. (b) Top view of the scanned surface with horizontal and vertical lines (lines not drawn to scale) to estimate the periodicity of the samples. (c) Topography of a sample horizontal line showing the waviness of the surface.

### 5.2.3 Contact Angle Measurement

Contact angle measurements were conducted with a Ramé-hart goniometer (model 250) at ambient temperature (22 – 25°C). A water droplet of 2  $\mu\text{L}$  was carefully deposited onto the sample surface, and the syringe was withdrawn immediately. The water droplet images were captured in 5 different sample locations by a charge-coupled device camera and a 150 W fiber optic illuminator. Finally, the water contact angle was measured using the low-bond axisymmetric drop shape analysis plugin provided by the ImageJ software [101].

### 5.2.4 High-speed Imaging

A Photron SA-X2 high-speed Camera was utilized to observe the roll-coating process with a Sigma 1800 mm macro lens. The images were collected at 200 frames per second (fps). The PDMS ribbing pattern was collected in a high-resolution camera. The collected images were processed by ImageJ software to analyze the wavelength patterns [102].

## 5.3 Results and Discussion

### 5.3.1. Ribbing Instabilities in Roll-coating of PDMS Composites

The CNTs were next introduced into the PDMS to tailor the viscoelastic properties of the coating materials. To avoid surface flattening when the rollers stop, a yielding material is necessary, which will selectively behave like a fluid in elevated shear stress but behave as a solid when the stress is unloaded. The entanglement of the cylindrical-shaped CNTs allowed such behavior. Composite paste with various concentrations of the CNTs was synthesized and utilized in the roll-coating process. At first, 0.27 vol% and 0.54 vol% CNT were added to the PDMS matrix, and the roll-coating was observed in a high-speed camera.

Similar to the PDMS, ribbing formation is observed for 0.27 vol% CNT-PDMS composite (Figure 5.3). However, another phenomenon known as filamentation was also observed during the roll-coating [103]. A small hole appears, generating a filament at the roller's interface. As the roller rotates, the hole becomes larger as the filament stretches, eventually breaking and developing a peak on top of the ribs (Figure 5.3). The produced surface is thus a hybrid of ribbing formation and peaks from filamentation rupture. The elastic relaxation of the composite paste has a crucial effect in the generation of such micro-peaks, with lower elastic materials expected to have shorter peaks [103]. Future studies will investigate the extensional viscoelasticity of the composite paste and how it influences the instabilities in roll-coating.

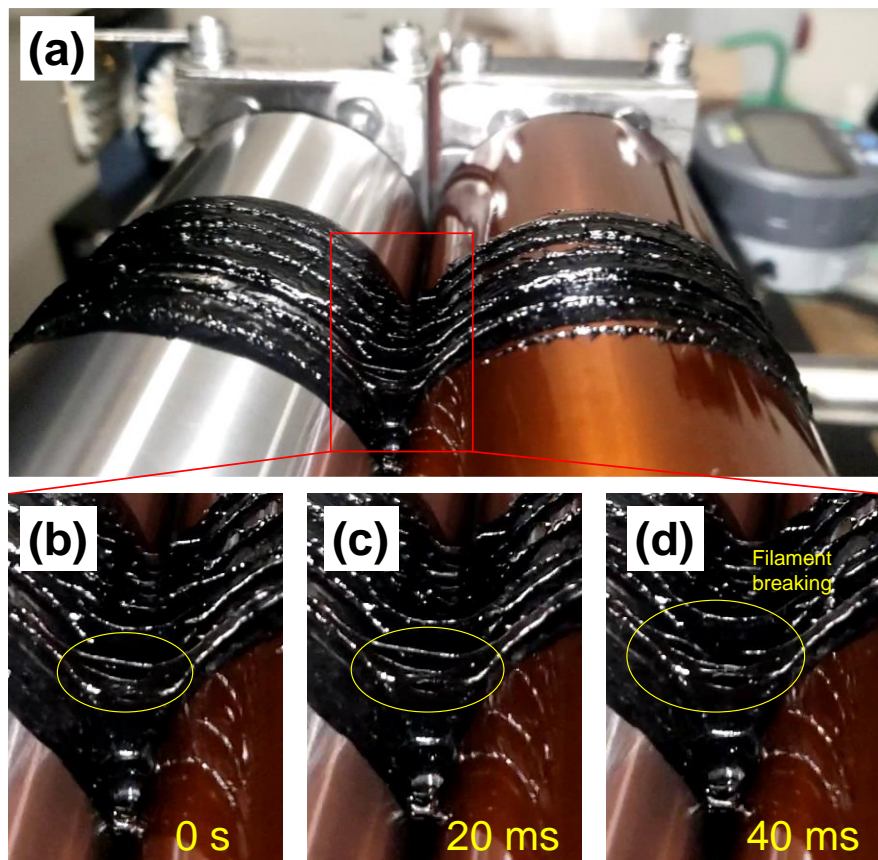


**Figure 5.3** (a) Filamentation phenomenon on 0.27 vol% CNT-PDMS composite roll-coating. (b) Filament initiation. (c) Filament elongation. (d) Filament breakage.

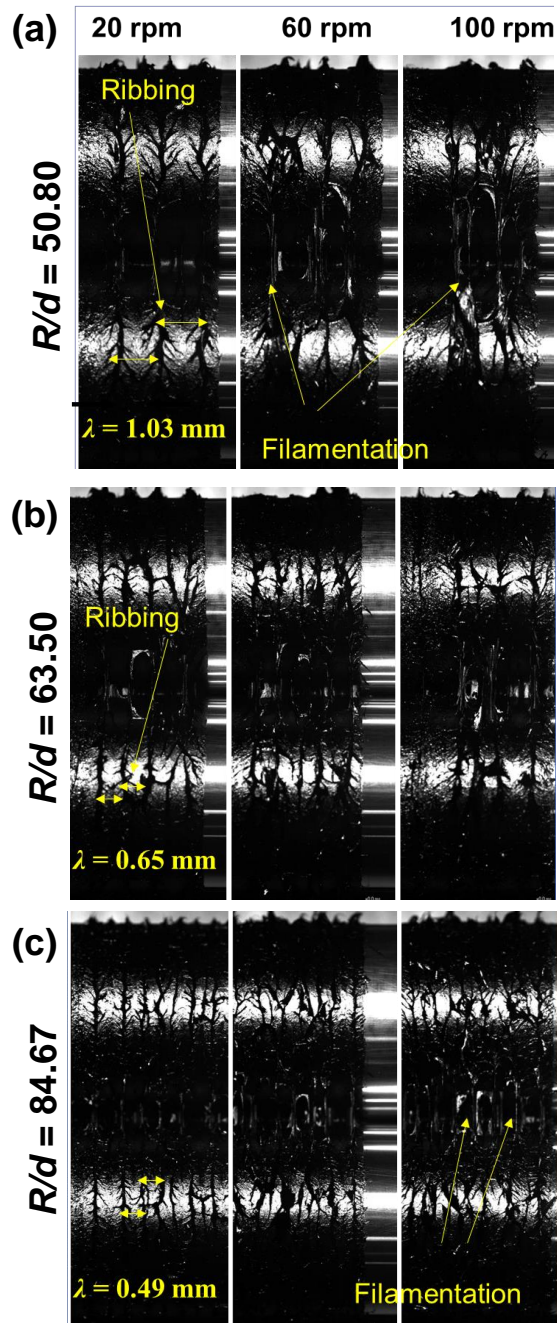


**Figure 5.4** High-speed images were captured for roll coating of 0.54 vol% CNT-PDMS for various roll-coating speeds of 20 rpm, 60 rpm, and 100 rpm for  $R/d$  of (a) 50.80, (b) 63.5, and (c) 84.67. The ribbing was relatively stable at a lower speed, whereas the higher speed incurred more filamentation and tip-splitting.

Figure 5.4 shows the high-speed images of roll-coating with 0.54 vol% of CNT-PDMS. Roller speeds of 20, 60, and 100 rpm and  $R/d$  of 50.8, 63.5, and 84.67 are presented. The observed hybrid pattern is similar to 0.27 vol% CNT-PDMS results. At 20 rpm speed, the wavelength reduces from 1.03 mm to 0.49 mm with an  $R/d$  increment from 50.8 to 84.67. Notice that the ribbing wavelengths in PDMS ranged from 2.8-5.32 mm, whereas the wavelength significantly reduced with the addition of CNTs. This is primarily due to the higher viscosity of the coating paste, causing more dramatic  $dp/dx$  resulting in a shorter wavelength. In addition, the linearity of the wavelength formation is also compromised at higher speed and  $R/d$ .

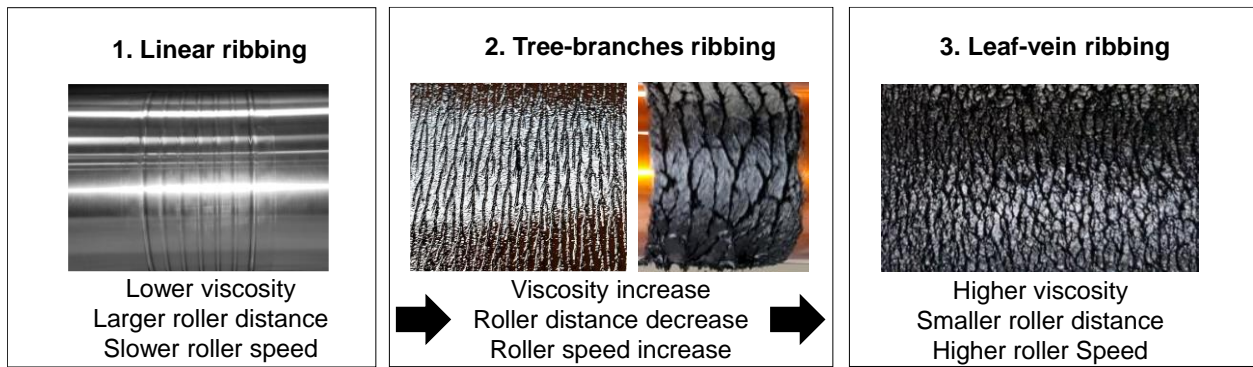


**Figure 5.5** Patterns classification occurring by ribbing and filamentations. The patterns begin from linear to tree branches, and finally, leaf-vein-shaped random structure.

The roll coating of 0.27 and 0.54 vol% CNT-PDMS provided essential insights. (i) The wavelength reduced significantly compared to the PDMS as the viscosity and elasticity increased. (ii) An additional mode for pattern formation known as filamentation was also observed, which affects the final patterns. (iii) At a lower velocity, it was observed that the patterns were more likely to align linearly. (iv) The ribbing wavelength change is more sensitive to the  $R/d$ , which is also observed in the roll coating of the PDMS. The observed patterns during the roll-coating were broadly classified into three phases (Figure 5.5). Materials with lower

viscosity and less dominant elastic properties, such as PDMS S184, showed linearly spaced riblets during slower roller speed. However, when the nanoparticles are introduced to achieve higher viscosity materials with yield behavior, the patterns begin to show a more complex nature. Initially, the patterns transform into a tree-branch shape as the riblets begin to merge and separate as the instability increases. However, as the viscosity of the materials increases even further, with further higher speed and narrower roller distance, the generated patterns form like a leaf-vein network shape where the riblets connect diagonally. These findings guided subsequent experimentation with higher vol% CNTs for potentially achieving ribbing wavelength in the micron range.

One initially observed dilemma was that the linearly periodic patterns did not retain shape when the roller stopped as the materials did not possess yield stress. The following experiment was conducted to retain the shape of the linearly spaced patterns potentially. Based on the assumption that materials with lower surface energy yet higher viscosity with yield stress might retain the shape in the linear ribbing region. As discussed in Table 1.2, PDMS S186 composites displayed lower surface energy of 17.9-18.8 mJ m<sup>-2</sup> whereas PDMS S184-based materials showed 21.85-23.23 mJ m<sup>-2</sup>. Figure 5.6 shows the linearly periodic patterns generated by S186-6.9vol% SiO<sub>2</sub> and S186-0.98 vol% CNT composited at a roller speed of 10 rpm. The generated patterns are sustained for each of the materials when the rollers stop as the materials have yield stress, as discussed in section 3.3.2. Figure 5.7a shows the laser confocal images of the heat-cured samples to quantify the ribbing wavelengths. The S186-6.9vol% SiO<sub>2</sub> composite shows the wavelength of 3.11, 2.63, 2.4, and 1.64 mm at  $R/d$  of 127, 169, 254, and 508 consecutively. At the same time, S186-0.98 vol% CNT results in 1.54, 1.28, and 0.98 mm of wavelength at  $R/d$  of 169, 254, and 508. With both materials, the wavelength reduces with an

increase of  $R/d$ , whereas the cylindrical CNTs with lower vol% result in smaller ribbing wavelengths for the same process parameters attributed to their higher viscosity.

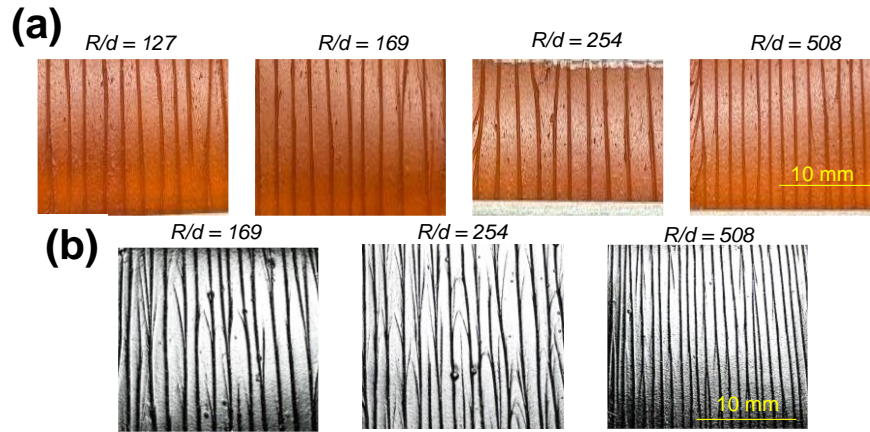


**Figure 5.6** (a) Photographs of 6.9 vol% of  $\text{SiO}_2$  – S186 samples for various  $R/d$  at a roller speed of 10 rpm. (b) Photographs of 0.98 vol% of CNT – S186 samples for various  $R/d$ .

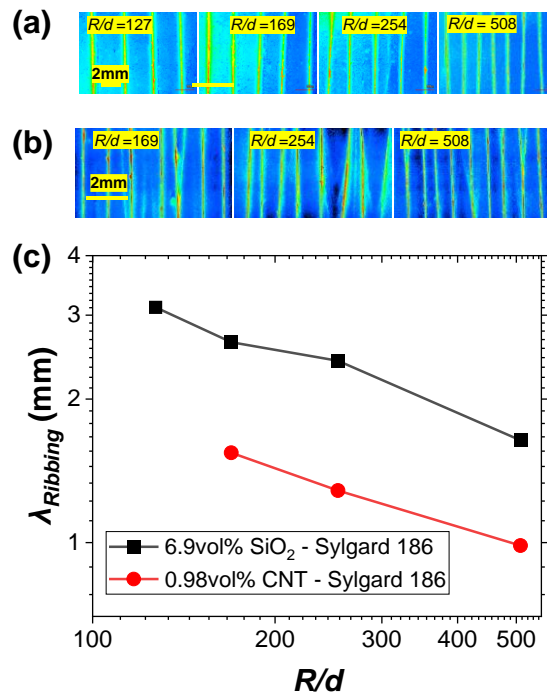


**Figure 5.7** Laser confocal images of (a) 6.9 vol% of  $\text{SiO}_2$  – S186 and (b) 0.98 vol% of CNT – S186 samples for various  $R/d$ . (c) Measured ribbing wavelengths of the sample vs.  $R/d$ .

### 5.3.2. Scanning Electron Microscopy

Coating pastes were prepared by adding various vol% of CNTs to the PDMS. 1.65-1.93 vol% CNT-PDMS provided the most linearly periodic samples upon extensive experimentation. As the vol% of CNTs increases, the higher viscosity and elasticity cause the generated pattern to be more random. For example, no forms of linearity were observed in roll coating samples with  $> 3$  vol% CNTs. Herein, the 1.65 vol% and 1.93 vol% CNTs-PDMS samples are presented. To analyze the surface morphology, the roll-coated samples were heat-cured and observed by SEM and laser confocal microscopy.

The 1.65 vol% CNT-PDMS sample showed ribbing instabilities and produced a micro-trench profile at  $R/d$  of 63.5 at 50 rpm roller speed (Figure 5.8). However, an attempt to further reduce the ribbing wavelength by increasing the  $R/d$  resulted in a linear to leaf-vein shape transition at  $R/d = 84.67$ . A further increase in  $R/d$  to 101.6 results in leaf-vein shape samples with a high aspect ratio with a large ribbing wavelength at a millimeter scale.

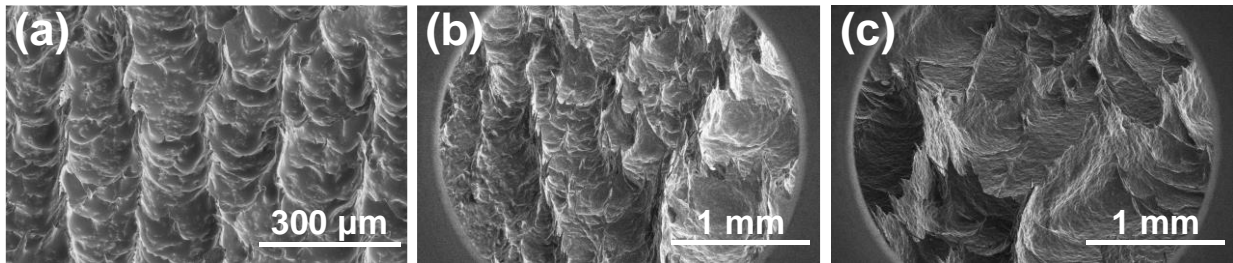


**Figure 5.8** SEM images of 1.65 vol% CNT-PDMS samples at 50 rpm speed, and (a)  $R/d = 63.5$ , (b)  $R/d = 84.67$ , and (c)  $R/d = 101.6$ .

Next, the 1.93 vol% CNT-PDMS composite paste was utilized to reduce the ribbing wavelengths. The roller's speed was fixed at 20 rpm, while the  $R/d$  varied from 56.44 to 127. The 1.93 vol% CNT-PDMS samples showed a hybrid microstructure created by ribbing and

filamentation similar to 0.27 and 0.54 vol% CNT-PDMS. While the ribbing waves were observed transverse to the roll-coating direction, filamentation resulted in many micro-peaks in the longitudinal direction. The camera images and SEM images of the samples are shown in Figure 5.9. The samples  $R/d = 56.44, 63.50, 72.57,$  and  $84.67$  showed mostly linear ribbing formation, whereas the  $R/d = 101.60$  transitioned to a more random microstructure. Despite less consistent micro-trenches in comparison to 1.65 vol% CNT-PDMS samples, it was possible to achieve shorter  $\lambda_{Ribbing}$ . The ribbing wavelengths were reduced from  $700 \mu\text{m}$  to  $90 \mu\text{m}$  for the linear-microstructure sample (Figure 5.9). The randomness increased to taller features at  $R/d > 84.67$ . At this point, roller speed was further increased to observe the effect on the generated pattern to generate highly rough samples. The samples at 40 and 80 rpm with  $R/d$  of 101.6 and 127 showed highly dense micro-peaks and a high aspect ratio (Figure 5.10). Notice that although the 40 rpm samples show uniformly rough samples, the 80 rpm samples show more nonuniformity. The entangled CNTs with their yield stress allowed the PDMS to retain the complex microstructure after roll-coating by resisting the surface tension-driven flattening.

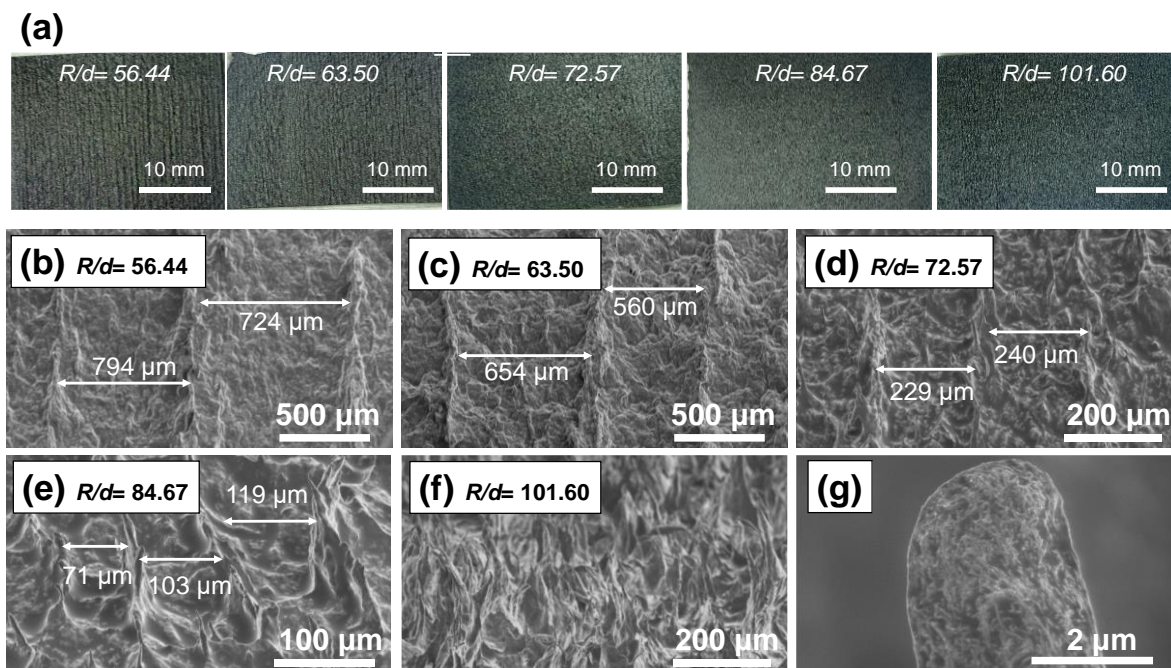


**Figure 5.9** (a) Photographs of fabricated samples using  $R/d = 56.44$ ,  $63.50$ ,  $72.57$ ,  $84.67$ , and  $101.60$ . (b-f) SEM images of samples fabricated with the same  $R/d$  ratios; (g) High-magnification SEM image of an individual peak of the samples showing CNT distribution in PDMS

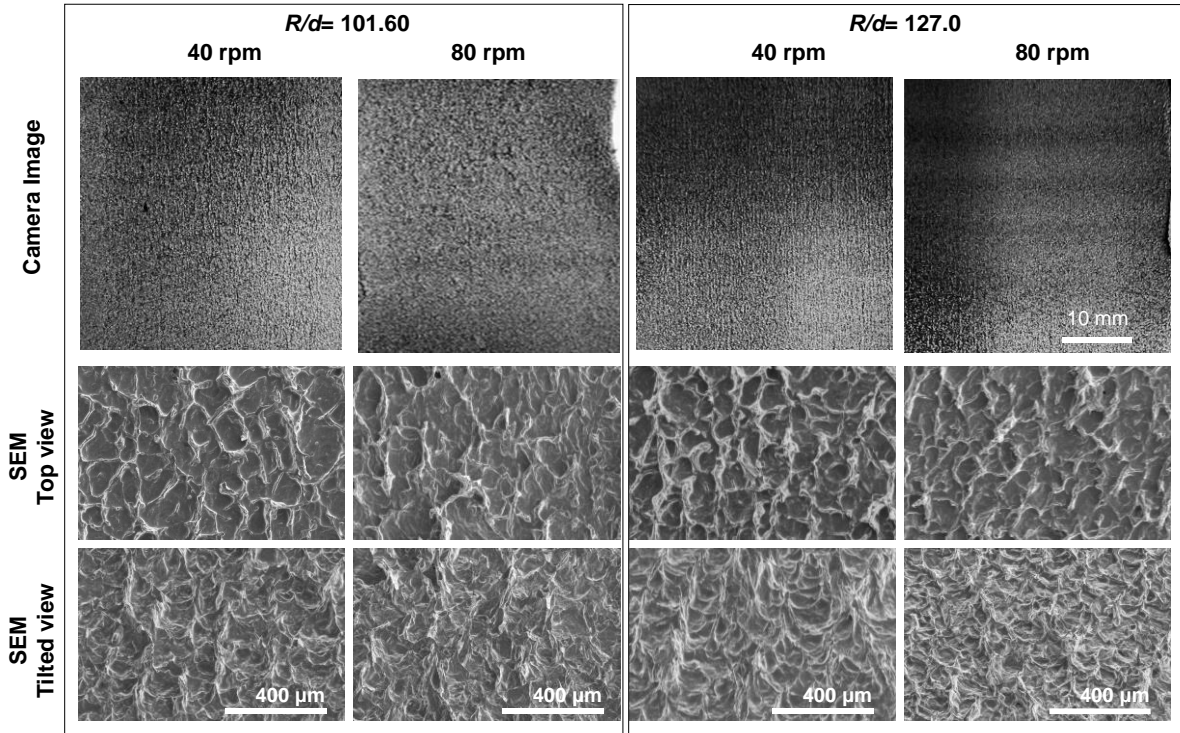


**Figure 5.10** Photographs and SEM images of leaf-vein-shaped samples fabricated at 40 and 80 rpm at  $R/d$  of 101.6 and 127.

### 5.3.3. Confocal Laser Microscope

Since the SEM shows only a small area of the samples, a laser confocal microscope was utilized to quantify the wavelengths and surface roughness. Figure 5.11 shows an example of samples' three-dimensional (3D) topography. The ribbing wavelength ( $\lambda_{Ribbing}$ ), as described earlier, is defined as the distance between each transverse riblet. The filamentation wavelength ( $\lambda_{Filamentation}$ ) is the peak-to-peak distance in the longitudinal direction, as shown in Figure 5.2. The samples included random microstructures along with the linearly periodic patterns. To quantify the wavelengths, multiple (>20) transverse and longitudinal lines (were drawn on the 3D surface with the Multifile-analyzer software (Keyence). Each of these lines showed the peaks

and valleys of the surface topography. The wavelengths for these individual lines are evaluated by the software, and the average values are presented in Figure 5.11. The wavelengths reduce for both ribbing and filamentation phenomenon with an increase in  $R/d$ , associated with more instabilities. The average  $\lambda_{Ribbing}$  was 777, 618, 148, 114  $\mu\text{m}$  for the  $R/d=56.44, 63.50, 72.57,$  and 84.67 samples. However, when the linear microstructure transitions to a leaf-vein microstructure at  $R/d > 84.67$ , the wavelength increases to 224  $\mu\text{m}$ . The average  $\lambda_{Filamentation}$  also follows the same pattern as the observed wavelengths were 455, 337, 200, 146, 230, and 242.98  $\mu\text{m}$  for the  $R/d=56.44, 63.50, 72.57, 84.67, 101.60,$  and 127. The Wenzel roughness factor ( $r$ ) was also evaluated, which is discussed in the following section in conjunction with the water contact angle measurement result.

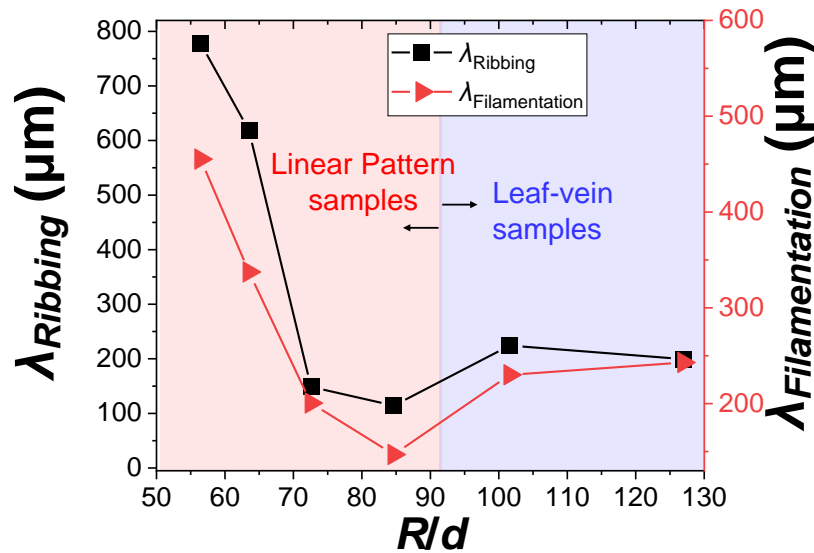


**Figure 5.11** Ribbing wavelength ( $\lambda_{Ribbing}$ ) and filamentation wavelengths ( $\lambda_{Filamentation}$ ) of the fabricated samples vs.  $R/d$ . The wavelengths decrease with increased  $R/d$  until the pattern transforms from linearly periodic to leaf-vein shape.

### 5.3.4. Water Contact Angle Measurement

The water contact angles (WCA) of the micro-structured samples were measured to demonstrate the hydrophobicity of the surface (Figure 5.12). The measurements were performed in 5 different locations for each of the samples. The average WCA of the linear micro-structured samples were  $128.17^\circ$ ,  $133.64^\circ$ ,  $136.98^\circ$ , and  $137.27^\circ$  for  $R/d = 56.44$ ,  $63.5$ ,  $72.57$ , and  $84.67$ , respectively. In comparison, a compression-molded flat CNT-PDMS sample showed a WCA of  $115.4^\circ$ . Thus, the increased WCA to  $R/d$  is related to the roughness of the fabricated sample. However, the trend stalls right before the transition from a linearly periodic microstructure to a high aspect-ratio random microstructure. The WCA dramatically increases into the superhydrophobic range to  $150.63^\circ$  and  $158.13^\circ$  for  $R/d = 101.6$  and  $127$ . This is primarily due to the increase in the surface area of the samples due to enhanced hierarchical structure geometry, which is also reflected in the high Wenzel roughness factor of  $\sim 3.5$ . The WCA and the Wenzel roughness factors matched well (Figure 5.12).

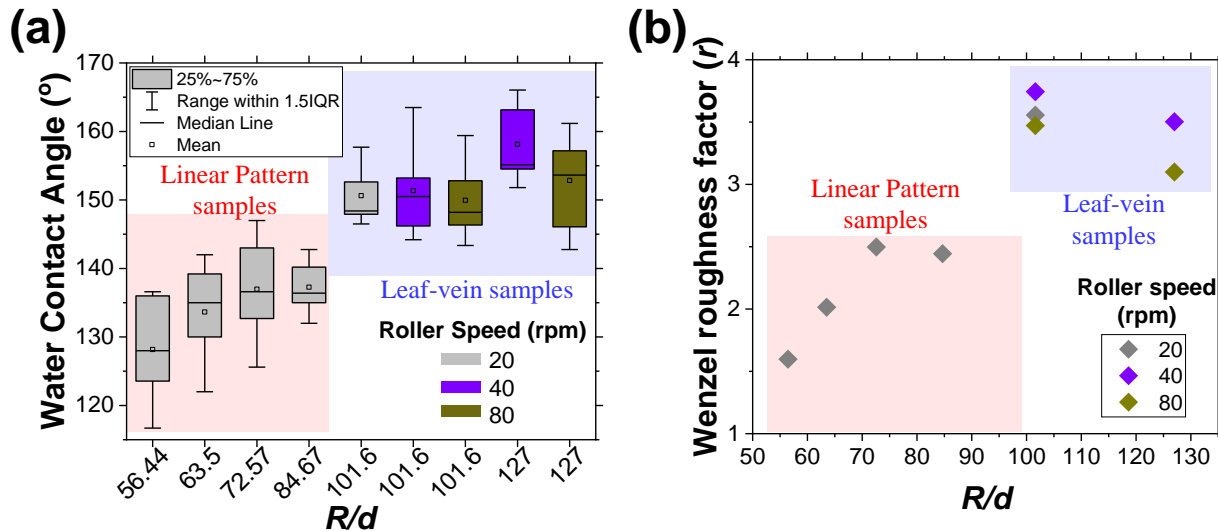


**Figure 5.12** (a) Water contact angle measurements boxplot at five different locations of each sample. (b) Wenzel roughness factor vs.  $R/d$

### 5.3.5. CFD Analysis of the Observed Surface Morphology

The roll-coated samples were broadly classified into two categories based on the microstructures. The generated patterns were mostly linearly periodic samples for the 1.93 vol% CNT-PDMS samples with 20 rpm speed and  $R/d \leq 84.67$  (Figure 5.9 and 5.10). Whereas samples with  $R/d$  101.6 and 127 showed more leaf-vein shape structure with high aspect ratios. The results indicate a significant alteration in the ribbing formation after the critical  $R/d$  value of 84.67. However, since the roll-coating experiment itself could not provide further information on the state of the coating paste, such as the fluid velocity, pressure gradient, shear rate, and wall shear stress, further CFD analysis was conducted to evaluate these parameters and potentially correlate with the experimental results observed by the SEM and laser-confocal. The CFD analysis was conducted in a similar method mentioned in section 4.2.1.

The pressure gradient in the direction of fluid flow,  $dp/dx$  for 1.93 vol% CNT-PDMS, was observed to be an order of magnitude higher than PDMS. The  $dp/dx$  ranged from 667 MPa  $m^{-1}$  to 3138 MPa  $m^{-1}$  for  $R/d$  of 56.4 to 127, respectively (Figure 5.13a). The enormous increase in pressure gradient is sourced from the elastic nature of the viscoelastic fluid, which restricts the flow and increases the stress significantly [42]. The high  $dp/dx$  results in much more aggressive ribbing instability even at a slower roller speed than PDMS. The associated shear rate during the roll-coating experiments was also evaluated based on the CFD analysis. The roll coating of 1.93 vol% CNT-PDMS at 20 rpm speed results in the shear rate of 54.02, 80.81, 93.04, 116.37, 119.87, and 154  $s^{-1}$  for  $R/d$  of 56.44, 63.5, 72.57, 84.67, 101.6, and 127, respectively. Notice that the wall shear stress steadily increases from 0.3 MPa to 0.41 MPa for  $R/d$  of 56.44 to 84.67, respectively. However, at  $R/d$  101.6, when the shear rate is 119.87  $s^{-1}$ , the wall shear stress increases sharply to 0.45 MPa (Figure 5.13b). As observed in prior studies, the abrupt change in

wall shear stress results in further tip-splitting, which results in the leaf-vein shape structure. Grillet et al. observed similar tip-splitting behaviour specifically for elastic materials and noticed that an increased elasticity dramatically changes the shape structure to be more random [35]. The CFD analysis of the roll coating of 1.93 vol% CNT-PDMS helped to uncover the critical roll coating process parameter along with the associated  $dp/dx$ ,  $\dot{\gamma}$ , and  $\tau_w$  that contribute for the transitions between the linear to leaf-vein shape formation.

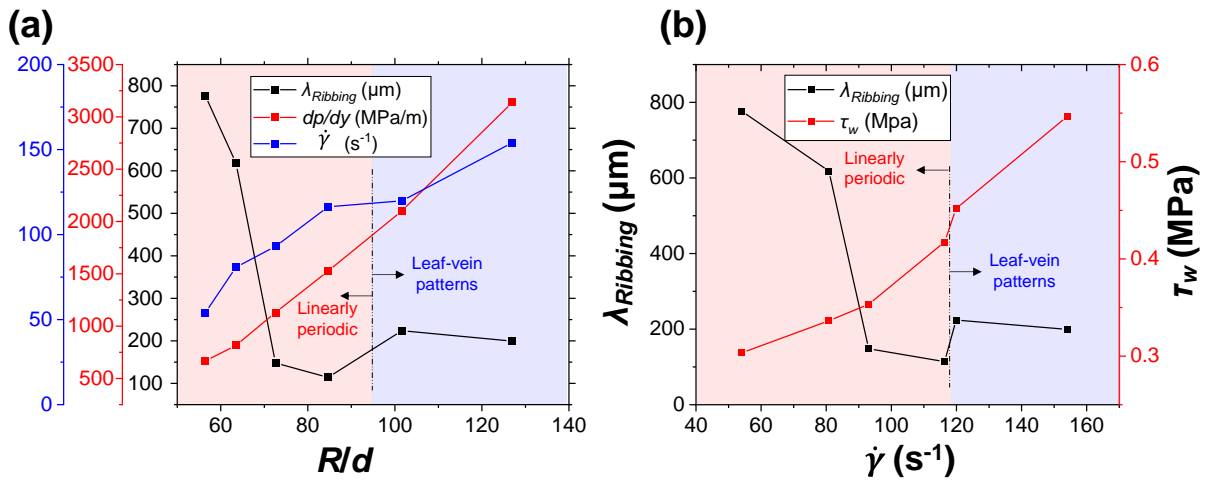


**Figure 5.13** CFD simulation results for roll-coating of 1.93 vol% CNT-PDMS under various process conditions. (a)  $\lambda_{Ribbing}$ ,  $dp/dx$ , and  $\dot{\gamma}$  vs.  $R/d$ . (b)  $\lambda_{Ribbing}$  and wall shear stress vs.  $\dot{\gamma}$ .

## 5.4 Conclusions

Increasing the CNT content to 2.08vol% on the S184 allows the polymer to retain shape even after roll-coating is stopped due to the high viscosity to surface energy ratio. Also, the ribbing instabilities help to achieve controllable linear micro-trenches of 114-777  $\mu\text{m}$  periodicity. However, as the roller distance decreases further to increase the  $R/d$  to 101.60, the linear ribbing transitions into the high aspect-ratio leaf-vein-shaped microstructure. The water contact angle of the samples ranged from  $128.17^\circ$  to  $163.63^\circ$ . The linear microstructure films can be essential in

mass manufacturing drag reduction surfaces. At the same time, the high aspect-ratio random microstructure films can have applications in superhydrophobic, self-cleaning, anti-icing, and anti-biofouling surfaces.

## CHAPTER 6 : Multifunctional Applications of Superhydrophobic Surfaces

### 6.1 Background

The fabricated samples were investigated for multifunctional applications, including SHPo drag reduction, loading capacity increase, electrical properties, and mechanical properties. Some future experiments are focused on biofouling applications and radiative cooling applications.

### 6.2 Experimental Methods

#### 6.2.1 Drag Reduction and Loading Capacity Test

The hydrodynamic drag reduction of the sample was measured by using a pulley system that attaches to a miniature boat (Figure 6.1). The SHPo sample surface was attached to the bottom of a model boat. Another boat with the same weight without the functional bottom surface was used as a reference. A mass was used to create a steady tension force ( $F$ ) on the surface was used as a reference. A mass was used to create a steady tension force ( $F$ ) on the miniature boat. Also, four different masses (1.7, 0.8, 0.6, and 0.5 g) were utilized to accelerate the boats, resulting in different Froude numbers and Reynolds numbers. The time required for the boat to travel a 72-inch length tank with static water was measured. The velocity, Reynolds number, Froude number, and related acceleration were calculated from these times. Based on the acceleration of the boat, the  $F_{boat}$  was calculated. As observed in Figure 6.1 free-body diagram ignoring the frictional force from the pulleys, the drag-reduction force  $F_{DR} = F - F_{boat}$  was calculated.

The loading test was conducted similarly to the drag-reduction test by attaching the SHPo surface at the bottom of a model boat. The reference boat and the SHPo surface boat had the same initial weight. The maximum weight was put on the boats until they sank into the water.

The loading capacity increase was calculated as the percentage increment in the maximum load of the boats with the addition of an SHPo surface sample.

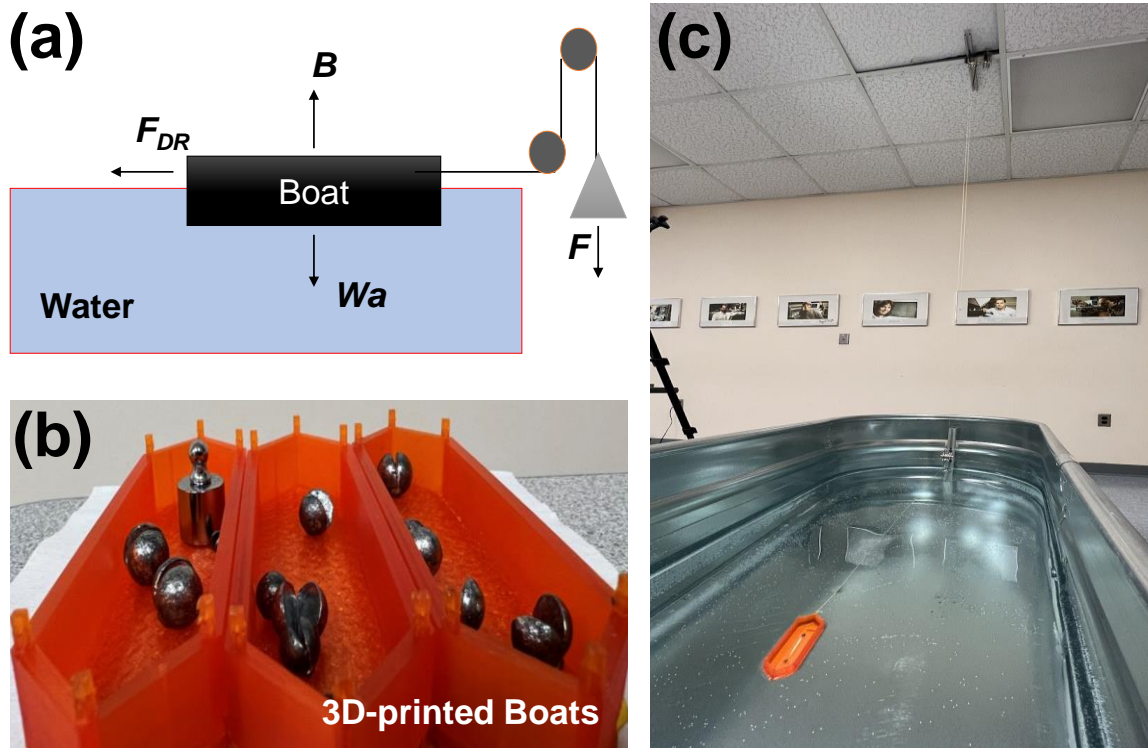


**Figure 6.1** (a) The free-body diagram of the drag-reduction experimental setup. (b) Miniature model boats with standard loads. (c) Experimental setup

### 6.2.2 Mechanical Scratch Testing

A Nanovea CB500 mechanical tester was utilized to examine the robustness of the 1.93 vol% CNT-PDMS micropatterned surface. A spherical-shaped indenter (6-mm diameter) was used to scratch the 6 – 8 mm sample length at  $6 \text{ mm min}^{-1}$  speed (Figure 6.2). A progressive normal load ( $F_N$ ) of 1 – 20 N was applied to the sample at a  $19 \text{ N min}^{-1}$  loading rate. The machine measured the frictional force ( $F_{fr}$ ) corresponding to the applied normal force. The frictional coefficient was evaluated as  $f = F_N/F_{fr}$ . The data were plotted against the scratch

length. The first sudden change in the frictional force or coefficient was considered materials' cohesive failure or mode-1 failure ( $L_{c1}$ ). The second abrupt change in the data is the adhesive failure or mode-2 failure ( $L_{c2}$ ) [104,105].

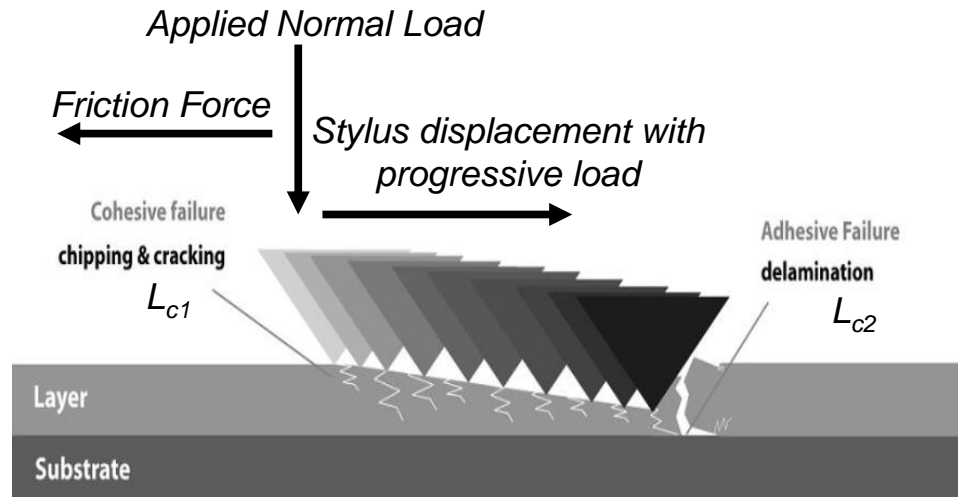


**Figure 6.2** Mechanical scratch testing of the samples showing cohesive and adhesive failure (image reconstructed based on [104,105])

### 6.2.3 Electrical Conductivity Measurements

The samples were prepared in the same method as the Surface energy measurement section mentioned (Figure 6.3). One additional step was conducted for the electrical conductivity measurement samples. After the samples were cured, they were cut into 2.54 mm by 2.54 mm square shapes.

The sheet resistivity of the CNT-PDMS composites was measured by the Van der Pauw method by a custom-made 4-point probe setup using Keithley 2400 source meter. Four uniform ohmic contacts of copper were placed at the four corners of the samples and connected to the source meter, as shown in Figure 6.3. A current was driven along one edge of the sample (for example,  $I_{AB}$ ) to make the measurement, and the corresponding voltage on the opposite edge  $V_{CD}$

was measured. For this particular case, the ohmic resistance  $R_{AB,CD}$  can be calculated based on Ohm's law as follows,

$$R_{AB,CD} = \frac{V_{CD}}{I_{AB}} \quad (6.1)$$

In this method, the resistance was measured both in horizontal and vertical directions by switching the probes, and the average  $R_{vertical}$  and  $R_{horizontal}$  value was calculated. Next, the sheet resistance  $R_s$  of the samples were measured by the Van der Pauw formula as follows,

$$e^{-\pi\left(\frac{R_{vertical}}{R_s}\right)} + e^{-\pi\left(\frac{R_{horizontal}}{R_s}\right)} = 1 \quad (6.2)$$

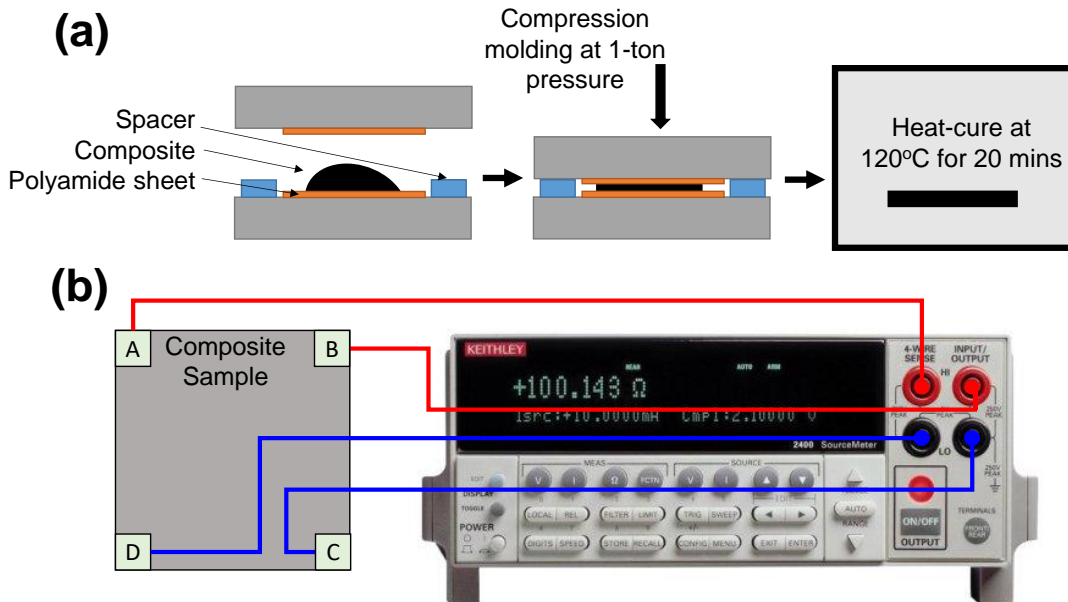


**Figure 6.3** (a) Sample preparation of CNT-PDMS composite sample for the electrical measurement (b) Electrical conductivity measurement setup using a custom-made 4-point probe following the Van-der-Pauw method.

## 6.3 Results and Discussion

### 6.3.1. Hydrodynamic Drag Reduction

The hydrodynamic drag reduction of the linear micro-structured sample was measured by attaching the sample to the underside of a miniature boat and pulling it parallel to the water

surface using a wire-and-pulley system (Figure 6.1). Weight was used to create a steady tension in the wire that pulls the boat with a constant force. Four different loads (1.7, 0.8, 0.6, and 0.5 g) were used for the boat to reach four different steady speeds. The time required for the boats to travel a set distance (180 cm) was measured, and the acceleration time was short enough to be ignored. The velocity, acceleration, Reynolds number ( $Re$ ), and Froude number ( $Fr$ ) of the boat and the velocity increase of the boats with the linear micro-structured sample relative to the ones without were calculated from the measured times. For Reynolds numbers 55397, 33163, 20677, and 15348, the velocity increases (or drag reductions) were 8.27, 8.68, 7.31, and 4.34%, respectively (Figure 6.4). This decrease of drag reduction with increasing Reynolds number, which deviates from what is known for laminar flows [73], can be explained by the large Froude number even at low Reynolds numbers due to the small boat size. Note that the drag of the boat in the current experiment comprises skin friction and wave-making, and the given sample can reduce only the skin-friction drag with no effect on the wave-making drag. When  $Fr < 0.25$ , the skin friction drag is dominant; however, the wave-making resistance dominates when  $Fr > 0.25$  [106]. When the Froude number increased (0.13, 0.18, 0.29, and 0.48, correspondingly) so that the portion of skin friction in the total drag decreased, the reduction of skin friction had a diminishing effect on the total drag. The sample with the densest linear patterns ( $R/d = 84.67$ ,  $\lambda_{Ribbing} = 114 \mu\text{m}$ ) was the most significant drag-reduction reported in this section. The samples with broader wavelengths did not have a conclusive result as they lack the ability to retain the plastorn.

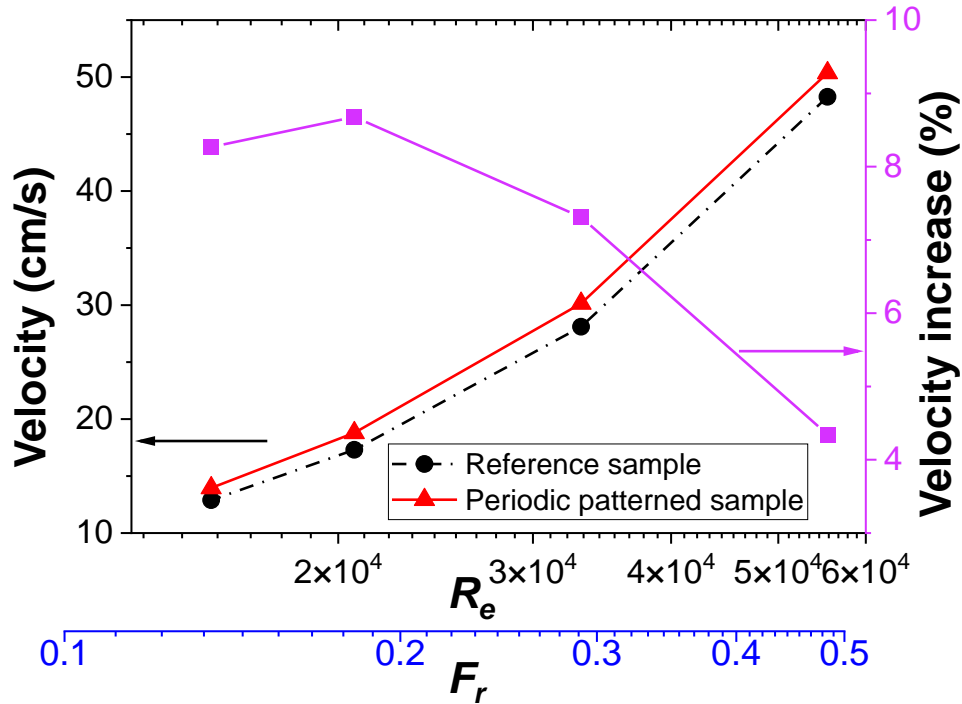


**Figure 6.4** Velocity profile of model boat with and without the linear micro-structured sample.

### 6.3.2. Loading Capacity Test

The loading capacity of miniature boats with and without the micro-nano textured surface was measured by placing masses on the boat while maintaining a constant center of gravity until the boats were submerged (Figure 6.5). The maximum load for the boat without the SHPo was 29.63 g, while the maximum load was 33.16 g for the boat with the SHPo. Thus, the loading capacity increased by 11.9% for the boat with the SHPo surface. The sample with the highest water contact angle ( $R/d = 127$ ) was chosen for this test due to the most significant superhydrophobicity. The loading capacity increase can be explained by the air entrapment on the SHPo surface, as observed in Figure 6.5a. The buoyancy force due to air entrapment depends on the air entrapment's surface area and the air film's thickness [107]. Because there is an evident air film thickness, the buoyancy force for the boat with the CNT-PDMS surface is much higher

than the boat without the CNT-PDMS surface. Therefore, an increase in loading capacity is observed.

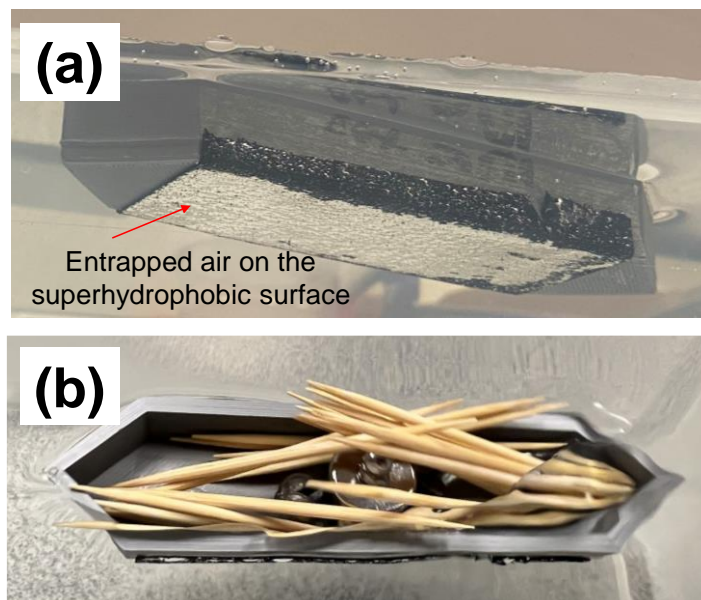


**Figure 6.5** (a) Entrapped air underneath the SHPo surface skin attached to the model boat (b) Loading test for the model boat with SHPo surface

### 6.3.3. Electrical Conductivity Measurements

The addition of a conductive filler in a non-conductive polymer matrix was found to incur electrical conductivity based on prior studies [108–110]. Since CNTs are highly conductive, there is a potentiality of achieving multifunctionality of the SHPo samples if electrical conductivity is also observed. The electrical sheet resistance of the samples was measured by a custom-made 4-point setup following the Van-der Paw method with varying CNT vol% and is represented in Figure 6.3b. It was found that CNT vol% of 0.27, 0.54, 0.82, 1.09, and 1.37 had sheet resistance values of 747.84, 190.36, 90.64, 36.26, and 22.66  $\Omega/\square$ , respectively (Figure 6.6). The decrease in sheet resistance because of increased CNTs creates a percolated network. As more CNTs are added, the percolation increases until a certain percolation

threshold. In a percolated network, electrons move across the network under an applied electrical field, which leads to an increase in electrical conductivity [111]. This increase in electrical conductivity, therefore, decreases the measured sheet resistance. Thus, as more CNTs are added, the percolated network grows and enables a decrease in the sheet resistance by increasing electrical conductivity. The PDMS-Sylgard 184 sample resistance was undetermined in the experiment, possibly due to very high resistivity.

This is also important to mention that Lee et al. [112] and Xu et al. [113], worked on manufacturing SHPo surfaces capable of plastron regeneration primarily by attaching additional conductive electrodes integrated into the surface, which allowed plastron regeneration by electrolysis when the water began to penetrate the micro-trench cavities (Figure 6.6b). However, the micro-trench structure fabricated in the present study would also be able to regenerate plastrons without additional electrode molding since the CNT-PDMS material is reasonably conductive. Further studies will be conducted in the future, focusing on the plastron regeneration capabilities of the manufactured SHPo surface in the presented study.

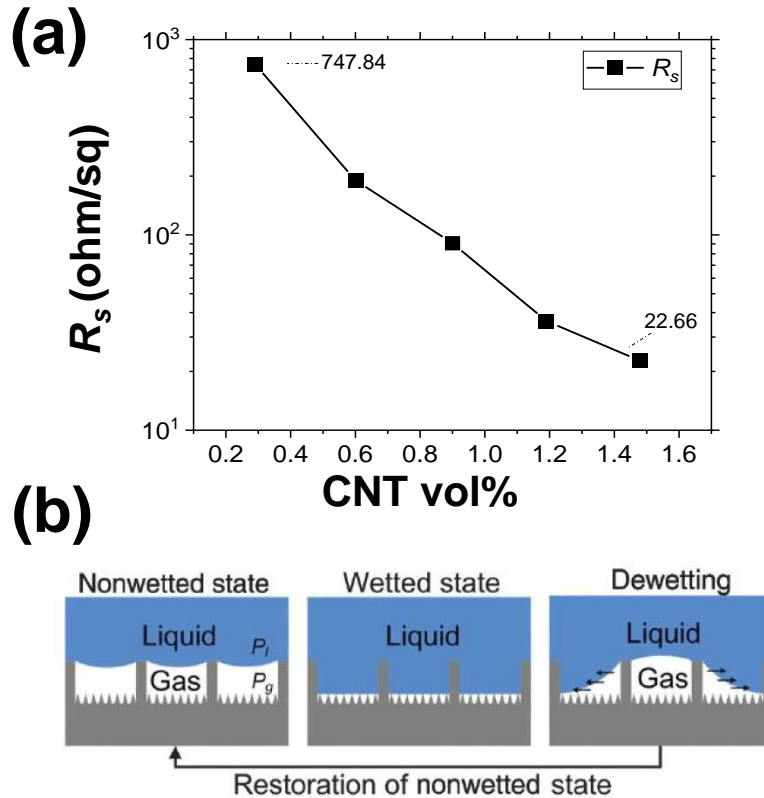


**Figure 6.6** Sheet resistance  $R_s$  of the CNT-PDMS composite samples fabricated in the current study. (b) Mechanisms of regenerative plastrons by work of Lee et al. [112].

#### 6.3.4. Scratch Testing

The robustness of the 1.93 vol% CNT-PDMS micro-structured sample was tested to identify the critical load of cohesive and adhesive failure. The critical load is the smallest load that causes microstructural damage for possible cracking or plastic deformation [104,105]. Although this test is not a comprehensive materials property test as the test parameters also have an effect, the critical load observed in such a scratch test is also a function of the mechanical strength of the materials. The first mode of failure, or the cohesive failure ( $L_{CI}$ ) in the CNT-PDMS sample, was observed for 7 N force as there seemed to be a sudden increase in the frictional force (Figure 6.7). The secondary failure was observed at 16 N, the adhesive failure between the test sample and the substrate. The frictional coefficient for the 1.93 vol% CNT-

PDMS composite was stable at  $\sim 0.2$ . Compared to the CNT-PDMS sample, the PDMS sample's cohesive failure occurred at a lower force of 3.6 N. The adhesive failure ( $L_{c2}$ ) was similar to the CNT-PDMS sample of 15.8 N force. The frictional coefficient of the PDMS sample seems to be much higher ( $\sim 0.35-0.45$ ) than the CNT-PDMS sample. The micro-structured surface assisted in this reduction in tribological friction, as observed in other studies [13,114]. The CNT addition helped the composite layer achieve superior mechanical properties compared to pure PDMS. Future studies will include the wear properties of the CNT-PDMS microstructures layer and underwater testing for a prolonged time to observe possible material degradation.

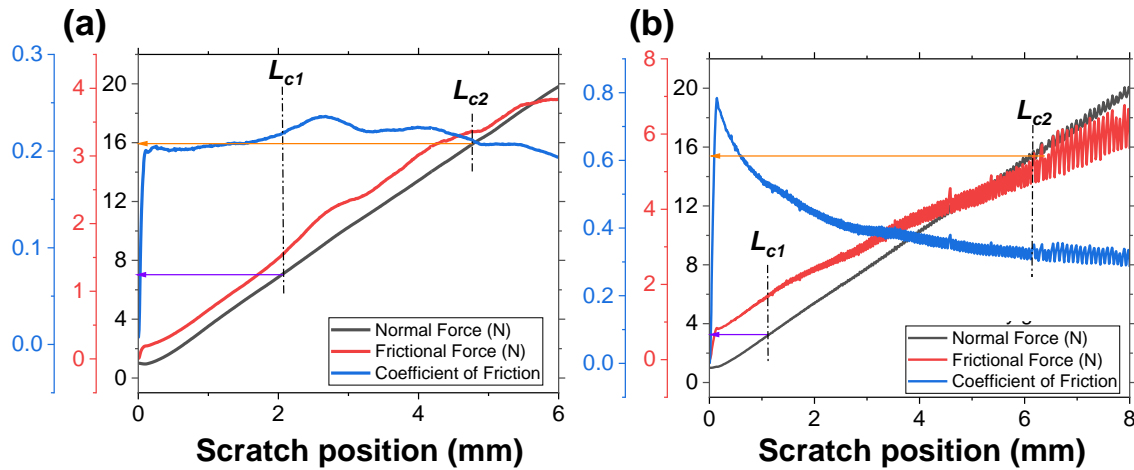


**Figure 6.7** Scratch test of (a) 2.08 vol% CNT-PDMS sample and (b) PDMS-Sylgard 184 sample.

## 6.4 Conclusions

The 3D printed boat showed 7 – 8% faster speed than the boat with a flat PDMS film when towed in a static water pool. The boat with the microstructured coating showed an 11.9% increased loading capacity by weight. The CNT-PDMS composite materials showed the reinforcement in mechanical properties as the cohesive failure occurs at 7 N force, whereas the

bare-PDMS fails at 3.6 N. CNT-PDMS films showed electric conductivity, where the sheet resistance reduces from 747.84 to 22.66  $\Omega/\square$  with 0.29 – 1.48 vol% of CNTs addition. The increase in electrical conductivity enables the potentiality of plastron regeneration capabilities in the SHPo drag-reduction.

## CHAPTER 7 : Conclusions and Future Works

### 7.1 Conclusions

A comprehensive investigation was conducted to study the ribbing formation during a roll-coating process both computationally and experimentally. First, ribbing instabilities for the pure PDMS were investigated. It was found that the pressure gradient occurring due to roller speed,  $R/d$ , and the material's viscoelastic properties is the key driving force of the ribbing instabilities. The wavelengths for the PDMS were observed in the 7.03 to 3.52 mm range for roller speeds from 30 to 100 rpm and  $R/d$  of 31.75 to 63.50. The ribbing formation of PDMS was also observed to flatten when the roller stops due to lower surface energy compared to the viscosity and also not having yield stress. Increasing the CNT content on the PDMS allows the polymer to retain its solid shape even after stopped roll-coating as yield stress of 0.0025, 0.01247, and 0.08737 MPa was observed for 0.54, 1.93, and 5.68 vol% of CNT-PDMS, respectively. The observed microstructure of the surfaces by the roll-coating was characterized as a hybrid pattern due to ribbing instability and filamentation due to elastic relaxation of the coating paste.

The manufactured samples showed a controllable 114-777  $\mu\text{m}$  periodicity. However, as the roller distance decreases further to increase the  $R/d$  to 101.60, the linear ribbing transitions into the random microstructure with a high Wenzel roughness factor ( $r$ ) of 3.56. The water contact angle of the samples ranged from 128.17° to 158.63°. The CNTs addition also made the samples conductive, opening opportunities for multifunctional applications. The mechanical durability of the fabricated microstructures is also investigated by scratch-testing. Finally, the fabricated pieces are also being employed to demonstrate drag-reduction capabilities in miniature model ships, self-cleaning surfaces, and anti-biofouling applications.

This study demonstrated a simple, scalable fabrication process to achieve periodic microstructures. The research helped to carefully identify and narrow down the suitable material composition and process parameters to control the micro-trench periodicity. However, the periodicity and continuity in the produced samples are far from the photolithography-based manufacturing techniques. However, the presented new technique has a huge potential moving forward for scalable manufacturing. The complete sample preparation takes only half an hour, beginning with the coating paste preparation, roll-coating, and heat-curing. The maximum size achievable with the presented two-roll-coater is 300 mm by 150 mm, only constrained by the diameter and length of the rollers. Taking advantage of the ribbing instabilities, a large periodic microstructured surface can be obtained quickly by employing a more robust roll-coater with continuous substrate-feeding capabilities. Future work will be focused on fine-tuning the process parameters, including new materials systems to improve the control of the surface morphology to move closer to the photolithography-based techniques.

## **7.2 Future Works**

Future research will first focus on investigating the potential of regenerative plastrons on the fabricated samples since CNT-PDMS was found to be conductive. We are also exploring potential applications in anti-biofouling, radiative cooling, and self-cleaning surfaces. The extensional viscosity and its effect on ribbing instabilities are also of interest to minimize the filamentation. New materials systems with different physical properties are also will be explored. Further study on physical properties of the materials system to design such materials to support manufacturing of continuous micro-grating trenches. We also want to design a roll-coating setup with a continuous feed of Web for larger-scale manufacturing.

## REFERENCES

- [1] X. Wang, B. Ding, J. Yu, M. Wang, Engineering biomimetic superhydrophobic surfaces of electrospun nanomaterials, *Nano Today*. 6 (2011) 510–530.  
<https://doi.org/10.1016/j.nantod.2011.08.004>.
- [2] Z. Guo, W. Liu, B.L. Su, Superhydrophobic surfaces: From natural to biomimetic to functional, *J. Colloid Interface Sci.* 353 (2011) 335–355.  
<https://doi.org/10.1016/j.jcis.2010.08.047>.
- [3] Q. Xu, W. Zhang, C. Dong, T.S. Sreeprasad, Z. Xia, Biomimetic self-cleaning surfaces: synthesis, mechanism and applications, *J. R. Soc. Interface*. 13 (2016) 20160300.  
<https://doi.org/10.1098/rsif.2016.0300>.
- [4] Q. Li, Z. Guo, Fundamentals of icing and common strategies for designing biomimetic anti-icing surfaces, *J. Mater. Chem. A*. 6 (2018) 13549–13581.  
<https://doi.org/10.1039/c8ta03259a>.
- [5] Y.Y. Yan, N. Gao, W. Barthlott, Mimicking natural superhydrophobic surfaces and grasping the wetting process: A review on recent progress in preparing superhydrophobic surfaces, *Adv. Colloid Interface Sci.* 169 (2011) 80–105.  
<https://doi.org/10.1016/j.cis.2011.08.005>.
- [6] B. Bhushan, Biomimetics: Lessons from Nature - an overview, *Philos. Trans. R. Soc. A Math. Phys. Eng. Sci.* 367 (2009) 1445–1486. <https://doi.org/10.1098/rsta.2009.0011>.
- [7] C. Zhang, D.A. Mcadams, J.C. Grunlan, Nano/Micro-Manufacturing of Bioinspired Materials: a Review of Methods to Mimic Natural Structures, *Adv. Mater.* 28 (2016) 8566–8566. <https://doi.org/10.1002/ADMA.201604494>.
- [8] T. Sun, L. Feng, X. Gao, L. Jiang, Bioinspired surfaces with special wettability, *Acc.*

- Chem. Res. 38 (2005) 644–652. <https://doi.org/10.1021/ar040224c>.
- [9] P. Vukusic, J.R. Sambles, Photonic structures in biology, *Nature*. 424 (2003) 852–855. <https://doi.org/10.1038/nature01941>.
- [10] M. Srinivasarao, Nano-Optics in the Biological World: Beetles, Butterflies, Birds, and Moths, *Chem. Rev.* 99 (1999) 1935–1961. <https://doi.org/10.1021/cr970080y>.
- [11] W. Yu, J. Koc, J.A. Finlay, J.L. Clarke, A.S. Clare, A. Rosenhahn, Layer-by-layer constructed hyaluronic acid/chitosan multilayers as antifouling and fouling-release coatings, *Biointerphases*. 14 (2019) 051002. <https://doi.org/10.1116/1.5110887>.
- [12] M.D. Ibrahim, S.N.A. Amran, Y.S. Yunus, M.R.A. Rahman, M.Z. Mohtar, L.K. Wong, A. Zulkharnain, The study of drag reduction on ships inspired by simplified shark skin imitation, *Appl. Bionics Biomech.* 2018 (2018) 1–11. <https://doi.org/10.1155/2018/7854321>.
- [13] X. Li, J. Deng, Y. Lu, L. Zhang, J. Sun, F. Wu, Tribological behavior of ZrO<sub>2</sub>/WS<sub>2</sub> coating surfaces with biomimetic shark-skin structure, *Ceram. Int.* 45 (2019) 21759–21767. <https://doi.org/10.1016/j.ceramint.2019.07.177>.
- [14] G. Liu, Z. Yuan, Z. Qiu, S. Feng, Y. Xie, D. Leng, X. Tian, A brief review of bio-inspired surface technology and application toward underwater drag reduction, *Ocean Eng.* 199 (2020) 106962. <https://doi.org/10.1016/j.oceaneng.2020.106962>.
- [15] M. Xu, A. Grabowski, N. Yu, G. Kerezyte, J.W. Lee, B.R. Pfeifer, C.-J.J. Kim, Superhydrophobic Drag Reduction for Turbulent Flows in Open Water, *Phys. Rev. Appl.* 13 (2020) 034056. <https://doi.org/10.1103/PhysRevApplied.13.034056>.
- [16] H. Park, G. Sun, C.J. Kim, Superhydrophobic turbulent drag reduction as a function of surface grating parameters, *J. Fluid Mech.* 747 (2014) 722–734.

- <https://doi.org/10.1017/jfm.2014.151>.
- [17] M. Xu, N. Yu, J. Kim, C.-J. “CJ” Kim, Superhydrophobic drag reduction in high-speed towing tank, *J. Fluid Mech.* 908 (2021) A6. <https://doi.org/10.1017/jfm.2020.872>.
- [18] B. Liu, Y. He, Y. Fan, X. Wang, Fabricating super-hydrophobic lotus-leaf-like surfaces through soft-lithographic imprinting, *Macromol. Rapid Commun.* 27 (2006) 1859–1864. <https://doi.org/10.1002/marc.200600492>.
- [19] H.S. Hwang, N.H. Kim, S.G. Lee, D.Y. Lee, K. Cho, I. Park, Facile fabrication of transparent superhydrophobic surfaces by spray deposition, *ACS Appl. Mater. Interfaces.* 3 (2011) 2179–2183. <https://doi.org/10.1021/am2004575>.
- [20] S. Kato, A. Sato, Micro/nanotextured polymer coatings fabricated by UV curing-induced phase separation: Creation of superhydrophobic surfaces, *J. Mater. Chem.* 22 (2012) 8613–8621. <https://doi.org/10.1039/c2jm16675e>.
- [21] J. Zou, H. Chen, A. Chunder, Y. Yu, Q. Huo, L. Zhai, Preparation of a superhydrophobic and conductive nanocomposite coating from a carbon-nanotube-conjugated block copolymer dispersion, *Adv. Mater.* 20 (2008) 3337–3341. <https://doi.org/10.1002/adma.200703094>.
- [22] S. Lee, J. Lee, J. Park, Y. Choi, K. Yong, Resistive switching WO<sub>x</sub>-Au core-shell nanowires with unexpected nonwetting stability even when submerged under water, *Adv. Mater.* 24 (2012) 2418–2423. <https://doi.org/10.1002/adma.201200068>.
- [23] L. Zhu, Y. Xiu, J. Xu, P.A. Tamirisa, D.W. Hess, C.P. Wong, Superhydrophobicity on two-tier rough surfaces fabricated by controlled growth of aligned carbon nanotube arrays coated with fluorocarbon, *Langmuir.* 21 (2005) 11208–11212. <https://doi.org/10.1021/la051410+>.

- [24] M.E. Gurfinkel Castillo, A.T. Patera, Three-dimensional ribbing instability in symmetric forward-roll film-coating processes, *J. Fluid Mech.* 335 (1997) 323–359.  
<https://doi.org/10.1017/S0022112096004600>.
- [25] Y.H. Chong, P.H. Gaskell, N. Kapur, Coating with deformable rolls: An experimental investigation of the ribbing instability, *Chem. Eng. Sci.* 62 (2007) 4138–4145.  
<https://doi.org/10.1016/j.ces.2007.04.029>.
- [26] T. Bauman, T. Sullivan, S. Middleman, Ribbing instability in coating flows: Effect of polymer additives, *Chem. Eng. Commun.* 14 (1982) 35–46.  
<https://doi.org/10.1080/00986448208911036>.
- [27] J. Greener, T. Sullivan, B. Turner, S. Middleman, Ribbing instability of a two-roll coater: Newtonian fluids, *Chem. Eng. Commun.* 5 (1980) 73–83.  
<https://doi.org/10.1080/00986448008935954>.
- [28] G.A. Zavallos, M.S. Carvalho, M. Pasquali, Forward roll coating flows of viscoelastic liquids, *J. Nonnewton. Fluid Mech.* 130 (2005) 96–109.  
<https://doi.org/10.1016/j.jnnfm.2005.08.005>.
- [29] R.J. Fields, M.F. Ashby, Finger-like crack growth in solids and liquids, *Philos. Mag.* 33 (1976) 33–48. <https://doi.org/10.1080/14786437608221089>.
- [30] A.M. Grillet, A.G. Lee, E.S.G. Shaqfeh, Observations of ribbing instabilities in elastic fluid flows with gravity stabilization, *J. Fluid Mech.* 399 (1999) 49–83.  
<https://doi.org/10.1017/S002211209900628X>.
- [31] E. Szczurek, M. Dubar, R. Deltombe, A. Dubois, L. DUBAR, New approach to the evaluation of the free surface position in roll coating, *J. Mater. Process. Technol.* 209 (2009) 3187–3197. <https://doi.org/10.1016/j.jmatprotec.2008.07.025>.

- [32] O. Cohu, A. Magnin, Rheometry of paints with regard to roll coating process, *J. Rheol.* (N. Y. N. Y). 39 (1995) 767–785. <https://doi.org/10.1122/1.550656>.
- [33] C.K. Yang, D.S.H. Wong, T.J. Liu, The effects of polymer additives on the operating windows of slot coating, *Polym. Eng. Sci.* 44 (2004) 1970–1976. <https://doi.org/10.1002/pen.20200>.
- [34] G.P. Bierwagen, Film coating technologies and adhesion, *Electrochim. Acta.* 37 (1992) 1471–1478. [https://doi.org/10.1016/0013-4686\(92\)80092-Z](https://doi.org/10.1016/0013-4686(92)80092-Z).
- [35] P. Brumm, H. Sauer, E. Dörsam, Scaling Behavior of Pattern Formation in the Flexographic Ink Splitting Process, *Colloids and Interfaces.* 3 (2019) 37. <https://doi.org/10.3390/colloids3010037>.
- [36] M. Pudas, J. Hagberg, S. Leppävuori, Roller-type gravure offset printing of conductive inks for high-resolution printing on ceramic substrates, *Int. J. Electron.* 92 (2005) 251–269. <https://doi.org/10.1080/00207210500102930>.
- [37] M. Yamamura, Ribbing instability of Newtonian fluid coated on a topographic surface, *J. Coatings Technol. Res.* 17 (2020) 1447–1453. <https://doi.org/10.1007/s11998-020-00375-8>.
- [38] J.H. Lee, S.K. Han, J.S. Lee, H.W. Jung, J.C. Hyun, Ribbing instability in rigid and deformable forward roll coating flows, *Korea Aust. Rheol. J.* 22 (2010) 75–80. <https://koreauniv.pure.elsevier.com/en/publications/ribbing-instability-in-rigid-and-deformable-forward-roll-coating-> (accessed September 8, 2021).
- [39] A.M. Grillet, A.G. Lee, E.S.G. Shaqfeh, Observations of ribbing instabilities in elastic fluid flows with gravity stabilization, *J. Fluid Mech.* 399 (1999) 49–83. <https://doi.org/10.1017/S002211209900628X>.

- [40] M. Rosen, M. Vazquez, Secondary waves in ribbing instability, in: AIP Conf. Proc., American Institute of Physics AIP, 2007: pp. 14–19. <https://doi.org/10.1063/1.2746717>.
- [41] D.J. Coyle, C.W. Macosko, L.E. Scriven, Reverse roll coating of non-Newtonian liquids, *J. Rheol.* (N. Y. N. Y). 34 (1990) 615–636. <https://doi.org/10.1122/1.550145>.
- [42] F. Varela López, L. Pauchard, M. Rosen, M. Rabaud, Non-Newtonian effects on ribbing instability threshold, *J. Nonnewton. Fluid Mech.* 103 (2002) 123–139. [https://doi.org/10.1016/S0377-0257\(01\)00165-3](https://doi.org/10.1016/S0377-0257(01)00165-3).
- [43] M.E. Gurfinkel Castillo, A.T. Patera, Three-dimensional ribbing instability in symmetric forward-roll film-coating processes, *J. Fluid Mech.* 335 (1997) 323–359. <https://doi.org/10.1017/S0022112096004600>.
- [44] T. Bauman, T. Sullivan, S. Middleman, Ribbing instability in coating flows: Effect of polymer additives, *Chem. Eng. Commun.* 14 (1982) 35–46. <https://doi.org/10.1080/00986448208911036>.
- [45] D.A. Soules, R.H. Fernando, J.E. Glass, Dynamic Uniaxial Extensional Viscosity (DUEV) Effects in Roll Application I. Rib and Web Growth in Commercial Coatings, *J. Rheol.* (N. Y. N. Y). 32 (1988) 181–198. <https://doi.org/10.1122/1.549966>.
- [46] D.J. Coyle, Knife and Roll Coating, in: *Liq. Film Coat.*, Springer Netherlands, Dordrecht, 1997: pp. 539–571. [https://doi.org/10.1007/978-94-011-5342-3\\_15](https://doi.org/10.1007/978-94-011-5342-3_15).
- [47] A. Shahsavari, M. Bahiraei, Experimental investigation and modeling of thermal conductivity and viscosity for non-Newtonian hybrid nanofluid containing coated CNT/Fe<sub>3</sub>O<sub>4</sub> nanoparticles, *Powder Technol.* 318 (2017) 441–450. <https://doi.org/10.1016/j.powtec.2017.06.023>.
- [48] S. Abbasi, S.M. Zebarjad, S.H.N. Baghban, A. Youssefi, M.-S. Ekrami-Kakhki,

- Experimental investigation of the rheological behavior and viscosity of decorated multi-walled carbon nanotubes with TiO<sub>2</sub> nanoparticles/water nanofluids, *J. Therm. Anal. Calorim.* 123 (2016) 81–89. <https://doi.org/10.1007/s10973-015-4878-4>.
- [49] B. Jo, D. Banerjee, Viscosity measurements of multi-walled carbon nanotubes-based high temperature nanofluids, *Mater. Lett.* 122 (2014) 212–215. <https://doi.org/10.1016/j.matlet.2014.02.032>.
- [50] S. Mueller, E.W. Llewellyn, H.M. Mader, The rheology of suspensions of solid particles, *Proc. R. Soc. A Math. Phys. Eng. Sci.* 466 (2010) 1201–1228. <https://doi.org/10.1098/rspa.2009.0445>.
- [51] E. Anczurowski, S.G. Mason, Particle Motions in Sheared Suspensions. XXIV. Rotation of Rigid Spheroids and Cylinders, *Trans. Soc. Rheol.* 12 (1968) 209–215. <https://doi.org/10.1122/1.549106>.
- [52] C. Zhang, D.A.M. Ii, J.C. Grunlan, C. Zhang, D.A. Mcadams, J.C. Grunlan, Nano/Micro-Manufacturing of Bioinspired Materials: a Review of Methods to Mimic Natural Structures, *Adv. Mater.* 28 (2016) 6292–6321. <https://doi.org/10.1002/ADMA.201505555>.
- [53] R.A. Lawson, A.P.G. Robinson, Overview of materials and processes for lithography, *Front. Nanosci.* 11 (2016) 1–90. <https://doi.org/10.1016/B978-0-08-100354-1.00001-6>.
- [54] Y. Li, J. Zhang, B. Yang, Antireflective surfaces based on biomimetic nanopillared arrays, *Nano Today.* 5 (2010) 117–127. <https://doi.org/10.1016/J.NANTOD.2010.03.001>.
- [55] T. Nørgaard, M. Dacke, Fog-basking behaviour and water collection efficiency in Namib Desert Darkling beetles, *Front. Zool.* 7 (2010) 1–8. <https://doi.org/10.1186/1742-9994-7-23/FIGURES/5>.
- [56] P. Zhang, F.Y. Lv, A review of the recent advances in superhydrophobic surfaces and the

- emerging energy-related applications, *Energy*. 82 (2015) 1068–1087.  
<https://doi.org/10.1016/J.ENERGY.2015.01.061>.
- [57] X. Yao, Y. Song, L. Jiang, X. Yao, Y. Song, L. Jiang, Applications of Bio-Inspired Special Wettable Surfaces, *Adv. Mater.* 23 (2011) 719–734.  
<https://doi.org/10.1002/ADMA.201002689>.
- [58] R. Carriveau, A. Edrisy, P. Cadieux, R. Mailloux, Ice adhesion issues in renewable energy infrastructure, *J. Adhes. Sci. Technol.* 26 (2012) 447–461.  
<https://doi.org/10.1163/016942411X574592>.
- [59] R.W. Gent, N.P. Dart, J.T. Cansdale, Aircraft icing, *Philos. Trans. R. Soc. London. Ser. A Math. Phys. Eng. Sci.* 358 (2000) 2873–2911. <https://doi.org/10.1098/RSTA.2000.0689>.
- [60] R. Enright, C. Eason, T. Dalton, M. Hodes, T. Salamon, P. Kolodner, T. Krupenkin, Friction Factors and Nusselt Numbers in Microchannels With Superhydrophobic Walls, *Proc. 4th Int. Conf. Nanochannels, Microchannels Minichannels, ICNMM2006*. 2006 A (2008) 599–609. <https://doi.org/10.1115/ICNMM2006-96134>.
- [61] S. Han, R. Yang, C. Li, L. Yang, The Wettability and Numerical Model of Different Silicon Microstructural Surfaces, *Appl. Sci.* 9 (2019) 566.  
<https://doi.org/10.3390/app9030566>.
- [62] Y. Zhang, F. Shen, W. Cao, Y. Wan, Hydrophilic/hydrophobic Janus membranes with a dual-function surface coating for rapid and robust membrane distillation desalination, *Desalination*. 491 (2020) 114561. <https://doi.org/10.1016/J.DESAL.2020.114561>.
- [63] M. Kawabuchi, C. Kawakita, S. Mizokami, S. Higasa, Y. Kodan, S. Takano, CFD Predictions of Bubbly Flow around an Energy-saving Ship with Mitsubishi Air Lubrication System, *Mitsubishi Heavy Ind. Tech. Rev.* 48 (2011) 53–57.

- <http://www.mhi.co.jp/en/technology/review/pdf/e481/e481053.pdf> (accessed May 14, 2022).
- [64] N. Wang, L. Tang, Y. Cai, W. Tong, D. Xiong, Scalable superhydrophobic coating with controllable wettability and investigations of its drag reduction, *Colloids Surfaces A Physicochem. Eng. Asp.* 555 (2018) 290–295.  
<https://doi.org/10.1016/J.COLSURFA.2018.07.011>.
- [65] M. Xu, N. Yu, J. Kim, C.-J. “CJ” Kim, Superhydrophobic drag reduction in high-speed towing tank, *J. Fluid Mech.* 908 (2021) A6. <https://doi.org/10.1017/jfm.2020.872>.
- [66] C. Henoeh, T.N. Krupenkin, P. Kolodner, J.A. Taylor, M.S. Hodes, A.M. Lyons, C. Peguero, K. Breuer, Turbulent drag reduction using superhydrophobic surfaces, in: *Collect. Tech. Pap. - 3rd AIAA Flow Control Conf.*, 2006: pp. 840–844.  
<https://doi.org/10.2514/6.2006-3192>.
- [67] B. Woolford, J. Prince, D. Maynes, B.W. Webb, Particle image velocimetry characterization of turbulent channel flow with rib patterned superhydrophobic walls, *Phys. Fluids.* 21 (2009) 085106. <https://doi.org/10.1063/1.3213607>.
- [68] K. Watanabe, Yanuar, H. Udagawa, Drag reduction of Newtonian fluid in a circular pipe with a highly water-repellent wall, *J. Fluid Mech.* 381 (1999) 225–238.  
<https://doi.org/10.1017/S0022112098003747>.
- [69] N.J. Shirtcliffe, G. McHale, M.I. Newton, Y. Zhang, Superhydrophobic copper tubes with possible flow enhancement and drag reduction, *ACS Appl. Mater. Interfaces.* 1 (2009) 1316–1323. <https://doi.org/10.1021/am9001937>.
- [70] D. Kim, W. Hwang, A template-based superhydrophobic tube structure with nanofiber forests and its mass flow characteristic, *J. Micromechanics Microengineering.* 20 (2010)

027002. <https://doi.org/10.1088/0960-1317/20/2/027002>.
- [71] P. Joseph, C. Cottin-Bizonne, J.M. Benoît, C. Ybert, C. Journet, P. Tabeling, L. Bocquet, Slippage of water past superhydrophobic carbon nanotube forests in microchannels, *Phys. Rev. Lett.* 97 (2006) 156104. <https://doi.org/10.1103/PhysRevLett.97.156104>.
- [72] H. Park, C.H. Choi, C.J. Kim, Superhydrophobic drag reduction in turbulent flows: a critical review, *Exp. Fluids.* 62 (2021) 1–29. <https://doi.org/10.1007/s00348-021-03322-4>.
- [73] C. Lee, C.H. Choi, C.J. Kim, Superhydrophobic drag reduction in laminar flows: a critical review, *Exp. Fluids.* 57 (2016) 1–20. <https://doi.org/10.1007/s00348-016-2264-z>.
- [74] H. Park, C.H. Choi, C.J. Kim, Superhydrophobic drag reduction in turbulent flows: a critical review, *Exp. Fluids.* 62 (2021) 1–29. <https://doi.org/10.1007/s00348-021-03322-4>.
- [75] L.M. Cox, A.M. Martinez, A.K. Blevins, N. Sowan, Y. Ding, C.N. Bowman, Nanoimprint lithography: Emergent materials and methods of actuation, *Nano Today.* 31 (2020) 100838. <https://doi.org/10.1016/J.NANTOD.2019.100838>.
- [76] D.W. Li, H.Y. Wang, Y. Liu, D.S. Wei, Z.X. Zhao, Large-scale fabrication of durable and robust super-hydrophobic spray coatings with excellent repairable and anti-corrosion performance, *Chem. Eng. J.* 367 (2019) 169–179. <https://doi.org/10.1016/J.CEJ.2019.02.093>.
- [77] S.-H. Park, S. Lee, D. Moreira, P.R. Bandaru, I. Han, D.-J. Yun, Bioinspired superhydrophobic surfaces, fabricated through simple and scalable roll-to-roll processing, *Sci. Rep.* 5 (2015) 15430. <https://doi.org/10.1038/srep15430>.
- [78] A.M. Grillet, A.G. Lee, E.S.G. Shaqfeh, Observations of ribbing instabilities in elastic fluid flows with gravity stabilization, *J. Fluid Mech.* 399 (1999) 49–83. <https://doi.org/10.1017/S002211209900628X>.

- [79] F.M. Fowkes, Additivity of intermolecular forces at interfaces. I. Determination of the contribution to surface and interfacial tensions of dispersion forces in various liquids 1, *J. Phys. Chem.* 67 (1963) 2538–2541. <https://doi.org/10.1021/j100806a008>.
- [80] D.K. Owens, R.C. Wendt, Estimation of the surface free energy of polymers, *J. Appl. Polym. Sci.* 13 (1969) 1741–1747. <https://doi.org/10.1002/app.1969.070130815>.
- [81] N. Selvakumar, H.C. Barshilia, K.S. Rajam, Effect of substrate roughness on the apparent surface free energy of sputter deposited superhydrophobic polytetrafluoroethylene coatings: A comparison of experimental data with different theoretical models, *J. Appl. Phys.* 108 (2010) 013505. <https://doi.org/10.1063/1.3456165>.
- [82] A. Kozbial, Z. Li, C. Conaway, R. McGinley, S. Dhingra, V. Vahdat, F. Zhou, B. Durso, H. Liu, L. Li, Study on the surface energy of graphene by contact angle measurements, *Langmuir.* 30 (2014) 8598–8606. <https://doi.org/10.1021/la5018328>.
- [83] H.J. Walls, S.B. Caines, A.M. Sanchez, S.A. Khan, Yield stress and wall slip phenomena in colloidal silica gels, *J. Rheol. (N. Y. N. Y).* 47 (2003) 847–868. <https://doi.org/10.1122/1.1574023>.
- [84] S. Wu, Calculation of interfacial tension in polymer systems, *J. Polym. Sci. Part C Polym. Symp.* 34 (1971) 19–30. <https://doi.org/10.1002/POLC.5070340105>.
- [85] Surface Energy Data for PDMS: Polydimethylsiloxane, CAS #9016-00-6, (n.d.). [http://www.accudynetest.com/polymer\\_surface\\_data/polydimethylsiloxane.pdf](http://www.accudynetest.com/polymer_surface_data/polydimethylsiloxane.pdf) (accessed May 1, 2022).
- [86] A. Dresel, U. Teipel, Influence of the wetting behavior and surface energy on the dispersibility of multi-wall carbon nanotubes, *Colloids Surfaces A Physicochem. Eng. Asp.* 489 (2016) 57–66. <https://doi.org/10.1016/J.COLSURFA.2015.10.027>.

- [87] S.C. Roh, E.Y. Choi, Y.S. Choi, C.K. Kim, Characterization of the surface energies of functionalized multi-walled carbon nanotubes and their interfacial adhesion energies with various polymers, *Polymer (Guildf)*. 55 (2014) 1527–1536.  
<https://doi.org/10.1016/J.POLYMER.2014.02.015>.
- [88] S. Nuriel, L. Liu, A.H. Barber, H.D. Wagner, Direct measurement of multiwall nanotube surface tension, *Chem. Phys. Lett.* 404 (2005) 263–266.  
<https://doi.org/10.1016/J.CPLETT.2005.01.072>.
- [89] Y. Chan Jeong, S. Jae Yang, K. Lee, al -, Y. Kamebuchi, Y. Kamimoto, M.H. Al-Saleh, Measuring surface energy of carbon nanotubes using modified washburn method, *Mater. Res. Express*. 6 (2019) 115088. <https://doi.org/10.1088/2053-1591/AB4B2C>.
- [90] C.W. Macosko, *Rheology : principles, measurements, and applications*, VCH, 1994.
- [91] R.D. Corder, P. Adhikari, M.C. Burroughs, O.J. Rojas, S.A. Khan, Cellulose nanocrystals for gelation and percolation-induced reinforcement of a photocurable poly(vinyl alcohol) derivative, *Soft Matter*. 16 (2020) 8602–8611. <https://doi.org/10.1039/D0SM01376E>.
- [92] S.A. Jin, E.G. Facchine, S.A. Khan, O.J. Rojas, R.J. Spontak, Mesophase characteristics of cellulose nanocrystal films prepared from electrolyte suspensions, *J. Colloid Interface Sci.* 599 (2021) 207–218. <https://doi.org/10.1016/J.JCIS.2021.04.071>.
- [93] S. Wang, H. Tang, J. Guo, K. Wang, Effect of pH on the rheological properties of borate crosslinked hydroxypropyl guar gum hydrogel and hydroxypropyl guar gum, *Carbohydr. Polym.* 147 (2016) 455–463. <https://doi.org/10.1016/J.CARBPOL.2016.04.029>.
- [94] M. Razavi-Nouri, A. Sabet, M. Mohebbi, Effect of organoclay content on mechanical and rheological properties of dynamically cross-linked acrylonitrile-butadiene rubber/poly(ethylene-co-vinyl acetate)/organoclay nanocomposites, *Polym. Bull.* 77

- (2020) 5933–5952. <https://doi.org/10.1007/S00289-019-03060-Y/TABLES/5>.
- [95] T. V. Neumann, E.G. Facchine, B. Leonardo, S. Khan, M.D. Dickey, Direct write printing of a self-encapsulating liquid metal–silicone composite, *Soft Matter*. 16 (2020) 6608–6618. <https://doi.org/10.1039/D0SM00803F>.
- [96] Y.Y. Huang, S. V. Ahir, E.M. Terentjev, Dispersion rheology of carbon nanotubes in a polymer matrix, *Phys. Rev. B - Condens. Matter Mater. Phys.* 73 (2006) 125422. <https://doi.org/10.1103/PhysRevB.73.125422>.
- [97] N.A. Burns, M.A. Naclerio, S.A. Khan, A. Shojaei, S.R. Raghavan, Nanodiamond gels in nonpolar media: Colloidal and rheological properties, *J. Rheol. (N. Y. N. Y.)*. 58 (2014) 1599. <https://doi.org/10.1122/1.4892901>.
- [98] D.J. Coyle, C.W. Macosko, L.E. Scriven, Film-splitting flows in forward roll coating, *J. Fluid Mech.* 171 (1986) 183–207. <https://doi.org/10.1017/S0022112086001416>.
- [99] D.J. Coyle, C.W. Macosko, L.E. Scriven, Film-splitting flows of shear-thinning liquids in forward roll coating, *AIChE J.* 33 (1987) 741–746. <https://doi.org/10.1002/aic.690330506>.
- [100] M.S. Owens, M. Vinjamur, L.E. Scriven, C.W. Macosko, Misting of non-Newtonian liquids in forward roll coating, *J. Nonnewton. Fluid Mech.* 166 (2011) 1123–1128. <https://doi.org/10.1016/j.jnnfm.2011.06.008>.
- [101] A.F. Stalder, G. Kulik, D. Sage, L. Barbieri, P. Hoffmann, A snake-based approach to accurate determination of both contact points and contact angles, *Colloids Surfaces A Physicochem. Eng. Asp.* 286 (2006) 92–103. <https://doi.org/10.1016/j.colsurfa.2006.03.008>.
- [102] C.A. Schneider, W.S. Rasband, K.W. Eliceiri, NIH Image to ImageJ: 25 years of image analysis, *Nat. Methods*. 9 (2012) 671–675. <https://doi.org/10.1038/nmeth.2089>.

- [103] M.S. Owens, M. Vinjamur, L.E. Scriven, C.W. Macosko, Misting of non-Newtonian liquids in forward roll coating, *J. Nonnewton. Fluid Mech.* 166 (2011) 1123–1128. <https://doi.org/10.1016/j.jnnfm.2011.06.008>.
- [104] Nanovea, Scratch Hardness Measurement Using Tribometer, (2014).
- [105] D. Li, UNDERSTANDING COATING FAILURES USING SCRATCH TESTING, NANOVEA. (2013) 1–10.
- [106] M.P. Schultz, Effects of coating roughness and biofouling on ship resistance and powering, *Biofouling.* 23 (2007) 331–341. <https://doi.org/10.1080/08927010701461974>.
- [107] Q. Pan, M. Wang, Miniature boats with striking loading capacity fabricated from superhydrophobic copper meshes, *ACS Appl. Mater. Interfaces.* 1 (2009) 420–423. <https://doi.org/10.1021/am800116d>.
- [108] Y. Xia, P. Cai, Y. Liu, J. Zhu, R. Guo, W. Zhang, Y. Gan, H. Huang, J. Zhang, C. Liang, X. He, Z. Xiao, A Low-Cost and High-Efficiency Electrothermal Composite Film Composed of Hybrid Conductivity Fillers and Polymer Blends Matrix for High-Performance Plate Heater, *J. Electron. Mater.* 50 (2021) 3084–3094. <https://doi.org/10.1007/s11664-021-08873-0>.
- [109] B. Earp, J. Simpson, J. Phillips, D. Grbovic, S. Vidmar, J. McCarthy, C.C. Luhrs, Electrically conductive CNT composites at loadings below theoretical percolation values, *Nanomaterials.* 9 (2019) 491. <https://doi.org/10.3390/nano9040491>.
- [110] D.M. Kalyon, E. Birinci, R. Yazici, B. Karuv, S. Walsh, Electrical properties of composites as affected by the degree of mixedness of the conductive filler in the polymer matrix, *Polym. Eng. Sci.* 42 (2002) 1609–1617. <https://doi.org/10.1002/pen.11056>.
- [111] A. Mora, P. Verma, S. Kumar, Electrical conductivity of CNT/polymer composites: 3D

printing, measurements and modeling, *Compos. Part B Eng.* 183 (2020) 107600.

<https://doi.org/10.1016/j.compositesb.2019.107600>.

[112] C. Lee, C.J. Kim, Underwater restoration and retention of gases on superhydrophobic surfaces for drag reduction, *Phys. Rev. Lett.* 106 (2011) 014502.

<https://doi.org/10.1103/PhysRevLett.106.014502>.

[113] M. Xu, C.T. Liu, C.J. Kim, Self-Powered Plastron Preservation and One-Step Molding of Semiactive Superhydrophobic Surfaces, *Langmuir.* 36 (2020) 8193–8198.

<https://doi.org/10.1021/acs.langmuir.0c01289>.

[114] X. Li, J. Deng, H. Yue, D. Ge, X. Zou, Wear performance of electrohydrodynamically atomized WS<sub>2</sub> coatings deposited on biomimetic shark-skin textured surfaces, *Tribol. Int.*

134 (2019) 240–251. <https://doi.org/10.1016/j.triboint.2019.02.015>.